ALMA MATER STUDIORUM
UNIVERSITÀ DI BOLOGNA

DOTTORATO DI RICERCA IN

SCIENZE E TECNOLOGIE DELLA SALUTE

Ciclo 38

Settore Concorsuale: 09/G2 - BIOINGEGNERIA

Settore Scientifico Disciplinare: ING-IND/34 - BIOINGEGNERIA INDUSTRIALE

TOWARD IN SILICO TRIALS TO ESTIMATE THE RISK OF ASEPTIC LOOSENING IN NEW JOINT REPLACEMENT DESIGNS

Presentata da: Xiaoshu Sun

Coordinatore Dottorato

Igor Diemberger

Supervisore

Marco Viceconti

Co-supervisore

Cesare Faldini

Esame finale anno 2026

Abstract

The global rise in ageing and obesity has increased the prevalence of knee and hip osteoarthritis, driving higher demand for total joint arthroplasty (TJA), including both primary and revision procedures. Despite high long-term survival rates, the burden of revision surgery highlights the importance of reducing surgical failure risks. Among failure modes, aseptic loosening remains the most common, defined as the failure of the bone-implant fixation in the absence of infection.

As a multifactorial complication often associated with periprosthetic osteolysis and inflammatory responses, aseptic loosening can be mechanically driven by excessive micromotion at the bone–implant interface and wear-induced polyethylene particles. Practically speaking, it is influenced by a range of preoperative, intraoperative, and postoperative factors, including patients' bone quality, implant properties, surgical technique, and lifestyles. Among these, implant design plays a crucial role in the procedure's success. Studies have reported significantly different aseptic loosening incidence rates across implants. Therefore, studying the effect of implant designs on failure risk is essential to improving patient safety, reducing healthcare costs, and achieving long-term clinical success.

Conventional approaches, such as in vivo experiments, animal studies, and clinical trials, are commonly used to assess implant safety and predict aseptic loosening risk. However, these methods are often limited by biological irrelevance, species differences, and high costs or long durations. In contrast, in silico trials have emerged as a powerful alternative to investigate the individual joint biomechanics and support the orthopaedic device's safety and/or efficacy. In particular, a finite element analysis (FEA) model enables detailed analysis of TJA outcome by involving specific patients, implant design and even the surgical procedures.

The main aim of this thesis is to develop an in silico trial to estimate the risk of aseptic loosening in an anatomical cementless hip stem design. FEA models were used to predict the *primary stability* (the relative micromotion in each point of the bone-implant contact surface induced by physiological activities such as level walking or stair climbing) of a commercial stem design (Apta, Adler Ortho), for which extensive clinical experience is available. Specific thresholds derived from published experimental mechanobiology studies were used to decide which portion of the stem surface may experience fibrous differentiation, the first step toward aseptic loosening.

This basic model was then used to explore the primary stability of the Apta stem as a function of the femoral size, the subject's weight, the pre-operative bone quality (degree of osteopenia), and the surgical uncertainty on the implant sizing.

To support large-scale assessments, an automated FEA pipeline for orthopaedic devices was implemented, allowing for efficient batch processing of patient data, physiological loading cases, implant variations, or surgical plans in the future.

Contents

Chapter 1

Hip Joint Replacement

1.1 Biomechanics of joints

1.1.1 Anatomical Structure of the Hip Joint

The hip is a highly stable and mobile synovial joint, classified biomechanically as a ball-and-socket joint. It is formed by the articulation between the femoral head (the ball) and the acetabulum of the pelvis (the socket). The acetabulum is a deep, cup-shaped cavity located on the lateral aspect of the pelvis, formed by the fusion of three bones: the ilium, ischium, and pubis. To enhance the depth and stability of the socket, a fibrocartilaginous rim known as the acetabular labrum is attached to its margin. This structure enlarges the articular surface and creates a suction effect that further secures the femoral head within the joint. The transverse acetabular ligament bridges the acetabular notch, completing the circular contour of the acetabular rim and further reinforcing the containment of the femoral head. The anatomical structure of the hip joint is shown in Fig. 1.1.

The femoral head and the acetabulum are covered with hyaline cartilage, which reduces friction and absorbs mechanical shock during joint movement. Notably, articular cartilage nearly completely covers the surface of the femoral head. In contrast, the central and inferior portion of the acetabulum—the acetabular fossa—is not covered by cartilage [1]. As a result, the acetabular cartilage adopts a distinct horseshoe-shaped configuration, known anatomically as the *lunate surface*. The geometry of the lunate surface has been shown to optimize the distribution of contact stress within the joint, minimizing peak pressure [2].

Distal to the femoral head lies the femoral neck, a narrowed region connecting the head to the shaft of the femur. Lateral to the femoral neck are two important bony prominences: the greater trochanter laterally and the lesser trochanter medially and posteriorly. These are critical attachment points for muscles such as the gluteus medius, gluteus minimus, iliopsoas, and several external rotators, playing key roles in hip movement and stabilization.

The joint capsule of the hip is thick, fibrous, and highly resilient, attaching proximally to the outer rim of the acetabulum and the transverse ligament, and distally to the femoral neck—reaching the intertrochanteric line anteriorly and enveloping the medial two-thirds of the femoral neck posteriorly, just above the intertrochanteric crest.

Strong ligaments, including the iliofemoral, pubofemoral, and ischiofemoral ligaments, further reinforce joint stability, which prevents excessive extension and rotation. Additionally, several bursae, such as the trochanteric and iliopsoas bursae, help reduce friction between bones, tendons, and muscles. The surrounding

muscles, including the gluteus maximus, gluteus medius, adductors, and iliopsoas, contribute to movement and dynamic joint stabilization.

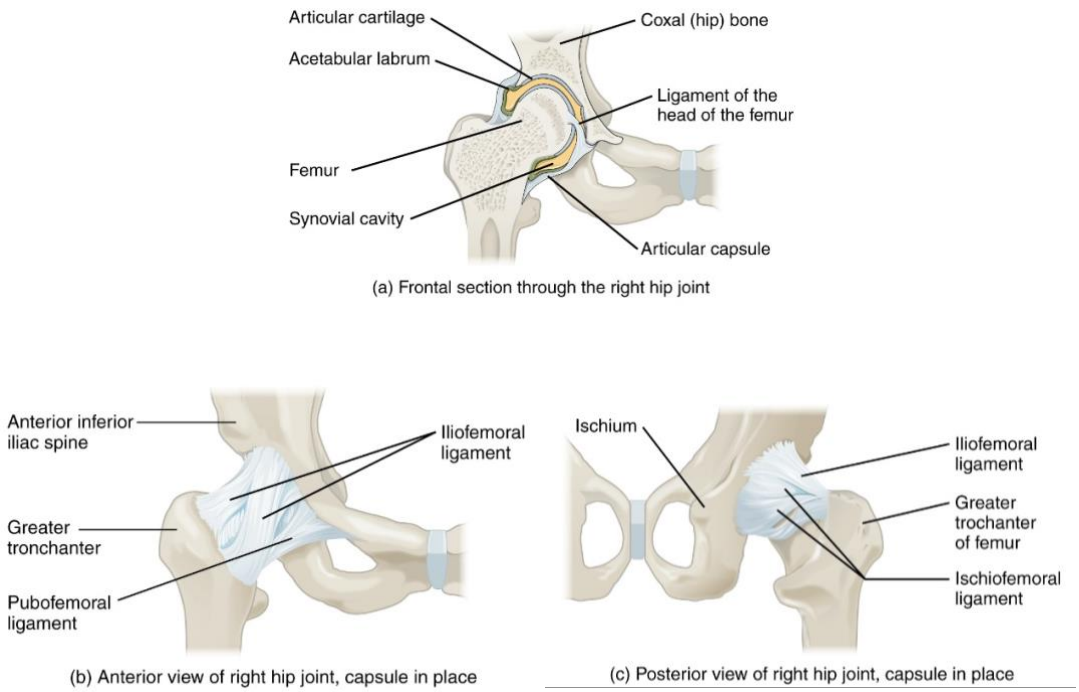

Figure 1.1. Hip joint anatomy. (a) Frontal section through the right hip joint, showing the articulation between the femoral head and the acetabulum, covered with articular cartilage and enclosed within the synovial cavity and articular capsule. (b) Anterior view of the right hip joint with capsule in place, illustrating the iliofemoral and pubofemoral ligaments that reinforce the joint anteriorly and connect the pelvis to the femur. (c) Posterior view of the right hip joint with capsule in place, displaying the ischiofemoral ligament, which stabilizes the posterior aspect of the joint. Reprinted from OpenStax, CC BY 3.0 < http://creativecommons.org/licenses/by/3.0/>, via Wikimedia Commons.

1.1.2 Biomechanical Function of the Hip Joint

As a large, weight-bearing synovial joint, the hip joint transfers the most significant load and connects the axial skeleton to the lower limb. It plays a central role in human locomotion, as a key driver of movement and load transmission between the upper body and lower limbs. The hip joint allows a wide range of motion in multiple planes, including flexion, extension, abduction, adduction, and internal/external rotation, supporting nearly all static and dynamic activities.

The following sections discuss hip joint kinematics and hip joint kinetics. The joint kinematics describes joint motions, while kinetics provides insight into the forces and torques that drive these movements. Together, they offer a comprehensive understanding of joint biomechanical function during locomotion.

1.1.2.1 Hip Joint Kinematics

The kinematics of the joint involves the study of its motion without reference to the forces causing it. As a multi-axial joint, the hip enables motion in three anatomical planes (frontal, sagittal, and transverse), and is fundamental for gait, postural control, and athletic activities. The orientation of the pelvis, femoral anteversion, and acetabular coverage all influence the hip joint range of motion. During daily movements, the femoral head rotates smoothly within the acetabulum, guided by the surrounding capsular ligaments and musculature.

Gait analysis based on motion capture has made it possible to quantify hip joint motion across different planes accurately:

1. In the frontal (coronal) plane, the joint permits approximately 10° to 45° of abduction and 10° to 30° of adduction, depending on body position and muscle flexibility.
2. In the transverse (axial) plane, the hip joint permits approximately 30° of internal rotation and up to 60° of external rotation in an extended or neutral position. As the hip flexes, rotational mobility increases, allowing for up to 60° of internal and approximately 90° of external rotation.
3. Hip flexion is highly dependent on the knee position in the sagittal plane. With the knee in an extended position, hip flexion is typically limited due to hamstring tension, while the flexion range increases substantially with the knee flexed. The overall hip flexion range varies from 100° to 140°, depending on whether the knee is straight or bent. Hip extension, on the other hand, is more limited and usually ranges from 10° to 20°.

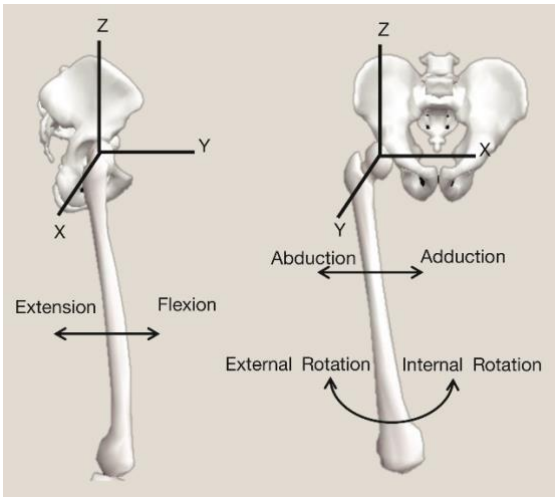

Figure 1.2. Axis of rotation around the hip joint centre and movements produced by the hip joint. Flexion and extension occur in the sagittal plane around the frontal (y) axis. Abduction and adduction movement occurs in the frontal plane around the sagittal (x) axis. Internal and external rotation occur in the transverse plane around the vertical (z) axis. Reprinted with permission of Elsevier from [3] .

1.1.2.2 Hip joint kinetics

Joint kinetics refers to the study of the forces and moments that act on the joint during static and dynamic activities. Joint reaction forces result from the combined effect of external loads and internal muscle forces acting across the joint. Hip joint contact force represents the vector sum of the external ground reaction force (GRF) and the internal forces generated by surrounding musculature, particularly the abductors (F_{abd}).

The magnitude of the hip joint contact force can be explained using a biomechanical lever model, as illustrated in Fig.1.3. Under a single-leg stance, the body weight acts downward from the body's centre of mass and creates a moment around the hip joint. This moment must be counterbalanced by the upward force generated by the hip abductor muscles (F_{abd}). Due to anatomical constraints, the abductor lever arm (r)—defined as the perpendicular distance from the hip joint centre to the line of action of the abductor muscles—is significantly shorter than the body weight lever arm (R)—the distance from the hip joint centre to the line of action of the GRF. This mechanical disadvantage requires the abductors to exert a force that is a multiple of body weight to maintain pelvic stability. The resulting hip joint contact force becomes several times greater than body weight, especially during the stance phase of gait. This force vector is oriented upward and medially, guiding the femoral head into the acetabulum during weight-bearing. The femoral offset (FO) and acetabular offset (AO), as labelled in Fig.1.3, influence the effective length of the abductor lever arm and therefore directly affect joint loading dynamics.

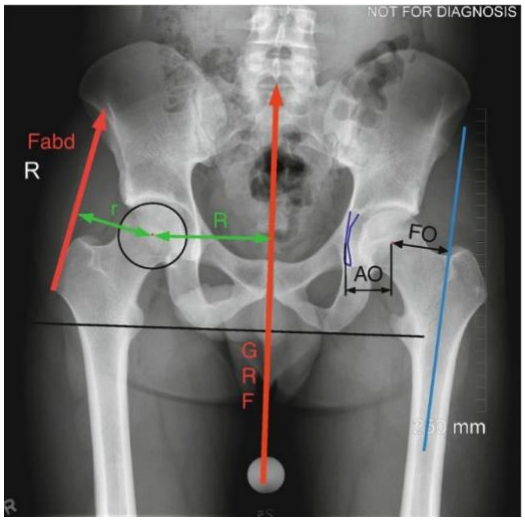

Figure 1.3. AP pelvis X-rays. F_{abd}: Abductor muscle force; GRF: Ground Reaction Force; FO: Femoral Offset; AO: Acetabular Offset; r: Abductor lever arm; R: Body weight lever arm. Reprinted with permission from [4], CC BY 4.0 <https://creativecommons.org/licenses/by/4.0/>.

The load varies considerably depending on body posture and movement. Researchers often employ musculoskeletal (MSK) models based on motion capture data and inverse dynamics analysis to estimate the internal joint forces. Through gait analysis, reflective markers are placed on anatomical landmarks to record three-dimensional limb movements. These kinematic data are then used to calculate joint angles and simulate

internal forces, including muscle and joint contact forces. A range of daily activities—such as walking, turning, sit to stand, squatting, kneeling, reaching, lunging, and golf swing—have been analysed using this approach [5]. The resulting peak hip joint contact forces vary widely, ranging from 0.5 to 6.4 times body weight, depending on the specific task and individual musculoskeletal characteristics. In healthy individuals, the variability between subjects can reach up to 30% [5].

Using instrumented prostheses, Bergmann et.al [6] recorded in vivo hip joint contact forces throughout the entire gait cycle. Their study included nine representative daily activities: slow walking, normal walking, fast walking, ascending stairs, descending stairs, standing up, sitting down, alternating single-leg stance (2–1–2), and knee bending. During normal walking, the peak hip contact force was approximately 238% of body weight, while during down stair climbing, it increased to around 260% of body weight. Other daily activities resulted in comparatively lower hip joint loading.

Normal walking and stair climbing are considered the most critical loading scenarios in biomechanical and implant design studies, considering the activity frequency and the joint loading magnitude.

1.1.3 Hip Joint Disorders

1.1.3.1 Osteoarthritis overview

Osteoarthritis (OA) is a chronic, degenerative joint disease characterized by the gradual breakdown of articular cartilage, leading to joint pain, stiffness, and reduced mobility. It is one of the leading causes of disability globally [7], [8]. The number of individuals affected by OA has more than doubled over the past three decades, rising from 247.5 million in 1990 to 527.8 million in 2019 [9], [10]. While knee OA remains the most prevalent form, hip OA has demonstrated the highest estimated annual percentage increase in many countries [9]. In Europe, radiographic prevalence of hip OA was reported as 12.59% [10].

In healthy joints, the ends of the femoral head are covered with a layer of tough, smooth cartilage that functions as both a shock absorber and a lubricant, allowing for smooth and pain-free movement. As the cartilage deteriorates over time, the bones begin to rub against each other, causing severe pain and functional impairment. Late-stage osteoarthritis of the hip with loss of cartilage, narrowing of the joint space (the space between the bones), and bone spurs (Fig. 1.4).

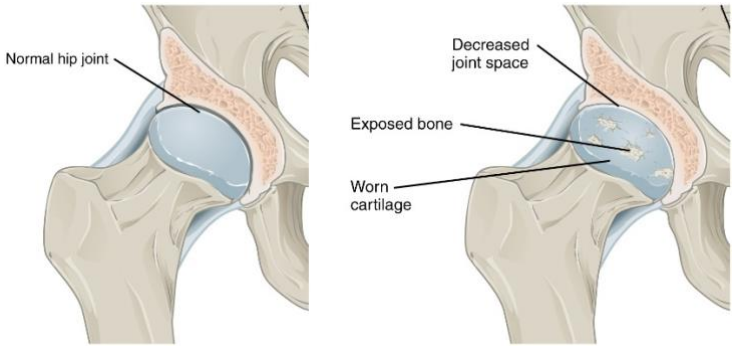

Figure 1.4. To compensate for the lost cartilage, the damaged bones may grow outward and form bone spurs (osteophytes). Reprinted from OpenStax, CC BY 4.0 <https://creativecommons.org/licenses/by/4.0/>, via Wikimedia Commons.

OA can be classified into two major types: primary and secondary. Primary OA is the most common form and typically develops with age due to the cumulative effects of joint use over time. In contrast, secondary OA arises from specific causes that damage joint structures. The most common contributors include trauma or sports-related injuries, and inflammatory arthritis, such as rheumatoid arthritis, gout, and psoriatic arthritis.

1.1.3.2 Biomechanics alteration

In pathological conditions, mechanical alterations in hip joint loading often result in compensatory movement adaptations and modified gait patterns. Studies have shown that patients with hip OA exhibit reduced joint contact forces in both the ipsilateral and contralateral hips during level walking [11], [12]. Specifically, hip joint contact forces' first and second peaks are reduced by approximately 22% and 32%, respectively [12]. These reductions are observed across all three anatomical planes, resulting in a more vertical and medially directed load distribution. Moreover, hip OA patients tend to reduce hip flexion during level walking. During stair climbing, altered locomotor strategies have been observed, particularly aimed at reducing the demand on the hip abductor muscles [13]. In addition, due to altered mechanical loading on the contralateral limb, there is an increased risk of developing secondary OA in the opposite hip.

1.2 Hip Joint Replacement

Total hip arthroplasty (THA) is the definitive intervention for end-stage degenerative, rheumatologic joint diseases and hip fractures. It is typically considered when conservative treatments, including pharmacological and physical therapies, fail to provide adequate symptom relief. By replacing the damaged or diseased components of the hip joint with prosthetic implants, THA aims to re-establish physiological load transmission across the hip, thereby restoring joint biomechanics. Since the 1960s, THA has demonstrated clinical efficacy in alleviating hip pain, restoring mobility, improving quality of life, and enabling patients to resume routine functional activities. Although modern THA's success rate is over 90% within 10 years, continuous optimization in prosthetic implant designs and materials is still being pursued.

This section consists of the following parts:

- THA components
- Fixation approach
- Surgical management
- Postoperative THA registry

1.2.1 THA Components

Standard primary THA usually consists of acetabular and femoral components, as the procedure replaces the damaged acetabulum and femoral head. The main components typically include an acetabular cup, liner, a femoral head (ball), and a femoral stem.

1.2.1.1 Acetabular components and bearing surface

The original hip joint socket is replaced with a cup and an inner liner on the acetabular side. **Acetabular components** have been designed as either non-modular or modular systems. Modular designs typically consist of a metallic acetabular shell implanted into the pelvic bone and a separate modular liner articulating with the femoral head. Depending on clinical requirements, the liner is seated within the shell and commonly fabricated from polyethylene, ceramic, or, less commonly, metal. It offers intraoperative flexibility by allowing the selection of different bearing surfaces. Bearing surfaces refer to the contact interface between the femoral head and the acetabular liner, playing a pivotal role in the tribological performance of the implant. Accounting for various combinations of femoral head and acetabular liner, these are broadly categorized into ***hard-on-hard*** and ***hard-on-soft***, with material pairings drawn from polymers, ceramics, and metals.

Hard-on-hard configurations involve the use of rigid materials in both the femoral and acetabular components, most commonly metal-on-metal (MoM) or ceramic-on-ceramic (CoC). Although initially developed in the mid-20th century, MoM bearings experienced a resurgence due to their potential for reduced volumetric wear

and suitability for larger femoral heads. However, subsequent reports linked them to adverse biological responses such as metal hypersensitivity, aseptic lymphocyte-dominated vasculitis-associated lesions, leading to high failure rates and declining use [14]. Alternatively, CoC was introduced to avoid issues associated with MoM. While it eliminates metal ion release and exhibits excellent wear characteristics, its brittleness presents manufacturing and clinical challenges, including precise component matching to avoid chipping and squeaking during joint motion [15].

Hard-on-soft configurations, by contrast, pair a rigid femoral head (metal or ceramic) with a polymer-based acetabular liner, typically ultra-high-molecular-weight polyethylene (UHMWPE). Metal-on-polyethylene (MoP) features a metallic femoral head articulating against a polyethylene liner. Since its introduction in the 1970s, it has remained prevalent due to its favourable safety profile and cost-efficiency. Yet, long-term implantation can lead to polyethylene wear and the generation of particulate debris, contributing to osteolysis and implant loosening. Cross-linked polyethylene (XLPE) was introduced to improve wear resistance. This material, produced by exposing UHMWPE to radiation to enhance molecular cross-linking, has significantly improved performance in long-term wear studies. Additionally, ceramic-on-polyethylene (CoP) configurations combine the wear resistance of ceramic femoral heads with the affordability and flexibility of polyethylene liners. The ceramic head's polished surface and hardness reduce abrasive wear on the liner, although early generations were occasionally criticized for cost and risk of fracture.

1.2.1.2 Femoral components

The femoral component of THA consists of a spherical femoral head and a femoral stem. The head is mounted onto a neck segment, which may be either monoblock (fixed) or modular. Modular necks enable surgeons to optimize joint biomechanics by selecting angles, lengths, and offsets that best match the patient's anatomy. The femoral stem is implanted into the intramedullary canal of the femur, providing the primary means of fixation and load transfer from the joint to the femoral bone. Due to their high biocompatibility, corrosion resistance, and mechanical strength, it is generally constructed from stainless steel, cobalt–chromium alloy, titanium alloy, and composites.

Over the years, various femoral stem designs have been developed. These designs differ in structural aspects, including stem length, geometry, cross-sectional shape, and curvature. Correspondingly, stems can be categorized based on their geometry: ***straight stems*** have a straight longitudinal axis from the neck to the distal tip; ***anatomical stems*** that follow the natural shape of the femur, ***cylindrical stems*** with uniform cross-sections; and ***tapered stems*** that narrow distally for press-fit fixation [16]. However, beyond shape, stems also differ in material properties and in how the head and neck components are configured. Surface treatments are another key differentiator — some implants are coated only at the proximal end, while others feature full-length surface coverage. The textures and coatings applied, such as porous structures, fibre-metal layers, or hydroxyapatite, are designed to enhance bone ingrowth and biological fixation. The most fundamental classification

distinguishes between stems designed for cemented and cementless fixation, which will be discussed in the following section of the fixation approach.

Mont classification is the most widely adopted system for categorizing cementless femoral stems used in primary THA [17]. This classification was proposed by Mont et al. in 2011[18]. It divides stem designs into six types based on their geometry, fixation principles, and intended load transfer characteristics, as shown in Fig.1.5.

Type 1, or single-wedge stems, are broad in the anteroposterior (AP) plane and narrow mediolaterally, typically featuring a straight, wedge-shaped cross-section. These stems achieve proximal metaphyseal fixation primarily through sagittal press-fit stability, with common examples including Taperloc®, Vision®, and SL-PLUS®. Type 2, double-wedge stems, are tapered in both the sagittal and coronal planes, providing enhanced metaphyseal fit in multiple directions. Fixation is achieved through three-dimensional wedge stability, as seen in implants such as Corail®, Summit®, and Bi-Metric®. Type 3, or tapered stems, are defined by a gradual taper along the longitudinal axis and may be straight or slightly curved. They rely on distal diaphyseal engagement to promote axial and rotational stability, with notable examples including AML®, Fitmore®, and Wagner SL®. Type 4 stems have a cylindrical shape with a constant or nearly constant diameter throughout the shaft. They achieve fixation by uniformly filling the diaphyseal canal and transferring load distally; examples include Solution®, Versys®, and AML®. Type 5 represents modular stems, consisting of interchangeable proximal and distal components that allow intraoperative customization of parameters such as neck length, offset, and version. These designs combine the geometric principles of other types with modular flexibility and are particularly advantageous in revision surgeries or cases with complex anatomy or bone loss. Representative examples include S-ROM®, Profemur®, and MODULUS®. Lastly, Type 6 encompasses anatomic stems curved to replicate the natural femoral anatomy, including antecurvature and torsion. These stems achieve a close metaphyseal fit through three-dimensional proximal contact, enhancing load distribution and fixation. Commonly used implants in this category include APTA® (Adler), ABG®, Furlong Active®, and FMP®. Table 1.1 summarizes the Mont classification of cementless femoral stems, outlining their geometry, fixation technologies, and representative examples.

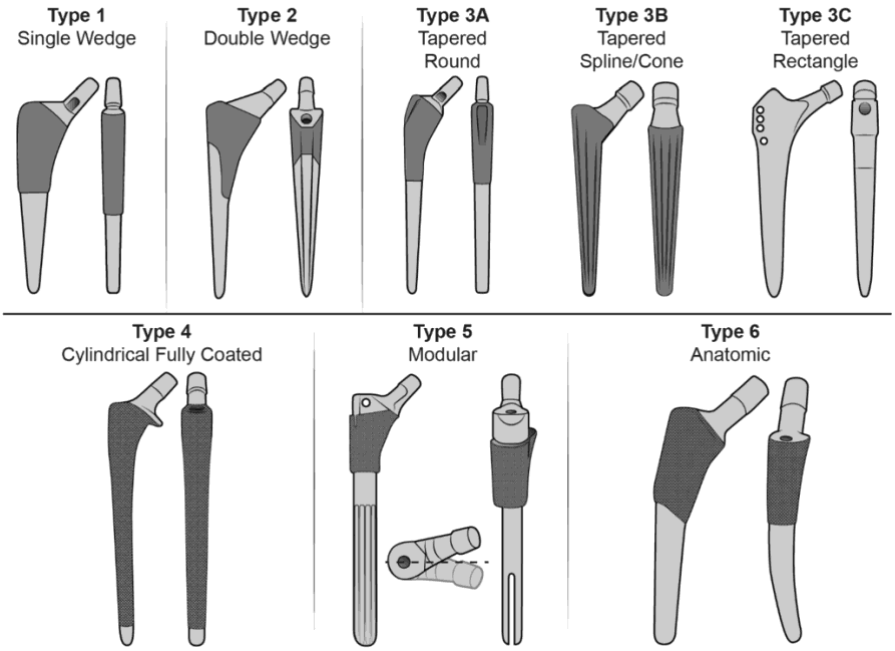

Figure 1.5. Schematic representation of the six types of cementless femoral stems according to the Mont classification. Briefly, types 1, 2, and 3 include those designed to achieve more proximal fixation, with single wedge (Types 1), double wedge (Types 2), and tapered (Types 3) shapes, respectively. Tapered stems are further divided into subclasses based on the geometric shape of the cross-section: round (3a), spline/cone (3b), and rectangle (3c). Type 4 stems are cylindrical and fully coated to achieve more distal fixation. Type 5 includes modular prosthetic stems in which the metaphysis and diaphysis are modular. Type 6 is the anatomic, curved design that matches the proximal femoral endosteal geometry. Reprinted with permission of Springer Nature from [17].

Table 1.1 Mont classification of cementless femoral stems used in primary total hip arthroplasty

Type	Name	Geometry	Fixation	Examples
Type 1	Single wedge	Straight, tapered in one plane (sagittal)	Proximal fixation; full coating allows distal	Taperloc®, Vision®, SL-PLUS®
Type 2	Double wedge	Straight, tapered in both sagittal & coronal	3D metaphyseal press-fit	Corail®, Summit®, Bi-Metric®
Type 3	Tapered (subtypes 3a–c)	Straight, longitudinal taper; cross-section may be round (3a), spline/cone (3b), or rectangular (3c)	Mainly metaphyseal, some diaphyseal support	MS-30®, Fitmore®, CLS Spotorno®
Type 4	Cylindrical	Straight, cylindrical with constant diameter	Diaphyseal fixation	AML®, Solution®, Versys®
Type 5	Modular	Modular neck/stem components	Custom fixation per anatomy	S-ROM®, Profemur®, MODULUS®
Type 6	Anatomic	Curved, mimics natural femoral shape	Proximal anatomical 3D metaphyseal fit	APTA® (Adler), ABG®, Furlong Active®

1.2.2 Fixation approach

Aiming at the firm and durable bond at the interface between the bone and the implant, the fixation approach has long been a key consideration in THA, with three primary options: ***cemented***, ***cementless,*** and ***hybrid fixation***.

Initially, hip implants were designed for ***cementless fixation***, in which the implant is inserted in direct contact with the bone. This method relies on biological integration, whereby the surrounding bone gradually grows into the implant surface to achieve long-term stability. However, early cementless designs featured smooth surfaces that failed to attain solid bridge with the surrounding bone. In the 1960s, John Charnley [19] introduced a new surgical technique of "low-friction arthroplasty" utilizing bone cement, known as polymethylmethacrylate (PMMA). ***Cemented fixation*** involves anchoring the implant to the bone using PMMA, which provides immediate mechanical stability. This innovation represented a significant milestone in the evolution of THA. However, concerns have been raised regarding the long-term durability of this method, as bone cement is not a living tissue and may undergo fatigue-related failure.

It was not until after the 1980s, with advancements in material science, that porous surface technologies were developed and proven effective in promoting bone ingrowth. The Anatomic Medullary Locking (AML) stem was the first extensively porous-coated cementless stem to be widely applied, and it demonstrated successful clinical outcomes [20]. This led to the renewed adoption of cementless fixation, which has gained widespread popularity over the past decade, including acetabular cups and femoral stems [21].

In addition, modern THA also involves ***hybrid fixation***, which refers to the combination technique of a cemented femoral stem and a cementless acetabular cup [22]. ***Reverse hybrid fixation*** consisting of a cementless femoral stem and a cemented acetabular cup has been rarely described in the literature and seldom used in clinics [23].

The optimal choice of fixation strategy in THA is still debated, even though the cementless fixation has become the mainstream approach worldwide. This shift towards cementless might be partly attributed to the trend towards younger THA recipients. Cementless fixation has demonstrated advantages in promoting long-term stability in younger (< 50 years old) and more active individuals [24], [25], [26]. However, in older patients (> 70 years old) with poor bone quality and lower activity demands, cemented fixation reduced the risk of periprosthetic fracture [27], [28]. Furthermore, cemented fixation is highly recommended for patients with hip osteoporosis or fragility fractures [28]. Facing the decline in the use of cemented fixation, the "uncemented paradox" has been proposed, and a study suggested the continuous concern of cemented fixation [29]. Therefore, the fixation strategy in THA should be individualized, considering patient-specific factors such as age, bone quality, and posterior activity expectation.

1.2.3 Surgical management

1.2.3.1 Preparation and preoperative evaluation

Before surgery, proper preoperative preparation and clinical evaluations, including radiographs and CT scans, are necessary. A comprehensive assessment should include evaluation of lower limb mechanical alignment, as well as identification of comorbidities involving the pelvis (e.g., pelvic obliquity), spine (e.g., hyperlordotic conditions), and knee (e.g., flexion contractures), in addition to any gait abnormalities such as Trendelenburg gait. Walking aids are also commonly recommended to reduce hip joint force for better pain management. Furthermore, the American Academy of Orthopaedic Surgeons' Guidelines strongly advise weight loss for patients with a BMI over 25. These non-surgical interventions aim to modify the patient's lifestyle and restore joint mechanics, both of which contribute significantly to the long-term success of the implant.

1.2.3.2 Surgical approaches

The first step in THA involves exposing the hip joint through a selected surgical approach, which enables subsequent removal of the diseased joint structures and facilitates preparation for prosthetic implantation.

The most utilized approaches include: (1) the posterior approach (PA), (2) the direct anterior approach (DAA), and (3) the direct lateral approach (DLA): each presents distinct anatomical pathways and management of the surrounding musculature.

The posterior approach (PA), also known as "*Southern*" or "*Moore*" approach, is the most frequently employed technique worldwide [30]. The main advantage of the PA lies in its ability to preserve the hip abductor mechanism and to provide sufficient exposure of both the acetabulum and the femur. A recent systematic review published in 2023 confirmed its continued predominance, reporting its use in approximately 55.31% of cases [31]. The surgical incision typically begins approximately 5 cm distal to the center of the greater trochanter, along the posterolateral aspect of the femoral shaft. This approach does not follow an actual inter-nervous plane. Instead, it requires splitting the gluteus maximus and detaching the short external rotators, which will compromise muscle integrity. Therefore, some studies pointed out that the PA was associated with a higher risk of postoperative dislocation if the posterior soft tissues are not adequately repaired [32]. However, the literature remains inconclusive, and no consensus has been reached on [33].

The direct lateral approach (DLA) is also called the "*Hardinge*" or "*Transgluteal*" approach. The incision begins approximately 2–4 cm proximal to the junction of the anterior and middle third of the greater trochanter and extends distally 4–6 cm along the femur. This approach involves splitting the hip abductor muscles, including the gluteus medius, to access the joint. As a result, postoperative abductor dysfunction has been a concern, with patients frequently reporting limping and unstable pelvic gait [32].

The direct anterior approach (DAA) has gained popularity in THA due to its muscle-sparing nature, as it utilizes an actual intranervous and intramuscular interval between the sartorius (innervated by the femoral nerve) and the tensor fasciae latae (innervated by the superior gluteal nerve). It is considered a minimally invasive technique, associated with reduced postoperative pain and potentially faster early recovery. However, intraoperative fractures, particularly of the greater trochanter, have been noted as a notable complication. This risk arises primarily from the aggressive femoral elevation required to achieve adequate femoral exposure, which imposes significant mechanical stress on the proximal femur and adjacent soft tissue structures.

In addition to the above traditional surgical approaches, alternative techniques such as the *Watson-Jones approach*, the two-incision approach, and the superior gluteal approach have also been applied in THA. The *Watson-Jones approach*, called "*anterolateral approach*", is an accurate intermuscular and intranervous technique. It accesses the hip joint through the interval between the gluteus medius and the tensor fasciae latae, thereby preserving the gluteus medius and minimizing trauma to the hip abductor mechanism. However, the term "anterolateral approach" has been inconsistently used in the literature, referring either to an intermuscular approach between the gluteus medius and tensor fasciae latae *(Watson-Jones type)*, or to a transmuscular approach involving partial detachment of the gluteus medius *(Hardinge type)* [34]. It is essential to distinguish between the two clearly, as only the Watson-Jones approach preserves the abductor muscles.

Despite the extensive use of these various techniques, high-quality evidence that directly compares outcomes across approaches [33] remains lacking. As such, most guidelines recommend that the surgical approach be tailored to the surgeon's experience and the patient's individual factors.

1.2.3.3 Surgical procedures

After the surgical approach, standard procedure steps should be followed once the hip joint is adequately exposed.

Step 1: Femoral Neck Osteotomy and Acetabular visualization

A femoral neck osteotomy is performed using a reciprocating saw according to the pre-operative plan. The resection plane is usually above the lesser trochanter, following the proximal-lateral direction, with the preservation of the greater trochanter. Once the neck is fully osteotomized and the femoral head is mobilized, the acetabulum is visualized using retractors placed medially and laterally to provide clear exposure.

Step 2: Acetabular installation

The femoral head is extracted using a corkscrew device, removing any residual soft tissue attachments. The limb is gently rotated while maintaining medial retraction to preserve visualization. The acetabular cup is implanted using an offset inserter handle, which helps minimize soft tissue impingement during insertion.

Step 3: Femoral Canal Preparation

Depending on implant design, the femoral canal is sequentially prepared using a rasping or broaching system. A specialized bone hook is placed at the posterior aspect of the proximal femur, near the insertion of the gluteus maximus, to manually elevate the femur anteriorly. An offset broach handle facilitates access to the canal. Rasping is continued until optimal press-fit stability is achieved. The calcar is contoured and levelled to match the final rasp position, ensuring proper seating of the implant shoulder.

Step 4: Trial the femoral stem in place

After the trial femoral stem is positioned, the hip is reduced using standard or high-offset trial components. Most implants offer various trial sizes (e.g., plus or minus options) to optimize fit and biomechanics based on intraoperative assessment of leg length, joint stability, and range of motion.

Step 5: Femoral Stem Insertion

The final femoral stem is inserted using a stem-holder. The final impactor-guide is attached to ensure accurate press-fit seating, and the implant is advanced into the femoral canal using controlled mallet blows. An extraction hook may adjust the stem depth or orientation if repositioning is required.

1.2.4 THA registry

Joint replacement registries are indispensable for enhancing prosthesis traceability, supporting research and development in implant technologies, and monitoring epidemiological trends. Previous studies have systematically reviewed existing European hip and knee replacement registries [35] and globally [36]. The first national registries for knee and hip arthroplasty were founded in Sweden in 1975 and 1979, respectively. In Italy and Switzerland, hospital-based or region-level registries were initiated earlier than national counterparts. To date, there are around 24 joint replacement registries covering 15 European countries, which have recorded more than 3 million hospital admissions for primary THA. In the United States, the development of a nationwide joint replacement registry began around 2000 as well, eventually leading to the establishment of the American Joint Replacement Registry (AJRR) in 2009. According to publicly available reports, over 1 million primary THAs were performed annually worldwide [37]. Furthermore, considering an ageing society, osteoarthritis prevalence, and the increase in obesity rate, there is a unified view that the demand for joint replacements will continue to rise over the next 20 years across different countries [38], [39], [40], [41], [42], [43], [44], [45].

Given the tremendous volume of registry data and the diversity of implant designs, the fixation method is commonly used as a key taxonomy criterion in registry-based analyses. Cemented and cementless designs were distinguished in many reports. The American Academy of Orthopaedic Surgeons (AAOS) reported that only 2.7% of primary THAs utilized cemented stems from 2012 to 2021. Australian Orthopaedic Association (AOA) Registry noted that cementless fixation has increased from 51.3% in 2003 to 61.6% in 2021. Hybrid fixation has risen from 34.8% to 36.3% and cemented fixation has declined from 13.9% to 2.1%. In Sweden,

the use of cemented fixation is relatively high, 52% in 2021, compared to other countries. Still, the Swedish register also commented that completely cementless fixation of both cup and stem has increased from 2% in 2000 to 32% in 2021.

The clinical database supporting this thesis is from Registro dell'Implantologia Protesica Ortopedica (RIPO registry) in Italy, a regional registry dedicated to the Emilia-Romagna region with a population of over 4 million. From 2000 to 2021, RIPO collected a total of 146,918 primary THAs. As reported, cementless fixation has become increasingly popular over time: its usage rose from 60% in 2000 to 95% in 2021, indicating a consistent annual increase throughout the two decades. 131,852 involved uncemented femoral stems were implemented, accounting for approximately 90% of the primary THAs in the latest report. Of these were 48 cemented stem designs and 76 cementless stem designs. Notably, 11,239 uncemented APTA Adler® femoral stems—representing 9% of all uncemented stems—were identified, making it the most used design in the registry. Survival analysis has shown that the 10-year survival rate of APTA Adler® implants reaches approximately 97%. APTA Adler® femoral stems are the primary focus of the present thesis.

1.3 Failure modes of hip joint replacement

While THA is a durable and effective procedure, several failure mechanisms may compromise long-term outcomes. Failure mode involves aseptic loosening, wear, periprosthetic fractures, dislocation, periprosthetic joint infection, osteolysis from wear debris, and metal hypersensitivity reactions. These complications can arise from a combination of factors, typically influenced by patient-related factors (e.g., bone quality, age, lifestyles), surgical technique (e.g., surgical approaches, implant positioning, soft tissue handling), and implant characteristics (e.g., material properties, geometry, surface coating, and fixation method).

1.3.1 Failure Modes

From a temporal perspective, implant failures can be broadly categorized into three stages: **intraoperative**, **early postoperative (short-term)**, and **mid- to long-term** failures.

- **Intraoperative failures** mainly involve iatrogenic femoral fractures, which are more frequently observed during the insertion of cementless stems, particularly in patients with poor bone quality or abnormal anatomy. Although not the most common mode of failure, iatrogenic femoral fractures can complicate initial fixation and increase the risk of future loosening.
- **Short-term failures**, occurring within the first few weeks to months after surgery, often include periprosthetic joint infection, dislocation, or hypersensitivity reactions to implant materials. These complications can severely compromise early implant stability, especially when infection leads to septic loosening, repeated dislocation from poor implant alignment, or insufficient soft tissue tension.
- **Mid- and long-term failures**, from months to years after implantation, are dominated by aseptic loosening (AL)—the most common cause of late THA failure.

1.3.2 Aseptic loosening

Aseptic loosening is described as the implant losing its mechanical stability with respect to the host bone in the absence of infection, often accompanied by periprosthetic osteolysis (bone resorption) and inflammatory cellular response within the joint. Much evidence on the mechanics of AL was observed, but it's hard to attribute it to a single cause. The following sections provide a detailed discussion of the mechanisms of AL, with particular attention to differences between cementless and cemented fixation techniques.

1.3.2.1 Cemented Aseptic Loosening

- Bone–cement interface

Two principal mechanisms have been proposed to account for the adverse biological and mechanical outcomes of PMMA, bone cement. First, thermal necrosis at the bone–cement interface may occur due to the exothermic nature of the polymerization reaction. Early cement formulations lacked precise thermal control, and the heat generated during curing can reach levels sufficient to induce osteonecrosis in adjacent bone tissue. This devitalized bone is gradually resorbed and replaced by fibrous tissue, compromising the mechanical integrity of the fixation and predisposing the implant to loosening over time. Second, the cytotoxicity of residual monomers represents a significant concern. PMMA is formed through methyl methacrylate (MMA) polymerization, initiated by mixing a liquid monomer with a powder catalyst. Incomplete polymerization can leave unreacted MMA monomers embedded within the cured cement. These residual monomers provoke local inflammation and cellular toxicity, undermining tissue integration and implant stability.

To address these issues, modern bone cements incorporate additives and stabilizers that precisely regulate the polymerization kinetics, temperature control, and reaction completeness, thus improving both mechanical performance and biocompatibility.

- Stem-cement interface

In some instances, fixation failure extends beyond the bone–cement interface to the junction between the femoral stem and the cement mantle. Unlike bone, PMMA is an inert material that cannot form a biological bond with the implant surface. As a result, cyclic loading during daily activities can lead to micromovements between the metallic stem and the surrounding cement, a phenomenon known as fretting. These micro-motions cause mechanical abrasion at the stem–cement interface, producing wear debris of metallic particles and polymer fragments. Over time, these particles may migrate into the periprosthetic joint space, triggering an inflammatory response in the surrounding soft tissues—a pathological condition called metallosis. This tissue reaction mirrors that seen in MoM articulations bearing surface and can further compromise implant longevity and patient outcomes.

1.3.2.2 Cementless aseptic loosening

Cementless fixation THA relies on bone ingrowth for long-term stability. Failure of osseointegration due to poor initial fixation or excessive micromotion at the interface can form fibrous rather than bony tissue, significantly reducing secondary stability and leading to loosening over time. Even a thin fibrous layer has been shown to interfere with osseointegration across most of the implant surface. Furthermore, wear debris-induced osteolysis is a major contributor to long-term loosening in both fixation methods, as particulate debris can stimulate macrophage-mediated bone resorption around the implant.

Different implant designs show considerably different incidence of AL. For cementless acetabular components, a large cohort study involving 12,800 primary THAs reported a five-year revision rate for AL of only 0.1% in implants with trabecular metal coatings, compared to 0.2% in non-trabecular metal-coated control implants, suggesting superior performance of trabecular designs [46]. Similarly, a separate analysis of 20,993 cases demonstrated that highly porous titanium-coated acetabular cups are associated with low AL rates during long-term follow-up [47]. However, not all porous coatings yield consistent results; another study found that ultra-porous-coated (Titanium) acetabular components showed a higher revision risk than the control group [48]. For the cementless femoral stem, a survey of 517 THAs showed that some shorter and shoulder-less double-taper press-fit stems have a high rate of AL (1,4% at five years) [49]. Revision rates for smaller Corail stems (Titanium; straight stem) are four times higher than those for larger femoral diameters [50]. At 4.5 years, the estimated probability of revision for AL for Bio-Fit stem (cobalt-chromium; straight stem) was 18.6%; for the Corail stem (Titanium; straight stem) was 0.5% [51].

A meta-analysis by Keurentjes et al. further evaluated the 10-year cumulative survival of cementless acetabular components and femoral stems [52]. The following cementless acetabular components demonstrated less than 2% incidence of AL at 10 years: Trabecular Metal Monoblock®, Fitmore®, Conserve Plus®, Morscher Press Fit®, Zweymuller-Alloclassic Screw Cup®, Arthropor®, ACS Triloc+®, Titan®, and Spectron®. The following cementless stems demonstrated excellent long-term outcomes, each achieving a survivorship rate (AL as an endpoint) exceeding 96%: ABG I, Osteonics Cementless, R-B Interlok, Zweymuller-Alloclassic, Freeman Cementless, Stanmore Custom Made, MS-30, Corail, Profile Porous, Bi-Metric, Mallory-Head Cementless, Taperloc, and Titan stems. However, ten-year survival rates for the Lubinus SP II and Interlok femoral stems were only 92% and 94%.

Chapter 2

Experimental Studies of Aseptic Loosening

As the most common failure mode in total hip arthroplasty (THA), aseptic loosening severely compromises the longevity of prosthetic implants. Patients undergoing aseptic loosening after THA may present with a wide spectrum of clinical manifestations. In mild cases, the condition can remain asymptomatic, whereas in severe cases it is often characterised by progressive impairment of joint function accompanied by localised pain. Clinical evaluation begins with a detailed medical history and physical examination. Typical symptoms include gait pattern abnormalities, painful restriction of the range of motion, limitation

s in walking ability, and limb length discrepancy due to femoral subsidence. Notably, pain associated with loosening of the femoral stem is generally more pronounced and disabling than that arising from the acetabular component [53]. In the worst cases, complex and invasive revision surgery may be required, which imposes substantial clinical and economic burdens. Because the success rate of revision procedures declines significantly with each subsequent revision over time [54]. These adverse outcomes have drawn attention from both clinicians and engineers, motivating a spectrum of research efforts dedicated to understanding and preventing aseptic loosening.

The mechanism of aseptic loosening of THA prostheses is complex and not fully understood. In most cases, the aetiology is combinatorial, occurring as a result of inadequate initial mechanical fixation (*primary stability*) or biological bonding loss over time (*secondary stability*). For modern cementless implants, large stress shielding or massive wear is uncommon, and loosening is predominantly linked to the large relative micromotion at the bone-implant interface [55]. Specifically, physiological loading induces over 100 to 200 μm relative micromotion, which was found to prevent osseointegration and instead promote the formation of a fibrous tissue layer surrounding the implant. This, derived largely from in-vitro studies on implants within cadaveric specimens, has led to the adoption of ≥150 μm as the reference "biological threshold" for predicting the occurrence of loosening [56]. The threshold is frequently cited in the context of radiographic evaluations, mechanical bench tests, and computational models for the implant stability studies in cementless femoral implants.

Despite its widespread use, the practical application of this threshold remains challenging for the implant's *primary stability* assessment. Radiographic techniques, while clinically accessible, have limited accuracy and reproducibility when attempting to resolve micromotion at such small scales. As Viceconti et al. emphasised [57], if the biological threshold is indeed within the 100–200 μm range, then methods for evaluating *primary stability* must achieve a resolution of at least 10–20 μm and capture displacement across the entire implant–bone interface. Current experimental approaches often fall short of the criteria, offering only partial or localised measurements, and they provide limited flexibility for the evaluation of novel implant designs or patient-

specific surgical scenarios. To overcome these limitations, computational modelling has emerged as a powerful complementary tool. In particular, nonlinear contact analysis with finite element (FE) techniques enables detailed characterisation of the contact behaviour between implant and bone, to predict relative micromotion at the whole contact area. These models therefore provide a means not only to assess implant designs under controlled conditions but also to support preoperative planning by offering insights that are difficult to achieve with experimental or radiographic methods alone.

Moreover, the risk of aseptic loosening in cementless hip stems can be reduced by promoting osseointegration, thereby ensuring a stronger bond between the bone and the metallic implant and favouring long-term stability (*secondary stability*). In other words, long-term fixation is achieved when bone grows into, or directly bridges with, the implant surface. To this aim, novel implant surface structures and coating materials have been developed to stimulate bone ingrowth. Since the process of osseointegration is governed by complex chemical and biological interactions at the bone–implant interface, numerous animal studies have been conducted to investigate the performance of various surface modifications and coating technologies in enhancing bone ingrowth and osteo-inductive responses. Ideally, computational models were then employed to translate results from animal studies to human femoral implants, providing a patient-specific framework to assess long-term stability under clinically relevant conditions.

Overall, existing studies cover multiple complementary perspectives to assess and predict the occurrence of aseptic loosening, including large-scale clinical retrospective analyses aimed at identifying risk factors through the joint replacement registries (discussed in Chapter 1: section1.2.4 & 1.3.2); advanced imaging approaches for early diagnosis and monitoring of implant instability; in vivo and in vitro experiments that investigate the biomechanical and biological mechanisms at the bone–implant interface; validated computational models that predict the failure risk; as well as animal studies that provide translational insights. This chapter will provide a comprehensive discussion of these approaches, particularly outlining the art of state for aseptic loosening in cementless hip implants and the development of technologies that researchers focus on, including the implant's *primary stability,* from *in vivo, in vitro* and *in silico*. The following Chapter 3 will then address patient-specific computational models of osseointegration, which represent a rapidly evolving methodology for predicting long-term implant stability and assessing the risk of aseptic loosening in individual patients.

2.1 Radiographic evaluations for aseptic loosening

2.1.1 Conventional radiography (plain X-ray)

Currently, in clinics, aseptic loosening after THA is often assessed indirectly through the imaging modality of choice. The most commonly used imaging modality for the evaluation of aseptic loosening is conventional radiography (plain X-ray). Standard practice includes obtaining an anteroposterior (AP) view of the pelvis as well as lateral views of the affected hip, which allow the detection of prosthetic displacement in multiple directions. Spot welds are radiographic signs of osseointegration, and their presence is crucial for confirming biological fixation of cementless prostheses. While signs of loosening can often be identified by comparing postoperative radiographs with either preoperative baseline images or serial follow-up examinations. A prosthesis surrounded by a circumferential radiolucent line (RLL) greater than 2 mm in thickness, in combination with evidence of subsidence over than 1 cm or migration, is generally considered diagnostic of loosening [58]. Determination of femoral stem loosening zones is usually described according to Gruen Classification [59] in the pelvis AP X-ray. These zones include the greater trochanter (Zone 1), lateral mid-stem (Zone 2), lateral distal stem (Zone 3), the tip of the stem (Zone 4), the medial distal stem (Zone 5), the medial mid-stem (Zone 6), and the medial calcar (Zone 7), as shown in Fig.2.1. According to the classification proposed by Charnley-Delee [60], abnormal cup positioning is typically localized within three distinct zones.

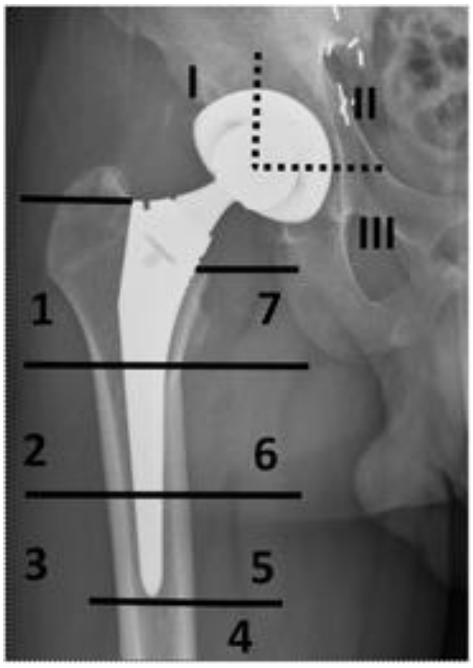

Figure 2.1. Standardised template for radiographic assessment of periprosthetic radiolucency, with three acetabular zones (I–III) and seven femoral zones (1–7). Reprinted with permission of Springer from [61].

The diagnosis and monitoring of prosthetic loosening remain challenging, and a definitive diagnosis can only be confirmed intraoperatively in some cases. Therefore, the predictive value of radiographic abnormalities for the prostheses' failure mode of aseptic loosening was investigated by a few studies [62], [63], [64], [65], [66],

[67], [68]. In 1994, Vresilovic et al. [63] proposed that the order of significant radiographic signs correlated with instability of cementless femoral components: radiolucent lines at the bone-prosthesis interface covering greater than 50% of the porous implant interface, a distal pedestal, calcar hypertrophy, poor implant-cortical contact, and varus component alignment. An 8- to 12-year follow-up study [65] of cementless femoral stem emphasised that radiographs obtained 2 years postoperatively may be valuable in predicting the long-term survival of cementless porous-coated hip stem. Radiolucent line was more frequently observed in all Gruen zones on radiographs in the revision group (caused by aseptic loosening). Radiolucent lines visible exclusively on the lateral view were identified as a statistically significant predictor of future revision (P = 0.001). The presence of RLLs around the porous coating predicted the need for revision with a sensitivity of 100% and specificity of 55%, whereas the absence of RLLs around the porous coating predicted freedom from revision within 8 years with a sensitivity of 100% and specificity of 45%. Another longitudinal follow-up study [66] involving more than 1,300 patients after primary THA reported that abnormal radiographic findings at five years were strongly associated with subsequent revision for aseptic loosening, particularly in patients younger than 60 years. Some studies found radiographic signs associated with instability and lack of osseointegration occur in clinically asymptomatic patients [62], [68], which supports their predictive value for implant failure. However, concerns for the accuracy of X-ray remain, for example, the phenomenon of radiographically silent loosening [69]. Limitations of conventional X-rays are generally from the lack of spatial resolution in the depth direction or observation variability. Accurate comparison of serial radiographs is challenging if the images are not acquired with consistent projection angles or degrees of limb rotation, and inter-observer agreement may be poor [64], [70] according to the surgeon's clinical experience.

2.1.2 Advanced imaging modalities

To address the shortcomings of plain radiography, and considering that implant mechanical loosening typically begins with micromotions of 0.2–1 mm [71], several advanced imaging modalities have been proposed for more reliable detection, including radiostereometric analysis (RSA), dual-energy X-ray absorptiometry (DEXA), computed tomography (CT), magnetic resonance imaging (MRI), and nuclear medicine imaging.

Radiostereometric analysis (RSA), also known as roentgen stereophotogrammetry, is a technique based on biplanar or multiplanar radiographs used to perform precise three-dimensional measurements. By inserting small metallic markers, usually tantalum beads, into the bone or implant and acquiring radiographs from different angles, computer algorithms can reconstruct the exact three-dimensional positions of these markers, enabling highly accurate quantification of implant–bone micromotions. The reported accuracy of RSA ranges from 0.05 to 0.5 mm for translational movements and from 0.15° to 1.15° for rotations, allowing detection of early implant migration [72]. Compared with conventional radiography, RSA offers lower radiation exposure. A review[73] on the predictive value of RSA for implant loosening emphasised that this technique enables the early identification of excessive implant migration with small patient cohorts over short follow-up periods. This may make RSA suitable for preclinical evaluation of new prosthetic designs, and its potential role in

regulatory approval processes is increasingly being recognised [74]. Current research efforts are directed toward the development of marker-less RSA, which could allow migration and wear measurements in larger patient cohorts during routine clinical follow-up [75]. Nevertheless, limitations included a lack of standardisation regulation regarding radiation dose, follow-up intervals, number and size of marker beads, and imaging protocols.

Dual-energy X-ray absorptiometry (DEXA) provides quantitative measurements of periprosthetic bone mineral density (BMD). Notably, the measurement error of DEXA for periprosthetic BMD was reported to be less than 1% [76], [77], [78], underscoring its high accuracy for longitudinal monitoring. It is widely used in research to monitor changes in BMD around implants and to assess the influence of different implant materials or designs on osteointegration and bone remodelling [79]. However, DEXA isn't the primary diagnostic tool for aseptic loosening; it requires further research to correlate measurements of regional BMD with the presence or absence of aseptic loosening.

Both computed tomography (CT) and magnetic resonance imaging (MRI) can provide three-dimensional imaging and reconstruction. CT offers high-resolution visualisation of cortical and trabecular bone but involves higher radiation exposure compared with plain radiography. MRI enables soft-tissue modelling, distinguishing bone and fibrous tissue, the latter being one of the signs of aseptic loosening at the bone implant interface. However, they are both likewise susceptible to metal-induced artefacts. Some innovations based on CT or MRI imaging were proposed. For example, inducible displacement CT has been reported to improve the diagnostic accuracy of aseptic loosening in primary THA [80]. This method involves paired CT scans acquired at the extremes of motion, with the femur positioned in maximum internal and external rotation [80], [81]. Implant failure was determined based on intraoperative definitive findings, identifying cases of loosening. For plain radiography, the sensitivity and specificity were 59% and 85%, respectively. In comparison, displacement CT demonstrated higher diagnostic performance, with a sensitivity of 77% and a specificity of 100%.

In addition, technical advances in metal artefact reduction (TMAR) [82] were developed to enhance 3D medical image quality and precisely evaluate the postoperative condition. Tomosynthesis, also digital tomosynthesis, is a method for performing high-resolution limited-angle tomography at a low-dose radiation comparable with plain radiography. It has been shown to reliably identify circumferential radiolucent lines as thin as ≤ 2 mm around the prosthesis, thereby enabling the diagnosis of implant loosening even in the absence of detectable displacement. A study [83] demonstrated that both TMAR and conventional CT exhibited significantly higher sensitivity than plain radiography in detecting radiolucent lines of varying widths surrounding cementless femoral stems.

Nuclear medicine imaging has been proposed as a potential tool in the diagnosis of prosthetic loosening, particularly in challenging or inconclusive cases. Some authors have suggested that radionuclide arthrography (RNA) should be considered a useful supplementary tool for detecting implant loosening in difficult-to-diagnose patients [84], [85]. However, studies comparing the diagnostic value of plain radiography (X-ray), digital subtraction arthrography (DSA), and RNA—using intraoperative findings as the reference standard—

reported that plain radiography remained the most effective modality, whereas subtraction arthrography and radionuclide arthrography were not suitable as routine diagnostic tools for detecting loosening after total knee arthroplasty [86]. Evidence suggested that nuclear imaging may still contribute diagnostic value when used in combination with conventional radiography [87]. Multivariate regression analysis demonstrated that bone scintigraphy and radionuclide arthrography, when combined with plain radiography, significantly improved diagnostic accuracy. Nevertheless, it is worth noting that these studies were limited by relatively small case numbers, and inspection tools based on nuclear medicine imaging are often invasive and expensive.

2.1.3 Imaging modalities assisted with machine learning

With the rapid development of artificial intelligence, radiographic studies employing machine learning algorithms have shown promising results in identifying loosening around THAs [88], [89], [90], [91]. Researchers proposed a fully automated and interpretable method based on deep convolutional neural networks (CNNs), aiming to overcome the poor inter- and intra-observer reliability and limited accuracy of manual detection of mechanical loosening based on X-ray. Using five-fold cross-validation on paired pre- and postoperative radiographs of 40 patients [91], the CNN was trained and its performance compared with that of multiple board-certified orthopaedic surgeons. The CNN demonstrated superior diagnostic performance, with a significantly higher sensitivity and equivalent specificity. Machine learning has therefore been suggested as a potential adjunct in prosthetic loosening screening programs [92]. But it should be noted that the algorithm was developed using radiographs from patients with either confirmed implant loosening at revision surgery or stable implants after primary THA and has not yet been validated in cases with suspected but unconfirmed loosening.

In summary, the diagnosis of aseptic loosening requires targeted clinical evaluation combined with comprehensive imaging assessment using multiple modalities. At present, no imaging-specific algorithm exists for the detection of loosening failure in THA [93]. Although conventional radiography has certain limitations, it is the most cost-effective method. In addition, there are differences in the agreement between the expert physicians who evaluated the cases, which is related to the technical limitations of radiography. However, it is important to note that the stability of the THA is a long-term result, especially since the process of osseointegration in cementless implants lasts for more than 24 months. Therefore, leveraging the complementary strengths of various imaging modalities and ensuring regular follow-up—particularly within the first 2 to 5 years after cementless hip arthroplasty—is essential for reliable monitoring.

2.2 Experimental measurement of micromotion

Early investigations suggested a limit of micromotion at 150 μm, which over time has become widely cited as the “gold standard.” In 1992, a post-mortem retrieval study of human femora implanted with Anatomic Medullary Locking (AML) stems reported that a maximum relative micromotion of approximately 40 μm was

compatible with bone ingrowth [56]. Numerous animal studies were conducted in an attempt to establish the threshold for osseointegration. Animal experiments [94] demonstrated that micromotion exceeding 150 μm completely inhibited bone ingrowth by promoting the formation of fibrous connective tissue, whereas thresholds of approximately 28 μm and 40 μm were proposed as the upper limits below which stable osseointegration could reliably occur. A systematic review [95] that summarised twenty-four animal studies reported that the mean micromotion of implants with bone ingrowth was 32% of that observed in non-integrated implants (112 μm vs 349 μm). Although several in vivo studies—mainly animal experiments—have attempted to define the permissible threshold for osseointegration, most of the available evidence is still derived from in vitro or ex vivo measurements. This section will discuss the measurement approaches, loading protocols of the mechanical bench test and the implant-related results.

2.2.1 In vitro test

In vitro techniques for monitor relative micromotion at the bone–implant interface have primarily relied on Linear Variable Displacement Transducers (LVDTs). Most studies have been performed on composite or cadaveric femora to assess micromotion at predefined measurement points on the implant surface [96], [97], [98], [99], [100], [101], [102], [103], [104], [105], [106], [107], [108]. The standard setup involves drilling small transcortical holes to insert metallic pins, which serve as contact points for the LVDT probes, thereby allowing measurement of stem relative displacement to the surrounding cortex under mechanical loading, as shown in Fig.2.2. To avoid cortical perforation, a variant of the LVDT technique was developed using a six degrees-of-freedom system [107]. This system measured micromotion in six composite femora implanted with cementless stems and consisted of six LVDTs mounted on a rigid frame connected to the implant via a flexible coupling. Displacements were recorded relative to a target device comprising three steel spheres attached to the femoral component. Implants were subjected to cyclic loading using a hydraulic fatigue testing machine to simulate physiological conditions. The device consistently measured micromotion across repeated cycles, maintained accuracy under controlled environmental factors such as temperature fluctuations, and was further validated against finite element model predictions. This setup demonstrated strong potential for extended testing and was found suitable for the preclinical evaluation of cementless hip implants. In 2011, Gortchacow et al. [109], [110] proposed a micro-computed tomography (μCT) technique for locally measuring relative micromotion between a metallic femoral stem and the surrounding bone. In this approach, tantalum beads were attached to the stem surface and distributed across the inner cortical surface of the femur. Relative displacements between the implant and the bone were then quantified under different loading magnitudes. It was reported that the micromotion measurement error of this method was approximately 10 μm. Under loading up to 1400 N, peak micromotion along the loading direction was found to be 60 μm. The key advantage of this technique is its ability to capture local displacements at multiple points across the entire implant surface, rather than being restricted to a few predefined positions [110]. In vitro micromotion measurement at the bone-implant interface of cementless femoral prosthesis is summarised in Table 2.1. As indicated in the table, certain experimental

investigations were subsequently adopted as reference datasets for the validation of finite element (FE) models. A comprehensive description of FE models dedicated to the quantification of interfacial micromotion will be discussed in Section 2.4.

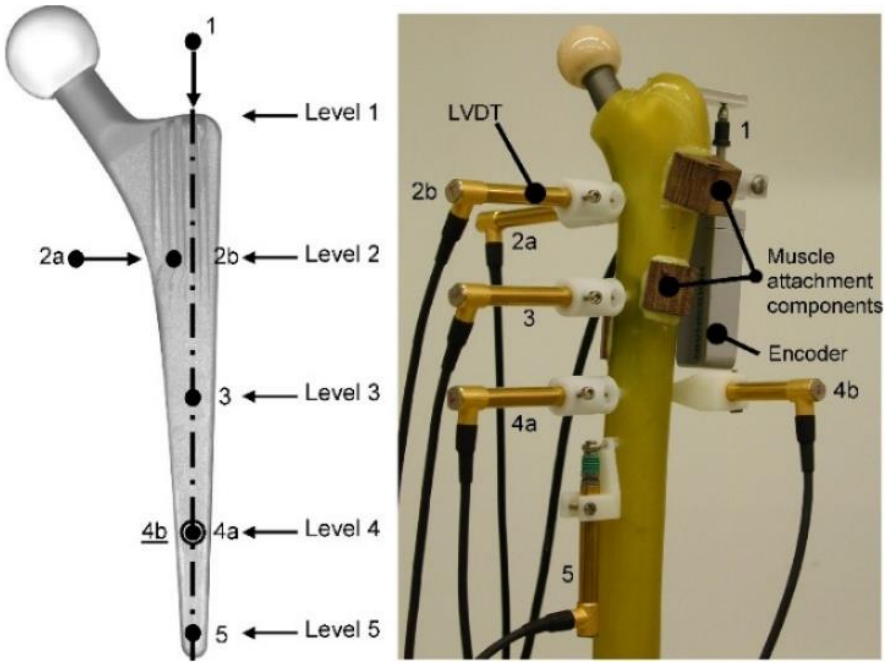

Figure 2.2. Measurement locations selected to determine the micro-movements at the bone–prosthesis interface (left) and medio-lateral view of the proximal part of a composite femur implanted with a cementless CLS stem and instrumented with one linear encoder (1) and six LVDTs (2a, 2b, 3, 4a, 4b and 5) to measure the interface micro-motion (right). Reprinted with permission of Elsevier from [105].

Table.2.1 In vitro micromotion measurement and finite element models validation for primary stability at the bone-implant interface of cementless femoral prosthesis.

Study	Implants	Technology to Measure Micromotion	Loading Protocol		Include FE model
Monti et al. [111] 1999	AncaFit (Cremascoli Ortho, Italy)	4 LVDT sensors attached to pegs inserted through the cortical bone	Stair climbing	Axial compressive force (275–1,683 N), the torque (5–26 Nm), and the bending moment (3–23 Nm).	N/A
Viceconti et al. [102] 2001	AncaFit (Cremascoli Ortho, Italy)	4 LVDT sensors attached to pegs inserted through the cortical bone	Stair climbing	Torsional moments of 19.8 Nm applied.	Including FE model, also reported in [57]
Götze et al. [103] 2002	A custom-made stem (Freiburg, Germany)	4 LVDT sensors attached to pegs inserted through the cortical bone	Single-leg stance	Vertical load 2000 N with frequency of 0.5 Hz	N/A
Cristofolini et al. [112] 2006	AncaFit® modified (Arlington, TN, USA)	2 LVDT sensors arranged without perforation of the cortical bone	Stair climbing	Torsional moments of 15–25 Nm applied.	FE model reported in [113], [114]
Kassi et al. [105] 2005	CLS® Spotorno (Winterthur, Switzerland)	6 LVDTs sensors attached to pegs inserted through the cortical bone and an optical encoder.	Walking and stair climbing at 50% or 75% gait cycle	Vertical load 1000 N; for walking, 1062 N or 1593 N; for stair climbing, 1174 N or 1761 N.	N/A
Abdul-Kadir et al.[99] 2008	Alloclassic (Zimmer GmbH, Winterthur, Switzerland)	2 LVDT sensors attached to pegs inserted through the cortical bone	Stair Climbing	A cyclical axial compression load of 0–2000N and triangular waveform.	Including FE model
Pettersen et al. [107] 2009	Summit™ (DePuy, Leeds, UK)	6 LVDT sensors arranged without perforation of the cortical bone	Stair Climbing	600 N axial load combined with torsional moments of 13.5 Nm	Including FE model
Fottner et al. [100] 2009	Thrust Plate Prosthesis (Zimmer, Warsaw, Indiana, USA); Mayo (Zimmer, Warsaw, Indiana,	6 LVDT sensors arranged without perforation of the cortical bone	Walking	Vertical load 300–1700 N (70 kg); A sinusoid dynamic with frequency 1 Hz.	N/A

	USA); Metha (Aesculap, Tuttlingen, Germany)				
Ostbyhaug et al. [98] 2010	ABG-I (Allendale, NJ, USA); *Unique*® customized stem (SCP, Trondheim, Norway)	6 LVDT sensors arranged without perforation of the cortical bone	Stair Climbing	600 N axial load combined with torsional moments of 15 Nm	N/A
Fottner et al. [101] 2011	CLS® Spotorno (Zimmer, Warsaw, USA)	6 LVDT sensors arranged without perforation of the cortical bone	Walking	Vertical load 100–1700 N; a sinusoid dynamic with frequency 0.5 Hz.	N/A
Gortchacow et al. [109], [110] 2011	Harmony Straight Stem and SPS Anatomical Stem (Symbios Orthopedie SA, Switzerland)	Micro-CT tracking 12 tantalum and 500 stainless steel markers	N/A	Vertical load 2000N	N/A
Bieger et al. [96] 2012	Fitmore, a short stem; CLS®, a straight, standard-length stem; Mayo, a short, bone-preserving stem	6 inductive miniature displacement transducers inserted through the cortical bone	Single-leg stance	Vertical load 100–1600 N; a sinusoidal load with frequency 2 Hz	N/A
Bieger et al. [97] 2016	2 Zweymüller-type straight stems: CBH and the CBH bone preserving (Mathys medical, Bettlach, Switzerland)	6 inductive miniature displacement transducers inserted through the cortical bone	Single-leg stance	Vertical load 100–1600 N; a sinusoidal load with frequency 2 Hz	N/A
Schmidutz et al. [115] 2017	3 sizes of CLS® Spotorno (Zimmer, Warsaw, USA)	6 LVDT sensors arranged without perforation of the cortical bone	Walking	Vertical load 250–1416N; a sinusoid dynamic with frequency 0.5 Hz.	N/A

Generally, micromotion was measured within specific regions of interest (ROIs), for example, as shown in Fig.2.2, the study defined seven predefined sites across five levels of composite femora, ranging from the prosthetic shoulder to the distal tip [105]. Positions were distributed on the anterior, medial, and posterior surfaces, with subscripts distinguishing multiple sites at the same level. Motion was recorded in the proximal–distal direction, in the medial–lateral direction, and in the anterior–posterior direction. Transcortical holes (5 mm) were drilled at the corresponding locations to capture relative micromotion at the bone–implant interface. The network meta-analysis [116] indicated that micromotions at the proximal stem were generally comparable across all four anatomical directions, suggesting a relatively uniform stability in this region. At the mid-stem, the highest relative displacement was observed at point P7, whereas at the distal stem, micromotion peaked at point P10, with distal values overall exceeding those measured at the middle and proximal regions. Across the implant–bone surface, point P13 showed the greatest micromotion. In terms of directional trends, medial micromotions appeared to be greater than those observed proximally, while lateral values did not exhibit a marked difference, as shown in Fig.2.3.

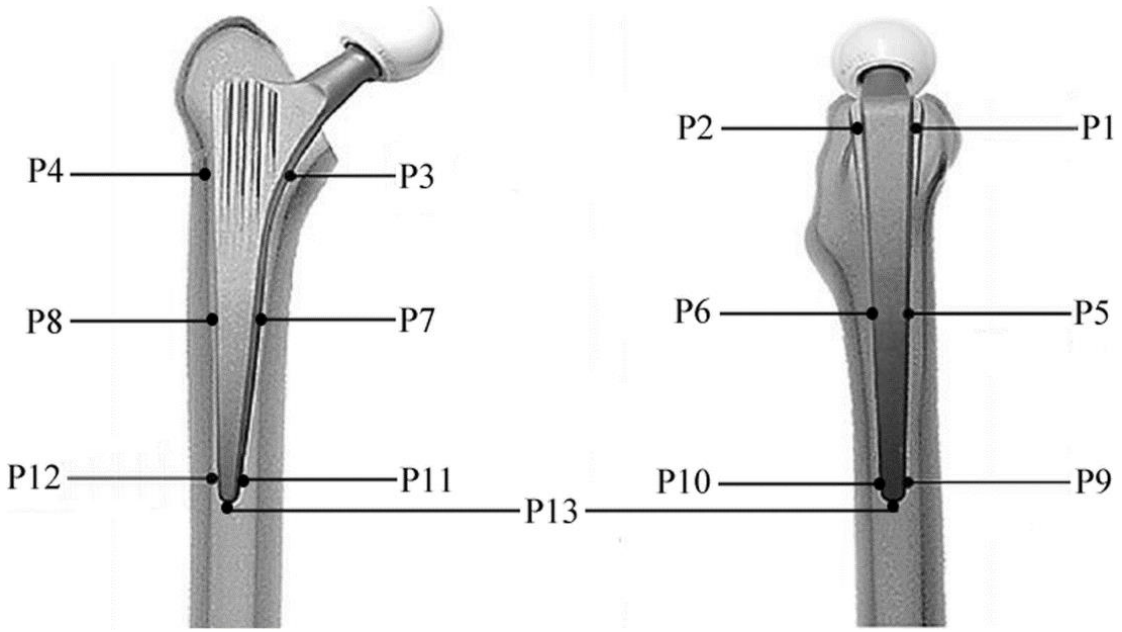

Figure 2.3. The schematic diagram of measuring micromotions of 13 measurement points at the bone-stem interfaces. Reprinted with permission of Springer from [116].

2.2.2 Mechanical loading protocols

The magnitude and distribution of implant–bone micromotion are highly dependent on the applied loading conditions, and variations in test protocols can lead to markedly different outcomes. Thus, in both experimental studies and subsequent computational models, it is critical to replicate physiologically relevant boundary conditions. Loading protocols summary of experimental micromotion measurement at the surface of the cementless femoral prosthesis is summarised in Table 2.1.

Kassi et al. [105] implanted identical cementless stems into 18 composite femora and applied cyclic loads using a servo-hydraulic testing system to replicate stair climbing and walking. Six LVDTs recorded the elastic and plastic components of micromotion, and an optical encoder measured axial displacement. Their results showed that stair climbing produced significantly greater micromotion (plastic: 177 ± 68 μm; elastic: 50 ± 5 μm) compared with walking (plastic: 36 ± 19 μm; elastic: 17 ± 6 μm), underscoring the importance of simulating physiological loading conditions to capture realistic implant behaviour.

Other studies have confirmed the strong influence of loading protocols. Abdul-Kadir [99] applied a vertical cyclic load of 2000 N along the femoral axis and reported micromotion amplitudes of 18 ± 2 μm proximally and 19 ± 5 μm distally. Pettersen et al. [107] and Osbyhaug et al. [98] employed similar setups under stair-climbing loads (600 N axial load combined with torsional moments of 13.5 Nm and 15 Nm, respectively). Ostbyhaug et al. [98] reported maximum proximal micromotion of 27 μm and distal micromotion of 182 μm, whereas Pettersen et al. [107] reported 28.52 μm proximally and only 60.52 μm distally. These discrepancies highlight the challenges of comparing published results on micromotion measurements of implant bone surfaces due to multiple factors such as different test setups, loading conditions and specimens used.

In addition, Cristofolini et al. [112] combined LVDTs with strain gauges mounted on the greater trochanter and, under a pure torsional load of 15–25 Nm (stair-climbing equivalent), measured axial displacement of 10 ± 2 μm. Notably, this was among the few experimental protocols conducted without an additional superimposed axial compression.

2.2.3 Implant-related micromotion

The type of prosthesis has been recognised as a crucial determinant of implant micromotion, which in turn plays a central role in the development of aseptic loosening. To address this, numerous in vitro investigations

have been conducted to compare the micromotion of different implant designs under controlled loading conditions. Several studies have compared cementless and cemented femoral stems [117], [118], [119], [120], [121], showing that cementless implants exhibit significantly less subsidence and rotational instability than cemented designs. In one of the earliest investigations, three straight cemented stems and one curved cementless stem were tested in cadaveric femora under combined dynamic axial and torsional loading. Micromotions at the prosthesis/bone interfaces were found to be smallest for the curved and highest for one of the straight cemented prostheses [120]. Future implant developments should therefore focus on enhancing the *primary stability* of cementless stems. Several experimental and comparative studies have evaluated variations such as anatomical versus straight stems, and short versus standard-length stems, providing biomechanical evidence on how design features influence the magnitude and distribution of bone–implant micromotion.

The Zweymüller concept, characterised by a straight tapered geometry with a rectangular cross-section and a four-point fixation principle, achieves primary stability through a press-fit in both the proximal metaphysis and the diaphyseal canal, providing strong resistance against axial and rotational forces. Bieger et al. [97] compared the traditional CBH stem with the modified bone-preserving CBH (CBH bp) under dynamic loading (100–1600 N for 40,000 cycles). Micromotions ranged from 6.6–45.6 μm for the CBH and 9.9–67.1 μm for the CBH bp, with the highest values consistently at the femoral neck region. Although both designs remained well below the critical 150 μm threshold, the CBH bp showed slightly higher micromotions proximally, suggesting a potential tendency toward reduced rotational stability relative to the conventional CBH. In 2002, a customised femoral stem was compared with the conventional Alloclassic stem (Freiburg, Germany) and reported that the customised design provided comparable overall initial stability, with increased stability in the proximal region due to significantly reduced micromotion [103]. The proximal metaphyseal portion of the customised stem was enlarged to achieve a closer fit within the proximal femoral canal, resulting in reduced rotational motion compared with the Alloclassic SL stem. However, unlike in the proximal region, the customised implant exhibited greater mediolateral translation distally, which is consistent with the biomechanical concept of distal anchorage in the Alloclassic SL design.

Anatomic cementless stems are designed to mimic the natural curvature of the femoral canal and achieve primary stability predominantly through proximal metaphyseal fixation, thereby promoting physiological load transfer while minimising distal fixation. The CLS Spotorno stem is one of the most widely used anatomic

cementless designs. Fottner et al. [101] investigated the influence of offset in the CLS Spotorno stem by comparing three neck-shaft angles (125°, 135°, and 145°) using three-dimensional micromotion measurements. Across all offset variants, micromotions were most pronounced at the distal stem tip, where values consistently exceeded the 150 µm threshold required for osseous integration, indicating that distal fixation is unlikely. By contrast, proximal measurement points exhibited considerably lower micromotions (68–113 µm), remaining below the 150 µm limit and thus within the range considered favourable for bone ingrowth. These results align with the design rationale of the CLS Spotorno, which aims to achieve proximal load transfer while minimising distal fixation. More recently, Schmidutz et al. [115] assessed three different CLS stem sizes implanted into correspondingly sized composite femora. Their results indicated a consistent tendency for the stems to migrate into a varus position under dynamic loading, regardless of stem size. Significant differences among stem sizes were observed only at the mid-medial measurement point (point 3), while size-related adjustments of the applied load did not result in marked differences in overall micromotion. Apart from the distal tip, where the highest values were recorded, micromotion at proximal and mid-level locations remained clearly below 100 µm for all stem sizes.

In addition, other anatomic cementless stems have also been evaluated in comparative studies against customised designs. One investigation compared the ABG (Anatomic Benoist–Girard) stem with the Unique® stem, a shorter custom-made implant (on average 19 mm shorter, range 11–27 mm) by Ostbyhaug et al. [98]. The ABG stem features an anatomically contoured proximal geometry with a macro-relief surface, and its proximal third is fully coated with a thick hydroxyapatite (HA) layer to promote osseointegration. Under stair-climbing conditions, micromotion at the proximal lateral surface was significantly greater for the ABG stem (24 µm) compared with the Unique® stem (14 µm). Within the HA-coated region, maximum micromotions were 28 µm for the ABG and 77 µm for the Unique® stem, although direct statistical comparison at the mid-level was not feasible due to differences in the HA-coated region length.

To preserve femoral bone stock, short-stem and stemless hip prostheses have been developed. However, purely metaphyseal designs without fixation at the greater trochanter are now rarely used, primarily due to complications such as chronic trochanteric pain. Fottner et al. [100] compared short-stem femoral prostheses and showed that under-sizing of cementless stems increases the risk of aseptic loosening and early subsidence. Mayo prosthesis (Zimmer, USA) and Metha prosthesis (Aesculap, Germany) were analysed. Metha prostheses

with different taper adapters (130° vs. 140°) demonstrated notable differences: the 130° variant produced significantly higher proximal micromotions, explained by the smaller neck-shaft angle that increases the load application angle from 24° to 34°. For the Mayo prosthesis, micromotions were consistently low (45.2–54.1 μm) at most sites, suggesting stable anchorage, but doubled at the critical medial proximal site (105 μm), indicating a potential loosening risk. This study highlights that design parameters of short-stem prostheses, such as neck-shaft angle and adapter selection, strongly affect proximal bone–implant micromotion.

Although in vitro mechanical bench tests have provided significant insights into the measurement of bone–implant interface micromotion and the assessment of *primary stability*, their relevance for understanding long-term implant stability remains debated. The use of synthetic or cadaveric femora entails inherent limitations: synthetic bones cannot reproduce the biological behaviour of living bone, while cadaveric specimens degrade over time. Furthermore, while Sawbones facilitate standardised mechanical testing, it eliminates patient-specific variability, thereby neglecting the influence of bone quality and geometry variation. In vitro studies are usually performed based on ideal implantation and tend to focus on the dependence of micromotion and stress distribution on prosthesis design rather than on surgical uncertainty.

For these reasons, computational modelling has been increasingly adopted to complement experimental approaches. By integrating in vivo and in vitro data, finite element (FE) simulations can be validated against experimental measurements, thereby improving confidence in their predictions. Moreover, subject-specific FE models allow the evaluation of implant designs within a wider spectrum of femoral geometries, enabling systematic isolation of individual parameters and investigation of their impact on both primary and long-term stability.

2.3 In vivo studies for osseointegration

The risk of aseptic loosening in cementless hip stems can be reduced by improving osseointegration with osteo-inductive coatings that favour long-term implant stability. Osseointegration is usually evaluated in in vivo studies, which, however, do not reproduce the mechanically driven adaptation process. A large body of animal studies has evaluated bone ingrowth or bone remodelling across different geometries, materials and surface roughness levels, porous architectures, and surface coatings, in dogs [122], [123], sheep [124], [125] or rabbits

[126], [127], [128]. These translational studies are considered important preclinical steps before new implant designs are used in the clinic. The porous surface and hydroxyapatite coating (HA) are believed to promote osseointegration.

An ovine study compared the bone-healing response to a titanium alloy implant with 5 different surface structures [125], including grit-blasted (GB); grit-blasted plus a 50-µm hydroxyapatite coating (GBHA); Porocoat (PC), a porous structure; Porocoat with HA coating (PCHA); and a smooth surface (S) as control.. All were assessed at 4-, 8-, and 12-weeks using push-out testing, histology, and backscattered scanning electron microscopy (SEM). Push-out testing demonstrated that PC and PCHA surfaces provided significantly greater mechanical fixation than all other implant types at every time point. HA coating on grit-blasted surfaces significantly improved fixation at 8 and 12 weeks. Similar results were also found in another ovine study [124], in which titanium plasma-sprayed and HA-coated pins were implanted into cortical and cancellous bone and evaluated after 4 and 12 weeks. Histological analyses were performed to examine bone ingrowth, interface reactions, and morphological parameters. Push-out testing in cortical sites demonstrated that titanium plasma-sprayed surfaces, which provide a porous structure, outperformed HA-coated surfaces. Nevertheless, both surface types promoted new bone ingrowth and remodelling in both cortical and cancellous regions.

Specifically, the biologic attachment characteristics of HA-coated porous titanium and uncoated porous titanium implants were investigated in a canine study [123]. The implants were transcortical placed. The interfacial shear strength of porous structures increased over time, indicating progressive improvement in bone fixation. However, the addition of HA did not further enhance the mechanical fixation of porous titanium. The main difference was observed at the interface: in HA-coated samples, the coating directly supported bone mineralization, and a thin continuous bone layer was consistently detected on the HA surface. In contrast, in uncoated samples, a very thin fibrous tissue layer was present between the titanium particles and the ingrown bone, without extensive direct bone apposition. These findings suggest that HA coating promotes a bioactive biological bond, even though porous structures already provide superior mechanical fixation.

By distinguishing between dense HA coatings, which are compact layers without interconnected porosity, and porous HA coatings, in which the coating itself is engineered with a porous architecture, a study in both rabbit and canine models demonstrated marked differences in biological response [127]. The porous HA coatings, with approximately 48% porosity and an average pore size of <100 µm, significantly enhanced early bone

ingrowth and fixation at one-month post-implantation, achieving up to a 120% improvement compared with dense HA coatings. Mechanistically, dense HA layers primarily support surface on-growth, whereas porous HA coatings allow bone ingrowth within the coating structure.

Other coating strategies beyond HA have also been investigated. A recent rabbit study examined the effects of HA and type I collagen coatings on Ti-6Al-4V and Co-Cr-Mo implants [126]. Sixty-four cylindrical implants were inserted into the femoral condyles and evaluated at 4 and 12 weeks. The results demonstrated that HA coatings accelerated the bone–implant contact process, whereas collagen coatings did not significantly improve osseointegration compared with uncoated controls.

In summary, animal experiments remain indispensable for studying osseointegration, despite their limitations. The main question is how efficiently these animal experiments translate to the case of human bone. A major question is how translatable animal experiments used to assess the implant designs, materials, or porous coatings are in the human femur [129]. For instance, rabbit cortical bone exhibits a turnover rate three to four times faster than in humans, particularly in young animals. While bone density and flexural strength are generally comparable to human bone, differences in bone mass, vascularisation, and mechanical loading environments impose substantial limitations when drawing clinical inferences. Moreover, most animal studies rely on transcortical nail placement, which contrasts with clinical cases where porous-coated implants predominantly interact with cancellous bone. Human studies have demonstrated a markedly slower ingrowth of cancellous bone into porous-coated titanium implants [130], suggesting that fixation outcomes observed in cortical models may not directly translate to clinical stability. This indicates that the capacity of bone ingrowth of cancellous bone has often been overestimated. To address these limitations, computational models (*in silico trials*) offer an alternative framework by incorporating comprehensive biomechanical factors—including bone anatomy and quality, implant geometry and orientation, interface treatments, and mechanical loading. Such models hold promise for bridging the translational gap between preclinical experiments and applications. The methodological strategies for modelling osteointegration (secondary stability) to predict aseptic loosening failure mode will be reviewed in Chapter 3.

2.4 Validated patient-specific FE model

Excessive micromotion at the bone–implant interface is known to compromise *primary stability* and eventually lead to aseptic loosening. Finite element (FE) models have been developed and applied to simulate the contact behaviour of femoral stems with greater accuracy. A major challenge lies in reliably capturing the progressive non-linear contact behaviour at the bone–implant interface. To validate subject-specific FE models for predicting the relative micromotion between cementless femoral stems and bone, several studies have compared FE predictions with experimental measurements obtained from the same femur (Table 2.1). These investigations proved the value of FE analysis in evaluating implant design outcomes in THA and highlighted specific contact modelling techniques as well as key influencing factors that should be considered in predicting micromotion to support patient-specific preoperative planning: (1) Patient variabilities; (2) Implant selection; (3) Surgical uncertainties; (4) Postoperative lifestyles.

Viceconti et al. [57], [102] evaluated a range of FE contact modelling techniques for predicting the primary stability of cementless stems, including frictionless, frictional, and press-fit frictional contacts, as well as node-to-node, node-to-surface, and surface-to-surface contact formulations. Comparison of FE predictions with in vitro micromotion measurements revealed that the *surface-to-surface, large-sliding, frictional contact* approach achieved the highest accuracy, with a minimum root-mean-square (RMS) error of 10 μm, whereas all other formulations exceeded 20 μm error. Similarly, Pettersen et al. [107] validated subject-specific FE models by comparing predicted micromotion against repeated experimental measurements under combined axial and torsional loading. These models were able to accurately reproduce the experimental results, with an RMS error of 12 μm and a peak error of 21 μm. Another similar study by Abdul-Kadir et al. [99] investigated the effect of different interference fit values (0–50 μm) on micromotion and validated the FE predictions against bench test results, reporting an average error of approximately 18–19 μm.

To provide a comprehensive *primary stability* prediction by computational models, Viceconti et al. [57] firstly developed a parametric FE analysis on an anatomically normal human femur implanted with a cementless anatomical stem (AncaFit, Cremascoli, Italy). Key factors were systematically varied, including the mechanical properties of bone quality, bone–implant interface gaps, patient body weight, and femoral size. The stem model was scaled to ensure correct sizing and alignment within the medullary canal across different femoral geometries. For each parameter, clinically relevant statistical distributions were defined, and their

combined effects were explored through a Monte Carlo approach involving more than 1000 simulated cases. The authors further emphasised that an adequate representation of geometrical variability requires consideration of surgical choices, such as implanting larger or smaller stem sizes within the same femur, and true inter-subject variability cannot be reproduced by simple uniform scaling.

The accuracy of virtual preoperative planning generating FE models was also suspected at the beginning. Reggiani et al. [113], [114] developed subject-specific FE models to predict the *primary stability* of cementless femoral stems to compare the preoperative plan-based FE model and the real postoperative FE model. These models were validated against in vitro experimental measurements of bone–implant interface micromotion under an applied internal torque of 11.4 Nm, showing good accuracy with an average root-mean-square (RMS) error of 7% across the applied load range. In their subsequent work, a sensitivity analysis was performed on the effect of stem position and orientation using an anatomical cementless femoral stem implanted into a cadaveric femur. CT scans performed before and after implantation were used to generate two FE models, referred to as PLANNED and ACHIEVED. Under bench test conditions, the experimental setup measured a micromotion of 171 μm, while the PLANNED and ACHIEVED FE models predicted 150 μm and 170 μm, respectively. The reported deviations corresponded to RMS errors of 12–13 μm and peak errors of 21–26 μm, indicating high agreement between FE predictions and experimental values. Importantly, the two FE models also provided consistent predictions of stress and micromotion, demonstrating that preoperative planning models can be reliably used to assess *primary stability*, even when minor differences exist between the planned and the achieved stem pose. This finding supports the feasibility of using virtual surgical planning for more specific preoperative analyses.

The variability of *primary stability* of cementless stems across different daily activities was investigated by Pancanti et al. [131]. Nine daily activities were simulated based on in vivo hip joint loading data reported by Bergmann (2001), with stair climbing producing the greatest micromotion. In all simulations, peak micromotion was consistently predicted at the distal–posterior region of the stem, reflecting the design rationale of anatomical stems, where stable fixation is expected to occur primarily in the proximal rather than the distal region. A factorial ANOVA performed on the predicted peak micromotions revealed that inter-subject variability was significantly greater than inter-task variability. However, the study did not account for

subject-specific differences in bone quality, stem fit, or the extent of stem–cortical contact, factors that would likely exacerbate inter-subject variability.

In a more recent study, building on these methodological and validation studies, Al-Dirini et al.[132] proposed an automated surgical planning framework of cementless femoral stems to predict the *primary stability*, including both patient and surgical variabilities. By segmenting the cortical bone boundaries, the algorithm first scanned the endocortical canal to identify the stem size and reference position that achieved the best anatomical fit without breaching the cortical wall. This automatically selected configuration was then used as the baseline for each femur, upon which surgical variations—implemented as controlled rotations and translations of the implant—were systematically introduced and compared. It highlighted that the *primary stability* of cementless femoral stems is highly dependent on both patient factors (such as bone mineral density and caput–collum–diaphyseal angle) and surgical variation (notably anteversion and medial–lateral offset). Including surgical variability brought FE predictions into closer alignment with clinical registry outcomes, highlighting the value of virtual trials for implant evaluation and selection.

It should be noted that performing computational modelling and simulation for medical devices can decrease the number of physical tests necessary for product development. Assuring that the computational model has been formed using sound procedures is key and is achieved through the processes of verification, validation and uncertainty quantification (VVUQ) [133]. Verification is performed to determine if the computational model fits the mathematical description. Validation is implemented to determine if the model accurately represents the real-world application. Uncertainty quantification is conducted to determine how variations in the numerical and physical parameters affect simulation outcomes.

Chapter 3

A Literature Review: Finite Element Models to Predict the Risk of Aseptic Loosening in Cementless Femoral Stems

Reproduced from the published manuscript:

Sun, X.; Curreli, C.; Viceconti, M. Finite Element Models to Predict the Risk of Aseptic Loosening in Cementless Femoral Stems: A Literature Review. Appl. Sci. 2024, 14, 3200. https://doi.org/10.3390/app14083200

Abstract

As the most common failure mode in total hip arthroplasty (THA), aseptic loosening severely compromises the longevity of prosthetic implants. Patients undergoing aseptic loosening after total hip arthroplasty may present with a wide spectrum of clinical manifestations. In mild cases, the condition can remain asymptomatic, whereas in severe cases it is often characterized by progressive impairment of joint function accompanied by localized pain. Clinical evaluation begins with a detailed medical history and physical examination. Typical symptoms include gait pattern abnormalities, painful restriction of the range of motion, limitations in walking ability, and limb length discrepancy as the result of femoral subsidence. Pain is typically exacerbated in weight bearing conditions due to increased joint loading. Notably, pain associated with loosening of the femoral stem is generally more pronounced and disabling than that arising from the acetabular component [53]. In the worst cases, complex and invasive revision surgery may be required, which imposes substantial clinical and economic burdens. Because the success rate of revision procedures declines significantly with each subsequent revisions over time [54]. These adverse outcomes have drawn substantial attention from both clinicians and engineers, motivating a spectrum of research efforts dedicated to understanding and preventing aseptic loosening.

The mechanism of aseptic loosening of THA prostheses is complex and not fully understood. It occurs as a result of inadequate initial fixation, mechanical fixation failure over time, or biological fixation failure over time. In most cases, the etiologic is combinatorial three factors. Currently, the most widely accepted causes are periprosthetic bone dissolution induced by wear debris from the prosthesis and large relative micromotion.

Existing studies cover multiple complementary perspectives to assess and predict the occurrence of aseptic loosening, including large-scale clinical retrospective analyses aimed at identifying risk factors, advanced imaging approaches for early diagnosis and monitoring of implant instability, in vivo and in vitro experiments that investigate the biomechanical and biological mechanisms at the bone–implant interface, as well as animal studies that provide translational insights.

This chapter will provide a comprehensive state-of-the-art review of these approaches, outlining current advances in the assessment of aseptic loosening in cementless hip implants. The following chapter will then address patient-specific computational models of osseointegration, which represent a rapidly evolving

methodology for predicting long-term implant stability and assessing the risk of aseptic loosening in individual patients.

3.1 Introduction

Since the 1960s, total hip arthroplasty (THA) has proven to be successful in alleviating hip pain, enhancing mobility and quality of life, and enabling patients to resume regular activities. Over three million primary THAs are performed annually in Europe [35], [134], and different studies suggest that a further increase in demand is anticipated over the next 20 years [44], [45]. From an engineering point of view, THAs can be mainly classified as cemented or cementless, depending on the implant fixation modality. Cementless fixation, which relies on press fit and osseous integration, has gained popularity over the past decade, both for cups and stems [135], [136]. According to the latest report on primary THAs from the Register of the Orthopaedic Prosthetic Implants register, between 2017 and 2019, cementless cups and stems accounted for 99% and 96.7% of all operations, respectively, in Italy [137]. The latest National Joint Registry annual report also indicates a total number of primary uncemented hip replacements higher than that of cemented implants [138].

Despite being one of the most effective and commonly performed orthopaedic procedures, with a 10-year survival rate of over 90% shown in cementless implants [135], the number of implant revisions is continuously rising, mainly due to the growing number of primary surgeries. Given the significant medical and economic burden associated with the revision surgery, the significance of paying closer attention to THA failure and lowering the risk is self-evident. The THA failure patterns most frequently observed include aseptic loosening (AL), infection, periprosthetic fracture, and instability. Aseptic loosening remains the leading cause of failure, as evident in most hip replacement registers. The reported values for the AL failure incidence range from 40% to 70% of all implants failure [139], [140], [141].

Aseptic loosening is described as the failure of the bone–implant fixation in the absence of infection [55]. Although AL can occur due to inadequate initial fixation (e.g., small-to-fit), it is primarily associated with mid- and long-term instability. While substantial evidence has been observed regarding the mechanics of AL, it is difficult to attribute it to a single cause. Aseptic loosening is often accompanied by periprosthetic osteolysis, which refers to bone resorption around the implant as well as an inflammatory cellular response within the joint. Additionally, excessive micromotion at the bone–implant interface or the abrasion of polyethene

particles from wear can also contribute to AL [55]. More practically speaking, AL is caused by various preoperative, intraoperative, and post-operative factors, including patients' bone quality, implant properties, surgical technique, and lifestyles. Among them, the implant designs play a crucial role in the procedure's success [142]. Clinical studies conducted long-term follow-up assessments to track the survival rate of THAs with various implant types, with some highlighting the AL rate of cementless femoral implants. In many cementless stem designs, a 10-year survivorship rate of over 96% has been observed (e.g., ABG I, Osteonics Cementless, R-B Interlok, Zweymuller-Alloclassic, Freeman Cementless) [143]. At 4.5 years, the estimated probability of revision for AL was 18.6% for the Bio-Fit stem (cobalt-chromium; straight stem) and 0.5% for the Corail stem (Titanium; straight stem) [51]. Another 5-year follow-up study conducted on 517 cementless THAs found an unusually high number of AL failure cases after using a modified stem with a shorter and shoulder-less double-taper [49]. The revision rate for the smaller Corail stem was four times higher than that for larger femoral diameters [50]. Different implant designs show a considerably different incidence of AL, which confirms that implant design is a major determinant.

Therefore, studying the effect of various femoral implant types on failure risk is crucial for improving patient safety, reducing costs, and improving long-term outcomes. Conventional methods for predicting the AL failure risk and assessing the safety of the implant devices preoperatively include in vitro experiments, animal experiments, and clinical trials. However, each approach has its limitations. One notable weakness of in vitro experiments is their inability to fully replicate the conditions of cells or tissues in a living organism [144]. Animal experiments can maintain biological conditions, but they may not be equivalent to clinical conditions in human patients [145]. Clinical trials are time consuming, costly, and limited in this long-term failure risk investigation. One promising alternative to traditional methods is represented by the use of computer modelling and simulation. In particular, Finite Element (FE) modelling, has been demonstrated to be a powerful numerical tool that allows for generating information supporting the device's safety and/or efficacy. It holds promise for assessing whether subtle modifications in orthopaedic devices can enhance existing designs while accounting for patient and surgical variability [146], [147], [148]. A virtual cohort of simulated patients can be used to optimise implant design, including material selection, geometry, and surface features (In Silico Trials) [149], [150]. Also, with patient-specific models, surgeons can create a virtual replica of a patient's anatomy (Digital Twins), personalise the planning, and optimise the surgical outcome [151].

A large body of literature has used FE modelling to investigate the biomechanical interaction between bone and cementless femoral implants in the context of AL failure. This literature covers a broad range of topics and can be categorised into subsets based on the various aspects related to AL that have been specifically analysed. Some researchers simulated the complex interactions between the implant and surrounding bone by quantifying parameters such as stress distributions, micromotion, osseo-integrated area, and bone remodelling [152], [153], [154], [155], [156], [157], [158]. Most of the studies focused on mitigating the risks of AL from various perspectives. For instance, some have evaluated the mechanical performance of stems with different parameters, such as geometric features and materials [153], [154], [156], [157], [158], [159], [160], [161], [162], [163], [164], [165]. Others have examined the effect of bone quality [166], [167], surgical variability, and patients lifestyles [155], [158], [160], [167], [168] on the risk of failure. While some articles have attempted to review the literature on numerical simulation of orthopaedic devices [147], [169], including in some cases analyses on post-operative bone growth and long-term bone adaptation [170], to the best of the authors' knowledge, none provide a comprehensive overview of the use of FE simulations to specifically investigate AL failure risk in cementless femoral stems.

The aim of this paper is to address this gap by providing a comprehensive overview of the main modelling procedures for predicting AL risk in cementless femoral stems due to a lack of long-term stability. The review will assess papers based on several criteria, including bone and implant geometry modelling, loading patterns considered, contact models, and output quantities analysed. For most of these criteria, the main limitations and effects of the different modelling assumptions on the simulation results will also be discussed.

3.2 Studies Selection

By conducting a comprehensive search of the PubMed databases, an initial list of relevant publications was generated using the key terms: ((hip replacement) OR (hip arthroplasty) OR (hip implant)) AND ((Finite Element) OR (simulation) OR (modelling)) AND ((aseptic loosening) OR (bone remodelling) OR (bone ingrowth) OR (osseointegration)). One important point to note is that when conducting a literature search on the prediction of AL failure modes using FE modelling, some researchers use terms such as 'bone ingrowth', 'bone remodelling', and 'osseointegration' instead of directly referring to AL or long-term stability failure of the implant. This variation in indirect terminology can be attributed to the multifactorial nature of AL. It is

therefore advisable to consider these indirect searches to ensure a more comprehensive coverage of the literature.

Potentially eligible articles were initially screened by title and abstract. If they did not match any of the following categories, they were excluded:

- hip joint replacement;
- Finite Element models;
- failure modes related to aseptic loosening.

After a thorough reading of the full manuscripts, studies were further excluded if they met any of the following criteria:

- osseointegration at the bone implant interface was not modelled;
- the implants were cemented;
- only lack of primary stability was simulated.

To clarify the last exclusion criterion, it is important to note that there is a significant body of literature that focuses on the mechanical behaviour of primary stability, which is an important risk factor for the AL of cementless hip implants (discussed in Chapter 2). And evidence was found that early peri-implant bone healing immediately after implantation and the consequent mechanical remodelling at the bone–implant interface are essential for secondary implant stability [171], [172]. Hence, if the study only investigated primary stability without any consideration of long-term adaptative biological evolution, it was excluded. It should also be noted that conference proceedings were excluded from the analysis, and only research journal articles published in the last three decades (1994-today) were considered. Of the 946 papers that our initial search identified, at the end of this selection process, by removing the overlap and based on the criteria above, 22 papers were considered for this review. This final selection also includes six additional sources that were identified after examining the bibliography of all relevant articles. The flowchart of article selection is depicted in Fig3.1. The studies will be detailed in the following sections according to suitable model assumptions for the following aspects:

- characteristics of bone and implant modelling (e.g., geometry, surgical pose, material properties, and meshing);

- boundary conditions;
- bone–implant interface contact;
- quantities of interest used to predict the failure mode.

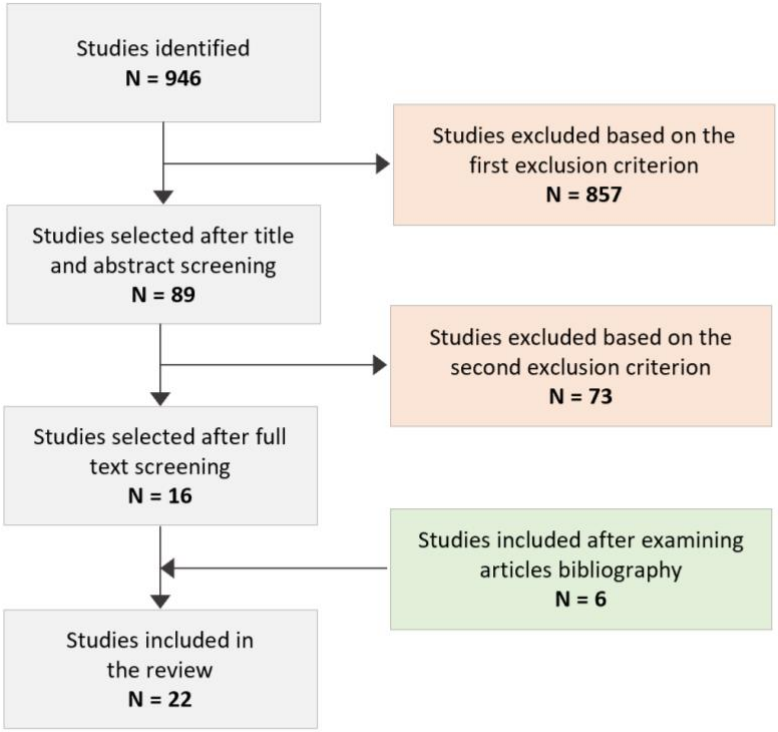

Figure 3.1. Flowchart of article selection.

3.3 Search Results

3.3.1. Bone and Implant Features

3.3.1.1. Geometry

Bone

Most 3D FE models have been developed by directly segmenting the bone geometry from computed tomography (CT) scan datasets of the patients and reducing the length of the original femur by resecting the distal part of the bone to reduce the computational cost (Table 3.1). Medical image processing software such as MIMICS (Materialise, Leuven, Belgium) was typically used in most of the selected works to process CT scan data and distinguish bone from soft tissue using CT number threshold values [154], [160]. In some cases, the three dimensional geometry of a composite femur was used as a standard reference for the FE model (Table

3.1) [152], [155], [156], [157], [158]. Instead of the intact bone–implant model, few studies solely mimic the local adjacent region of bone–implant interfaces based on a cubic 3D CAD model [162], [165], [173] or a plane 2D model [174]. In addition, simplified cylindrical 3D models were reconstructed in [159], [166].

Implant

As shown in Table 3.1, only a few studies used simplified cylindrical or truncated cone shapes to model the femoral stem implant [159], [175], while cubic and planar geometries were considered only for local models that include the adjacent regions of the bone–implant interface [162], [165], [173]. The majority of FE models of the implant were derived from commercial stem designs. Implants with different outline structures and surface morphologies have been tested as comparative characteristics to investigate whether implant geometries affect stability [153], [154], [156], [158], [160], [161], [162], [165], [176]. For example, S. Chanda et al. investigated osseointegration and bone remodelling performance using two fully coated cementless hip stems, one obtained from a generic TriLock (DePuy, USA) design and the other derived from a shape optimisation study [153]. J. Folgado et al. [156] compared two commercial stems: the tapered stem (Trilock by DePuy) and a cylindrical cross-sectioned stem (AML by DePuy). The tapered stem was found to be intrinsically more stable than the cylindrical stem with a similar fit and material. P.K. Puthumanapully et al. [161] focused on the short-stemmed implants and found that more bone formation occurred in the short stem with the lateral flare present compared to when the flare was absent.

Few studies have demonstrated that the implant surface texture might significantly improve bone ingrowth, while non-textured implants might promote fibrous tissue formation [160], [162], [165]. Specifically, three types of stem surface macro-textures were compared in [162], [170]: softer connective tissues and relatively less bone growth were observed at the edges of the grooves/ribs, where high-stress concentration occurs. In addition, some authors simulated the coating surface based on a porous microstructure [159], [174], [177]. F. Tarlochan et al. [159] compared the functionally graded porous with two diameters of homogenous porous microstructures on implant stability. Models with larger pore sizes predicted fewer chances of bone ingrowth, and functionally graded porous surfaces promoted stability and reduced the failure chance.

A few implant shape optimisation studies were also conducted in [153], [158]. R.B. Ruben et al. used a three-dimensional shape optimisation computational tool to obtain a hip stem with improved stability and reduced

stress shielding. Various design variables were considered to define the geometric parameterisation of the stem, starting from the Tri-Lock (DePuy) stem geometry. By minimising three single objective functions targeting tangential displacement on the stem–bone interface, normal contact stress, and stress shielding, they obtained seven optimised stems, which were then used to evaluate long-term performance [158].

3.3.1.2. Bone and Implant Positioning and Initial Fitting

Many authors created the bone–implant assembly using boolean operations and following surgical guidelines to define the relative poses of the two bodies (Table 3.1). Experienced orthopaedic surgeons typically perform the virtual implantations into a resected femur model by translating and rotating the solid geometries within the visualised CT data using specific software (e.g., DCMTK MFC, Robert McNeel & Associates) [154]. The bone–stem orientation was determined according to ISO 7206 in a few studies [160], [163]. Some models have examined the effect of the initial fitting scenarios or initial bone–implant contact area on the bone ingrowth prediction [155], [158], [167], [168]. A perfect initial press fit is what surgeons desire (approximately equal to perfect primary stability) while operating; however, in clinical practice, the stem is often placed with small misalignments while inserted into the bone. To mimic these varying initial contact conditions, M. Tarala et al. generated a gap area of 21% after initially creating a node-to-node surface mesh of bone and implant and adjusting the intramedullary canal contour to match regions with lower local CT values [154]. In another study [167], initial interface contact areas of 100%, 68%, 51%, and 35% with different magnitudes of interfacial gaps ranging from 0 to 1 mm were simulated. Their findings indicated that the ingrowth process accelerated as the contact area between the implant and bone increased. This aligns with another study from M. Viceconti et al. [155], highlighted that a perfect fit configuration led to improved long-term stability through extensive osseointegration. They investigated five initial implant positioning configurations: perfect fit, proximal fit, distal fit, varus fit and valgus fit, which are commonly observed in clinical practice. Two valgus-fitting surgical approaches were also modelled by M. Viceconti et al. in [168]: the implant with proximal lateral and posterior support reached better osseointegration than the configuration that considered the implant with proximal lateral and anterior support. R.B. Ruben et al. [158] clearly stated that totally coated stems are more sensitive to implant misalignments; their results showed that small varus and valgus rotations might lead to reductions in long-term bone ingrowth.

3.3.1.3. Materials

Bone

Most collected studies assumed the bone as a linearly elastic, heterogeneous, locally isotropic material [153], [154], [155], [160], [161], [162], [165], [166], [167], [168], [173], [177], [178]. Some assigned constant Young's modulus values for the cortical and trabecular bones [155], [158], [162], [163], [166], [168], [173]. Bonemat [179] or other in-house software is commonly used for the mechanical property mapping step. Hounsfield Unit values are typically extracted from calibrated CT data to estimate local bone mineral density, and non-linear density-to-elasticity relationships are commonly used to compute the elastic modulus, which is then assigned to mesh elements [154], [161], [167], [177].

Anisotropic material properties assumptions were used for cortical bone by H. Mehboob et al. [163], which provide the Young's modulus and Poisson's ratio in radial, circumferential, and longitudinal directions. F. Tarlochan et al. [159] assigned the anisotropic properties of the cortical bone in longitudinal directions. In addition, few studies [156], [157], [164], [166] considered bone remodelling based on the asymptotic homogenisation method (Table 3.1). Bone material adaptation, bone remodelling algorithms, or soft tissue differentiation properties will be discussed in the part about the bone–implant interface afterwards.

The effect of bone quality on the long-term fixation of the femoral implants was investigated in [166], [167]. Models with superior bone quality indicated larger areas of bone ingrowth, higher rates of ingrowth, and less fibrous tissue. To account for varying bone quality, P. Büchler et al. [166] assigned three different Young's Modulus values for the trabecular bone. In healthy bone, only limited propagation of fibrous tissue was observed in the proximal part of the femur, while poorer bone density showed a thick fibrous membrane around the implant. M. Tarala et al. [167] defined three bone qualities based on the original calcium equivalent distribution. They found that the area of bone ingrowth over the entire interface was higher when better bone quality was considered.

Implant

Most models directly assign commonly used mechanical material properties to the implant, such as Titanium, Cobalt-Chromium, or Stainless steel (Table 3.1). P. Moreo et al. [164] compared the simulation results obtained considering different hip implant materials and found that stem stiffness has an important effect on

bone ingrowth distribution. In particular, they found that flexible stems result in larger areas of poor osseointegration, predominantly observed at the proximal side. J. Folgado et al. [156] found that the CoCr model stem resulted in greater bone resorption compared to titanium stems.

Some modelled the composite construct stem with porous microstructures [154], [163]. M. Tarara et al. developed a composite construct stem based on the VerSys Epoch FullCoat design, which includes the neck, inner, middle, and outer layers with various materials for each part [154]. In total, five types of composite materials were tested. Among them, the 80% porosity tantalum with an inner CoCrMo core showed considerably better performance in terms of bone ingrowth and bone remodelling. H. Mehboob et al. [163] studied solid CoCr alloy, Ti alloy stems, and two porous Ti stems and concluded that high-stiffness stems exhibited increased stress shielding and reduced micromotions compared to stems with lower stiffness.

The surface roughness and coating were modelled in some cases considering different mechanical properties like friction coefficient values [152], [155], [156], [157], [158] and surface material stiffness [164], [178]. P. Moreo et al. [164] studied the impact of polished and rough surface finishes on a titanium stem stability, with different sets of interface mechanical properties. They found that rough stems achieved stability sooner than polished stems, while polished stems showed a higher average bonding degree. Few studies have examined the effect of coated and uncoated stems on long-term implant stability. The uncoated stem exhibited less bone resorption at the proximal femur than coated stems of similar geometry with bone ingrowth [156]. Non-uniform bone ingrowth on the coated surfaces was also observed in [152], [156], [157], [158]. No correlations were found between bone in-growth pattern and coating length for tapered stems [157].

3.3.1.4. Mesh

Tetrahedral and hexahedral meshes are typically used to build the FE models. Element edge lengths ranging from 0.2 to 3.0 mm and from 0.5 to 4 mm, with a relative finer mesh at the bone–implant interface, were considered in [153] and [161], respectively. While the final mesh size varies depending on implant/bone geometry and the investigated outputs, performing a mesh convergence analysis is essential. In [163], a uniform mesh size of 2 mm was adopted after conducting a mesh sensitivity study. In their study, R. Ghosh et al. [160] also conducted a mesh sensitivity analysis, taking into account the convergence of stress and strain. Peak deviatoric strain was also monitored as part of the convergence check as a robust indicator of tissue growth at the bone–implant interface. They determined the optimal mesh size by considering the implanted

femur under peak joint loads during normal gait. X. Liu et al. [174] investigated three different mesh densities with average edge element sizes of 95, 24, and 6 μm, and they found no significant effect of element size on the bone ingrowth fractions.

Table 3.1 Articles included in the review and summary of the main FE modelling characteristics. Highlighted rows refer to those studies that considered a model that only included the adjacent regions of the bone–implant interface.

Research Paper	Geometry		Virtual Implantation and Stem Pose	Materials		Mesh
	Bone	Implant		Bone	Implant	
P.R. Fernandes et al. [157] 2002	Standard human femur [180]	Tri-Lock Prosthesis of DePuy	NA	Cortical bone: E = 20 GPa; Trabecular bone: orthotropic porous material described with the homogenisation method [181], [182]	Titanium (115 GPa)	Hexahedral element
P. Büchler et al. [166] 2003	Three-dimensional hollow cylinder	Truncated cone	Implant placed in the central part of the bone	Cortical bone: E = 15 GPa; Trabecular bone: E = 294, 216, 150 MPa; $\nu = 0.3$	E = 200 GPa; $\nu = 0.3$	8-node hexahedral elements
M. Viceconti et al. [155] 2004 (a)	Standard human femur	AncaFit, Cremascoli Ortho, Italy	Implanted by an expert surgeon	Cortical bone: E = 14.2 GPa; Trabecular bone: E = 69 MPa [183]	Titanium Alloy (E = 107 GPa) [183]	Three separate structured hexahedral meshes for the cortical bone, spongiosa, and implant
M. Viceconti et al. [168] 2004 (b)	CT scans of a composite femur [183]	AncaFit, Cremascoli Ortho, Italy	Implanted by an expert surgeon	Cortical bone: E = 14.2 GPa; Trabecular bone: E = 69 MPa [183]	Titanium Alloy (E = 107 GPa) [183]	Structured mesh with 8-node isoparametric hexahedral elements
P. Moreo et al. [164] 2007	Subject-specific CT-scan dataset (middle-aged female)	Commercial design from Zweymüller (AlloPro, Baar, Switzerland)	NA	Anisotropic and heterogeneous	Stainless Steel (E = 210 GPa); Titanium (E = 84 GPa); Polyacetal (E = 20 GPa)	Hexahedral and wedge linear elements
X. Liu et al. [174] 2008	2D model of a plane	Rigid beads and a rigid bottom surface represent the prosthesis substrate	NA	Mature bone: E = 6 GPa; Immature bone: E = 1 GPa	NA	4-node plane strain elements; three mesh densities
A. Lutz et al. [176] 2009	Subject-specific CT-scan dataset	Mayo prosthesis (Zimmer, Germany)	NA	Linear elastic and isotropic, one phase continuum. Constitutive relationship between E and bone mineral density	NA	Linear tetrahedra; wedge elements for the interface layer; mesh refined gradually surrounds the implant model

S. Checa et al. [173] 2009	Cube (3 × 3 × 1 mm)	Cube (3 × 3 × 1 mm)	NA	Cortical bone: Homogeneous, isotropic, and linear elastic (E = 17 GPa; v = 0.3); Immature bone: E = 1 GPa, ν = 0.3	Homogeneous, isotropic, and linear elastic (E = 100 GPa; ν = 0.3)	Poroelastic elements
J. Folgado et al. [156] 2009	Standard human femur [180]	Tapered-wedge shaped prosthesis (Tri-lock by DePuy; Warsaw, Indiana); Cylindrical cross-sectioned stem (AML by DePuy; Warsaw, Indiana)	Perfect initial fit between the bone and the stem was determined based on post-operative CT scans of two patients following implantation	Trabecular bone: orthotropic, porous, described with the homogenisation method [181], [182] Cortical bone: E = 20 GPa	Titanium (E = 115 GPa); Co–Cr alloy (E = 230 GPa), ν = 0.3	Hexahedral meshes
P.K. Puthumanapully et al. [161] 2011	Subject-specific CT-scan dataset (43-year-old male)	Commercial design from the Proxima (DePuy)	Surgical instructions	Linearly elastic, heterogeneous, and isotropic; E was assigned using BONEMAT	Titanium alloy Titanium alloy 110 GPa, linear, elastic, isotropic material	First-order tetrahedral elements (edge length: range from 0.5 to 4 mm)
M. Tarala et al. [154] 2011	Subject-specific CT-scan dataset (81-year-old male)	Commercial design from VerSys Epoch FullCoat (Zimmer)	Expert surgeon guidance; in-house software within the visualised CT data (DCMTK MFC 10.8)	Isotropic; properties derived from calibrated CT data using an in-house software package	Five configurations with a layered structure varying material property composition	Linear 4-node tetrahedral elements
R.B. Ruben et al. [158] 2012	Standard human femur [180]	3D shape optimisation model based on the Tri-Lock Prosthesis of DePuy	Sensitivity to misalignments is analyzed	Bone marrow (E = 10^{-7} GPa), trabecular (E = 1 GPa) and cortical bone (E = 17 GPa); ν = 0.3	Titanium (E = 115 GPa; ν = 0.3)	Hexahedral meshes
A. Andrade-Campos et al. [152] 2012	Human femur	Commercial design from Tri-lock©/Dual-Lock© of DePuy	Follow surgical instructions; rasps are used to shape the hollow femur to fit the shape of the stem	Trabecular bone: Orthotropic, apparent material described with homogenisation [184] at microscopic level; Cortical bone: E = 20 GPa, ν = 0.3	Titanium (E = 115 GPa)	Linear hexahedral elements; remeshing technique after virtual implantation
A. Lutz et al. [178] 2012	Subject-specific CT-scan dataset	Commercial design from Metha–prosthesis	NA	Isotropic; power law for the constitutive relationship	Titanium (E = 105 GPa)	Linear tetrahedral elements

		(Aesculap, Tuttlingen, Germany)		between Young's modulus and bone mineral density		
M. Tarala et al. [167] 2013	Subject-specific CT-scan dataset (81-year-old male)	VerSys Epoch FullCoat stem (Zimmer, Inc., Warsaw, IN, USA)	The stem was considered settled when a converged subsidence was achieved, meeting the criterion of incremental subsidence values being less than 1% of the total subsidence in subsequent loading periods	Elastic modulus of the bone is computed from the local ash density. Young's Modulus ranged up to 7 GPa, 13.7 GPa, and 22.6 GPa	CoCrMo (E = 240 GPa), PEEK (E = 3.4 GPa) and Fiber mesh (E = 6.9 GPa), v = 0.3	4-noded tetrahedral elements
F. Tarlochan et al. [159] 2018	Simplified cylindrical 3D models	Cylindrical shape with homogenous and graded porous microstructure	Interface fit introduced using a prosthesis larger than the bone inner	Cortical bone: anisotropic [185]; Trabecular bone: isotropic (E = 400 MPa)	Isotropic elastic, Ti Alloy (E = 110 GPa), v = 0.3	Bones and calluses: 8-node poroelastic element; beads and prosthesis: 8-node solid element
S. Chanda et al. [153] 2020	Subject-specific CT-scan dataset (31-year-old)	Tri-Lock (DePuy) design; One optimal stem model based on a shape optimisation study	Expert surgeon guidance	Linearly elastic, heterogeneous, and isotropic; E assigned using BONEMAT v2	Titanium alloy (E = 110 GPa)	10-node tetrahedra, with the interface having a relatively finer mesh (edge length ranges from 0.2 to 3.0 mm)
R. Ghosh et al. [162] 2020	3D macro-textural models of the only bone-implant interface. Three types of macro-textures based on CLS Spotorno, CORAIL and SP-CL stems		NA	Linear, elastic, homogeneous, and isotropic; (E = 500 MPa, v = 0.3)	Linear, elastic, homogeneous and isotropic material (E = 210 GPa, v = 0.3)	8-noded hexahedral elements (edge length: maximum 1 mm)
H. Mehboob et al. [163] 2020	Subject-specific CT-scan dataset	3D printed stem	Stems were implanted in the femur and positioned according to the ISO 7206–8: 1995	Trabecular bone: Isotropic; Cortical bone: anisotropic	CoCr alloy 230 GPa; Ti alloy 110 GPa; 30% porosity Ti 53.8 GPa; 47% porosity Ti 31.5 GPa	Quadratic tetrahedron elements (edge length: 2 mm)
B. Mathai and S. Gupta [177] 2022	Subject-specific CT-scan dataset (31-year-old male); proximal femur	Commercial design from Tri-lock (DePuy);	Expert surgeon guidance; virtually into the resected femur	Linearly elastic, heterogeneous and isotropic;	Titanium alloy (E = 110 GPa, v = 0.3)	10-node tetrahedral elements; (edge length: range from 0.3 to 0.8 mm)

		Microscale model to mimic porous surface coating		E assigned using BONEMAT v2.0		
R. Ghosh et al. [165] 2022	3D macro-textural models of the only bone-implant interface.; two different macro-textured implant surfaces based on CORAIL and SP-CL stems		NA	Linear, elastic, homogeneous, and isotropic; (E = 500 MPa, ν = 0.3)	A high-nitrogen stainless steel alloy M30NW (E = 195 Gpa), ν = 0.3	Linear elastic eight-node hexahedral elements
R. Ghosh et al. [160] 2023	Subject-specific CT-scan dataset (35-year-old female)	Implant model (CORAIL AMT hip stem) with and without macro-textures	Bone–implant assembly created using boolean operation and following surgical protocols. Orientation of the implanted femur based on the ISO 7206–4:2010	Linearly elastic, heterogeneous, and isotropic; E was assigned using BONEMAT	High-nitrogen stainless steel alloy (E = 195 GPa)	10-noded tetra elements finer mesh at the bone-implant interface region

3.3.2. Boundary Conditions

A distinction between macroscale, microscale, and hybrid techniques has been made when detailing the boundary conditions for the selected FE modelling studies (Table 3.2). In particular, macroscale techniques are referred to for those studies where the level of modelling concerns the overall behaviour of the implant–femur structure, while all the works that considered a model that only included the adjacent regions of the bone–implant interface were classified as microscale models (highlighted rows in Table 3.1).

In macroscale models (Fig3.2a), loading conditions are typically determined based on the subject's body weight and applied as hip contact forces and muscular loads (Table 3.2). Muscle loads are distributed over the respective attachment areas [177] or considered rigid plates attached to the stem and femur to avoid stress concentration [163], while the hip contact forces are usually applied as a concentrated load to the centre of the head of the femoral stem [160], [163]. Torsional loading applied to the superior part of the implant was considered in [166]. The femur is usually constrained at the distal part after defining a specific distance *h* below the implant tip (e.g., 45 or 50 mm) (Fig3.2) [160], [177]. The conditions prescribed by Saint-Venant's principle were checked by [176], [178]. Forces and moments extracted from daily activities such as normal walking, stair climbing, standing up, and sitting down are considered in the majority of the selected studies with reference to the work conducted by G. Bergmann et al. [186], M.O Heller et al. [187], [188] and D.R Pedersen et al. [189]. Most of the studies considered static loading scenarios [152], [153], [154], [155], [156], [157], [158], [160], [161], [163], [164], [166], [168] or solved a quasi-static problem by discretizing the load history into sub-steps of static loading [176], [178]. Some authors have proposed adding a less-loaded phase to mimic the resting period or walking with a walking aid after the operation [160], [163], [164], [167]. For example, in [167], an unloading phase was included in each loading cycle with a compressive force of 50 N considered for stability purposes. In the study conducted by [160], [163], both muscle and hip forces were reduced in the first simulation period (e.g., 1–8 iterations) considering 80% of the patient's BW and swing phase of the gait cycle. P. Moreo et al. [164] introduced a one-week period of no loading before simulating 25 weeks of healthy activities, where four different loading cases, including resting, were considered. In addition, the frequency of various activities has been taken into account in a few studies [161], [164].

The microscale models are usually solved under loading conditions, in terms of both loads and displacements, applied to the implant part while constraining the bone [162], [165], [173]. In [174], the fixed part was the

bottom surface of the implant. Shear load or tangential displacements were typically used to impose relative motion between the bone and the implant, while compressive force or normal displacement were applied to simulate gap distance and press-fit conditions at the bone–implant interface [162], [165].

A hybrid approach was adopted in [163], [177], where loading conditions applied to the microscale model were obtained by first solving the macroscale analysis (Table 3.2).

Some authors investigated how different loading conditions could influence the simulation results in terms of osseointegration [160], [164], [165], [178]. R. Ghosh et al. [160] examined the influence of two typical loading scenarios (i.e., normal walking and stair climbing) on the growth of the connective tissue phenotypes (i.e., mesenchymal stem cells, fibrous tissue, cartilage, and bone) around the stem. The results demonstrated a higher occurrence of fibrous tissue during stair climbing in comparison to normal walking. This suggests an increased risk of early AL during stair climbing, potentially attributed to elevated torsional moments at the bone–implant interface. With a higher value of normal displacement at the local interface, an increasing formation of fibrous tissue near the implant surface was found, which might lead to a higher AL risk [170]. R. Ghosh et al. [170] did a full factorial analysis to simulate all the possible combinations of tangential and normal micromotions while assessing their influence on bone growth. They found that both shear and normal micromotion played an important role in the type and amount of tissue phenotype formed at the interface. P. Moreo et al. [164] investigated the influence of patient resting schemes on osseointegration. Three post-surgical scenarios were tested, varying the duration of the initial resting time and load values representing the resting phase included in the four post-operation activities. The results obtained after simulating 25 weeks post-surgery showed that models with longer initial resting times achieved bone ingrowth stability sooner, while shorter initial resting times showed a lower average bonding degree. A. Lutz et al. [178] studied the effect of discretization of the six load cases on the simulation results. After observing similar patterns in terms of stimulus for osseointegration and corresponding micromotion at the interface obtained considering 180, 90, 45, 30, 15, 10, and 5 load steps, they decided to use only 5 load steps for the simulation in order to reduce the computation cost.

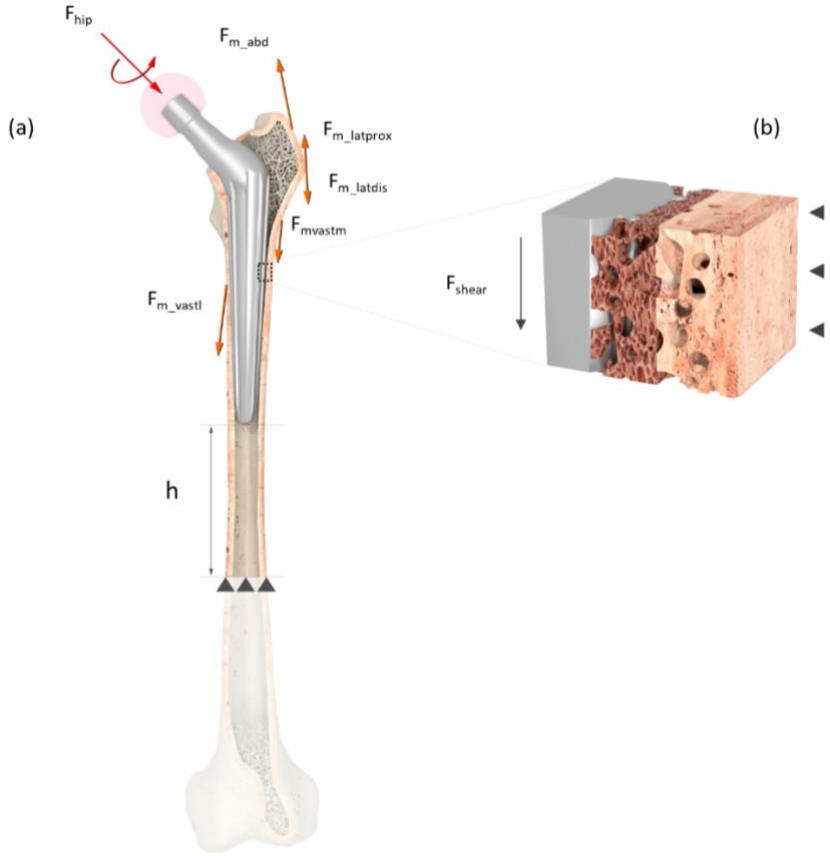

Figure 3.2. (a) Commonly used loading and constrained conditions for the macroscale models. For simplicity, only the main forces involved in normal walking and stair climbing are shown: F_{hip} (hip joint force), F_{m_abd} (abductor), F_{m_vastm} (vastus medialis), F_{m_vastl} (vastus lateralis), $F_{m\_latprox}$ (tensor fascia lata—proximal part), and F_{m_latdis} (tensor fascia lata—distal part). (b) Boundary conditions typically defined for microscale models include shear loads or tangential displacements (F_{shear}) at the implant part and constraints at the bone surface

Table 3.2. Loading conditions defined in the FE modelling studies considering macroscale, microscale, and hybrid techniques.

Macroscale Models		Microscale Models	
Research Paper	**Loading Conditions**	**Research Paper**	**Loading Conditions**
P.R. Fernandes et al. [157] J. Folgado et al. [156] R.B. Ruben et al. [158] A. Andrade-Campos et al. [152]	Peak joint forces during the stand phase of normal walking and the maximal joint load during stair climbing [190]. Muscle force considering one attachment point and hip contact forces.	X. Liu et al. [174]	Combination of 5 MPa shear and 5 MPa compressive stress, corresponding to the maximum load along the length of the stem [191] was applied to the bone part of the model. Beads and the bottom surface of the implant were fixed.
P. Büchler et al. [166]	Torsional loading applied to the superior part of the implant as described in [192].	S. Checa et al. [173]	Both force- and displacement-controlled conditions were used. The bone surface is constrained. Equal pore pressure and nodal displacements on the upper and lower surfaces to approximate a repeating unit of a long implant. Under force controlled conditions, shear load, applied to the implant surface, is defined based on specific initial relative displacements (117–233 μm) between the bone and the implant resulting [193], [194].
M. Viceconti et al. [155]	Peak joint load during stair climbing [186] applied as hip contact force.		
M. Viceconti et al. [168]	Model details are reported in [183], where stair-climbing activities are simulated considering a torsional force applied to the implant neck.		
P. Moreo et al. [164]	Four different post-operation activities, including resting, were considered for the load cases. Abductor muscle and hip contact forces [186], [188] were applied as two static loads.	R. Ghosh et al. [162]	Tangential displacement of 20 μm applied to the bottom surface of the implant based on [195]. Normal displacement of 20 μm is also applied to simulate press-fit conditions. Top surface of the bone is fixed.
A. Lutz et al. [176] A. Lutz et al. [178]	Different daily activities are considered with load values extracted from the OrthoLoad database. Load history is applied at the hip joint by discretizing the time series into static steps. Nine muscle forces are applied as static equivalent loads [196].	R. Ghosh et al. [165]	Shear displacement (20 μm) and normal displacements (5, 10, 20, 40 μm) applied at the bottom surface of the implant to simulate micromotions at the interface and gap varying, respectively. The top surface of the bone is fixed.
P.K. Puthumanapully et al. [161]	Maximum loads during normal walking and stair climbing. Applied contact hip and muscle forces were extracted from [186]		
M. Tarala et al. [154]	Normal walking loading conditions [188].		
M. Tarala et al. [167]	Four load increments (peak walking force, unloading, peak stair climbing force, and again unloading) are considered in each loading cycle that simulates 4 weeks in situ.		

S. Chanda et al. [153]	Maximum loads during the stance phase of normal walking and stair climbing [186], [188] are applied as two static load steps. Types of loads: muscles and hip contact forces.	
H. Mehboob et al. [163]	Maximum loads during normal walking [187], [189] applied as muscle forces and joint loads at the centre of the head stem. Post-operative conditions are considered.	
R. Ghosh et al. [160]	Maximum loads during normal walking and stair climbing [187], [189] applied as muscle forces and joint loads at the centre of the head stem. Post-operative conditions are considered.	
Hybrid Models		
Research paper	**Loading Conditions for the macroscale model**	**Loading Conditions for the microscale model**
F. Tarlochan et al. [159]	Prosthesis is coaxially fixed using the interference press fit function, and the distal part of the bone is fixed. Loads are applied to the proximal end of the stem, representing the highest reaction forces of physiological body weight and muscular forces during the stance phase of the gait cycle.	External surfaces of the bone fixed. Load applied to the implant part in the longitudinal direction and defined to match the initial micromovements obtained from the micromodel (12–25 μm). Pressure that mimics interference press fit is applied at the bottom surface of the implant.
B. Mathai and S. Gupta [177]	Maximum loads during the stance phase of four different daily activities are applied as muscle forces and joint forces.	Horizontal and vertical relative displacements were applied at the top bone surface. Values were obtained as average results from the macroscale model considering the four load cases. Bottom surface of the implant is fixed.

3.3.3. Bone–Implant Interface Contact

Predicting the long-term stability of implants requires modelling the complex nature of the bone–implant interface and the biochemical processes that govern bone remodelling and ingrowth. Simulating bone remodelling is frequently conducted by modifying the bone density value of the trabecular bone [156], [157], [158], typically using the bone adaptive theory [197]. This process is commonly combined with bone ingrowth using time-dependent adaptive modelling techniques. The fundamental principle of this modelling technique is that parameters of interest in response to the loading cases and initial conditions were calculated and then used to adapt the FE model by modifying parameters such as material properties of the tissue or element contact conditions in each load cycle interval. Depending on the main assumptions made to simulate the growth of bone within the surface of an implant, the selected studies for this review can be classified into two broad categories: Direct Contact models and Indirect Contact models. A summary of interface contact methodologies presented by the different studies belonging to these two categories is reported in Table 3.3, while the main assumptions are summarised below. The effect of considering different assumptions when estimating bone ingrowth will be discussed in the Discussion section.

3.3.3.1. Direct Contact

For direct contact models, bone ingrowth is simulated by changing parameter values directly associated with the status of the contact elements at the bone–implant interface. Typical contact statuses are: (i) *bonded*, which simulates perfect osseointegration; (ii) *gap,* representing the presence of fibrous tissue at the interface, and (iii) *frictional,* or *standard,* that reproduces initial post-operative conditions [155], [168]. Contact parameters such as contact stiffness [155] and coefficient of friction [168] are used to define the rules considered for the status change. For example, in [155], a fibrous status is obtained with a contact stiffness set to 15 N mm^{-1} [168]. Interface stiffness was also considered in [158] to determine five osseointegration levels. Relative tangential displacement between bone and implant is typically extracted as mechanical stimulus used to drive the change of the contact parameter values (e.g., 50 μm is the micromotion threshold value below which the bounded status is obtained in [156], [157]). Tensile stress and contact compressive stress are also considered for bone ingrowth and possible de-bounding [155], [158]. Typical coefficient of friction considered between the bone and coated stem for the different contact statuses are: bonded ($\mu > 0.32$), fibrous ($\mu < 0.0003$), and standard

($0.0003 \leq \mu < 0.32$) [168]. Initial interface conditions are usually set to frictionless for uncoated stems and to frictional contact for coated surfaces (a coefficient of friction of 0.6 or 1.7 in the press-fit condition).

3.3.3.2. Indirect Contact

For indirect contact models, an extra layer of elements considered between the bone and the stem is used to characterise the bonding strength, for example, by changing the stiffness value of spring elements linking in between [153], [154], [167] or the mechanical properties of the interface solid elements [161]. In [167], spring elements were activated to simulate bone ingrowth, considering stiffness values obtained from computed local micromotion, gap, and stress values. Spring length is typically defined based on the gap distance between two adjacent interfacial nodes, while stiffness values ranged between 10^{-6} N/mm (the lowest osseointegration level at the initial postoperative condition) and 30 N/mm (the highest level of osseointegration, which corresponds to bounded contact) [153]. An interface layer of solid elements was considered in most of the selected studies (Table 3.3). Mechanical properties are adjusted for each element to characterise tissue differentiation (e.g., from granulation tissue to fibrous tissue, intermediate bone, immature bone, cartilage, and mature bone), often in accordance with mechano-regulatory models and diffusion analyses of mesenchymal stem cells (MSCs), which differentiate into fibroblasts, chondrocytes, and osteoblasts. These models incorporated specific stimuli as inputs (such as relative tangential displacement at the interface, strain energy density, shear strain, and fluid/solid velocity). Oxygen concentration was considered a mechanical stimulus for tissue differentiation in [173], and capillary network formation was also included in the simulation. Typical Young modulus values set for the different tissues are: 0.2–1 MPa for granulation; 0.2–5 MPa for fibrous tissue; 5–1000 MPa for cartilage; 1000–6000 MPa for immature bone; and ≥2000 for mature bone [198]. Most of the studies used a smoothing process to average the Young modulus values considered for the material properties mapping during the simulations, thus mitigating numerical instabilities [159], [174], [177]. Typical thickness values considered for the interface layer are 0.2–1 mm. A maximum thickness layer of 5 mm was modelled in the case of macro-textural implant surfaces [162], [170]. For most of the indirect contact models that include the interface tissue layer in the proximal part of the implant, bounded contact was assumed between implant tissue surfaces and bone tissue surfaces. Frictional implant bone contact in the distal part of the coated implant was also considered in a few studies (e.g., friction coefficient values in the range 0.5–0.85) [163], [177].

3.3.4. Quantities of Interest

The long-term stability of the implant was evaluated in most of the studies by extracting results in terms of bone remodelling and bone ingrowth. In particular, bone density distribution values, or density percentage variation, were recorded during the simulation to assess the bone resorption process of the cancellous bone.

For the direct contact models, temporal evolution and spatial distribution of bounded contact elements are typically extracted to assess the bone osseointegration process [155], [157], [168]. The percentage of contact elements and the fraction of stem surface belonging to the different contact statuses were recorded for each of the seven Gruen zones in [155].

The percentage of ingrowth area and the spatial distribution of the bonding degree during the simulation were also considered for direct contact models.

As also mentioned in the previous section, typical mechanical stimuli considered to set the contact status or the tissue differentiation conditions are relative micromotions, strain energy density, tensile, and shear stresses at the interface. The quantities of interest were typically extracted at the initial contact configuration, indicating post-operative conditions, and at long-term conditions. The maximum time frame observed for extracting the simulation results was 120 days weeks [162], [170].

Table 3.3. Summary of interface contact methodologies presented by the different studies to model osseointegration at the bone-implant interface. Depending on the main assumptions made to simulate the growth of bone within the surface of an implant, two broad categories are identified: Direct Contact models and Indirect Contact models.

Research Paper	Direct Contact Models
P.R. Fernandes et al. [157]	Bone remodelling was simulated by changing the bone density of the trabecular bone and contact conditions after solving an optimisation problem that considered structural compliance and total bone volume. Initial interface conditions were set to contact with a friction coefficient of 1.7 for coated surfaces and frictionless contact for uncoated surfaces. After the first iterations, relative displacement was computed for each contact node, and if the value was <50 μm, bone ingrowth was simulated by changing the contact status at that node to bonded. Once a node is set to bond, it will remain until the end.
P. Büchler et al. [166]	Fibrous tissue formation is based on a differential equation that includes three parameters: the rate of biological evolution v and two threshold values indicating shear strains that promote the formation, ε_{min}, of bone tissue or fibrous tissue, ε_{max}. The parameters were determined to match the same thickness of fibrous tissue value obtained with experimentally observed micromotion of 20 and 150 μm after 3 weeks of evolution [192]: $\varepsilon_{min} = 2.3 \times 10^{-3}$, $\varepsilon_{max} = 8.2 \times 10^{-3}$ and $v = 5$ weeks $^{-1}$. The prosthesis was assumed to be in contact with the cancellous bone, with the friction coefficient set to 0.6.
M. Viceconti et al. [155]	The bone–implant interface was modelled with face-to-face frictional contact elements. Osseointegration was simulated using a discrete-states machine. Contact element status is set based on micromotion values d_c: *bonded* if $d_c < 40$ μm; *gap* if $d_c > 150$ μm; *frictional* if 40 μm < d_c > 150 μm. *Bonded* condition was implemented by drastically increasing the tangential contact stiffness and the normal contact stiffness. *Gap* status assumed fibrous tissue between bone and implant, which was modelled using the stiffness relaxation technique [199]. A contact stiffness of 15 N mm $^{-1}$ was set to produce a 500 μm gap. *Frictional* status is modelled as an elastic frictional contact. The contact stiffness was set at 3×10^4 N mm $^{-1}$ to ensure peak penetration less than 1 μm. De-bonding was checked after the initial contact settings based on the stress threshold. Elements return to the friction status if: tensile stress > 0.8 MPa or shear stress > 4.9 MPa.
M. Viceconti et al. [168]	The bone–implant interface was modelled with face-to-face frictional contact elements. Osseointegration is simulated using a continuous and rule-based model and described for each time step and generic point at the interface with a first-order model in which the coefficient of friction μ is expressed as a function of the shear stress and micromotion. State of each contact element depends on the friction coefficients: *bonded* (μ > 0.32), *fibrous* (μ < 0.0003), and *standard* (0.0003 ≤ μ < 0.32).
J. Folgado et al. [156]	Bone remodelling was simulated as in [157]. Initial interface conditions were set to contact with a friction coefficient (0.6) for coated surfaces and frictionless contact for uncoated surfaces. After the first iteration, the relative displacement d was computed for each contact node. Two micromotion threshold values (d < 25 or < 50 μm) for the bonded contact state were analysed separately.
R.B. Ruben et al. [158]	Bone remodelling was simulated as in [157]. Contact elements changed status with a rule-based algorithm. Bone ingrowth occurs if all these five conditions are satisfied: relative tangential displacement < 25 μm; gap < 150 μm; tensile stress < 0.8 MPa, contact compressive stress < 7.89 MPa; shear stress below threshold values depending on the interface stiffness and related osseointegration level (e.g., shear stress should be less than 4.5 MPa when interface stiffness is zero, which corresponds to osseointegration level 1 and the initial simulated period immediately after surgery).

	Interface stiffness increases by one level until level 5 is reached, if all criteria are satisfied. Interface stiffness can return to zero if one of the conditions is not satisfied.
Research paper	**Indirect contact models**
P. Moreo et al. [164]	Bone remodelling and bone ingrowth were simulated based on the theory of continuum damage mechanics. Interface damage or interface repair was modelled by changing tissue stiffness (i.e., bounding degrees) defined based on mechanical stimuli (e.g., relative displacement at the interface). The bonded/debonded process was implemented using thin elements that connect the bone and implant with frictionless contact between the surfaces.
X. Liu et al. [174]	Two models were used to simulate osseointegration. In the first model, the mechano-regulatory model and diffusion analysis described in [200] were used for the differentiation of MSCs into fibroblasts, chondrocytes, and osteoblasts. The new tissue type was predicted for each element, and the effective material properties were assigned based on [200]. The second model used a modified tissue differentiation algorithm that allowed a change from immature bone to mature bone and the reverse change (bone resorption).
A. Lutz et al. [176]	Bone ingrowth was simulated using a linear elastic bioactive interface layer. An evolution rule for osseointegration based on normal pressure and relative motion was considered to change the tissue stiffness.
S. Checa et al. [173]	A lattice model that represents a space for the extracellular matrix and cells was considered for the tissue differentiation algorithm. Cells can proliferate, migrate, and differentiate according to the mechanoregulation algorithm proposed in [169], which also included the growth of the capillaries. Oxygen concentration and two mechanical stimuli, shear strain and fluid/solid velocity, were used for the differentiation of MSCs into fibroblasts, chondrocytes, and osteoblasts. Osseointegration was implemented considering a bone–implant interface layer of 1 mm thick regenerative tissue of poroelastic elements.
P.K. Puthumanapully et al. [161]	A uniform layer of 0.75 mm (corresponding to three layers of porous coating thickness in the Proxima implant) was created around the implant to represent the formation of granulation tissue. This layer was assumed to be fully bonded to the implant and the bone. Tissue differentiation algorithm based on the mechano-regulation theory from Carter et al. [201]. The tendency for ossification was represented by the osteogenic index 'I', dependent on the element stress state at each cycle. A low value of I denotes the tendency to form fibrous tissue. The index was mapped onto a range of material properties, considering an interpolated value of the Young's modulus of the materials. Values were averaged over 10 iterations to avoid rapid changes in tissue type from one iteration to the next. Convergence was obtained after about 50 iteration or when the change in tissue type between two successive iterations in every element in the layer was less than 5%.
M. Tarala et al. [154]	Bone ingrowth simulated by activating spring elements based on micromotion (less than 40μm); gap value (smaller than 500 μm); local stresses (less than 25 MPa). De-bonding (spring elements deactivated) occurred when local bone stresses exceeded 25 MPa. Frictional implant–bone contact (coefficient was 0.5 or 0.88 for different materials of the stem). The spring stiffness was defined as the summation of the adjacent bone elements' Young's Modulus was multiplied by 1/3 of the corresponding element face area (each face had three nodes connected to it), divided by the original spring length (equal to the gap between implant and bone node). Bone remodelling was simulated only for the cases with the best bone ingrowth performance. Adaptive bone theory was used [197].
A. Andrade-Campos et al. [152]	The bone–implant interface was modelled with a surface-based contact model with the penalty method (the stem is the master surface and the bone is the slave). Bone remodelling was simulated using an optimisation process that computes the evolution of volume fraction (0 void; 1 total density corresponding to cortical bone) at each point based on strain energy density values. Osseointegration was simulated by changing the stiffness of connector elements included between the bone and the stem based on a relative displacement criteria described in [157]. Osseointegration increases when the contact is achieved (normal contact force >1) and the tangential displacement is less than a threshold value. If these conditions were not verified, the initial contact conditions (contact with friction 0.3 if the surface is coated and frictionless contact for uncoated surfaces). Fully osseointegration was modelled with glued contact. De-bounded was also possible for high levels of stress (contact pressure > 0.8 MPa and shear stress > 35 MPa).

A. Lutz et al. [178]	An interface layer made of solid elements is considered between the bone and implant surfaces, with the initial constitutive behaviour described by the Drucker–Prager plasticity model [202]. Osseointegration is simulated considering the evolution of bone mineral density as a function of the mechanical stimuli (micromotions and strain energy density): interface stiffness, ability to carry tensile loads, and the limit until sliding occurs, which increases with ongoing mineralization.
M. Tarala et al. [167]	Bone ingrowth was simulated by activating spring elements with stiffness based on the ingrowth potential parameter *P*, which was computed based on the local micromotion stress and gap value micromotion (micromotion less than 40μm, gap value smaller than 1 mm, and local stresses less than 25 MPa). A non-linear progression of the spring stiffness was considered with *P*. A complete ingrowth was assumed after four loading periods ($P = 1$) under ideal conditions of micromotion and a gap equal to zero. Frictional implant-bone contact (coefficient 0.5).
F. Tarlochan et al. [159]	Microscale model of porous structures made of titanium alloy was constructed with a fixed RVE (representative volume element). The beads were initially placed inside a granulation tissue (callus) and penetrating the bone. The callus was tied to the bone and the prosthesis surface; sliding contact with a coefficient of friction of 0.4 was used between the beads and the callus and between the bone and the beads. An algorithm based on the biphasic mechano-regulation theory from Isaksson et al. 2006 [198] was used to predict tissue differentiation, including granulation tissue, fibrous tissue, intermediate bone, immature bone, cartilage, and mature bone. According to a stimulus computed using deviatoric strain and fluid flow, the material properties of the callus were updated in each element. A smoothing process was used to average the Young modulus values considered for the material properties mapping during the simulations.
S. Chanda et al. [153]	The bone–implant interface was modelled with large sliding surface-to-surface frictional contact elements. Bone remodelling is simulated using adaptive bone theory [13]. Bone ingrowth is simulated using contact, and spring elements (CONBIN14) are activated when the five conditions described in [158] are satisfied. Initial contact stiffness is assigned to ensure a low penetration [155] and a friction coefficient set to 0.4. Stiffness values for spring elements range between 10^{-6} (osseointegration level 1 at the initial post-operative condition) and 30 N/mm (the highest level of osseointegration, which corresponds to bounded contact). Spring length is defined based on the gap between two adjacent interfacial nodes.
R. Ghosh et al. [162]	A maximum thickness for the granulation tissue of 5 mm was assumed between the implant and the bone. The implant–tissue interface and bone–tissue interface were considered perfectly bonded. The mechano-regulatory model and diffusion analysis described in [200] were used for the differentiation of the MSCs into fibroblasts, chondrocytes, and osteoblasts. The new tissue type was predicted for each element, and the effective material properties were assigned based on [200]. The simulation was carried out for 120 iterations, which corresponded to 120 days.
H. Mehboob et al. [163]	Two tissue layers of 0.5 and 1 mm thick were considered to simulate the granulation tissue (callus) only at the proximal end of the stems. The callus was tied to the bone and stem surface. Ain the distal part, a surface-to surface frictional contact (0.5) was used between the stem and the bone. An algorithm based on the mechano-regulation theory from H. Isaksson et al.[198] was used to predict tissue differentiation. According to a stimulus computed using deviatoric strain, the material properties of the callus were updated for each element. A total of 16 iterations were considered for the entire simulation.
B. Mathai and S. Gupta [177]	An inter-bead granulation tissue of 850 μm was initially modelled with a fixed RVE only at the proximal part of the stem. The beads were assumed to penetrate the bone layer by 5 μm. Fully bonded contact was assumed between the tissue and the surfaces of the implant and bone. At the distal part, the implant-bone interface was modelled using a surface-to-surface contact with a frictional coefficient of 0.85. The tissue differentiation modelling technique presented in [162] was used. A temporal smoothing method was used to average the material properties assigned, avoiding numerical instabilities. The simulation was carried out for 60 iterations, which corresponded to 60 days.
R. Ghosh et al. [165]	A granulation tissue (minimum thickness of 2 mm) was assumed between the implant and the bone. The implant–tissue interface and bone-tissue interface were considered perfectly bonded. The tissue differentiation modelling technique and simulation scheme presented in [162] were used. The simulation was carried out for 120 iterations, which corresponded to 120 days.

R. Ghosh et al. [160]	A layer of granulation tissue (1 mm thick) was included around the proximal stem surface by Boolean subtraction operation. Both implant-tissue interface and bone–tissue interface were considered perfectly bonded. In the distal part of the implant, a surface-to-surface contact was modelled between the implant and the bone with a coefficient of friction of 0.5. The tissue differentiation modelling technique presented in [162] was used. The simulation was carried out for 56 iterations, which corresponded to 56 days.

3.4 Discussion

From this state-of-the-art review of the FE models predicting the AL failure, the main advantages and limitations of the different modelling approaches adopted by various authors have emerged.

One of the most critical aspects when simulating the long-term stability of hip prostheses is modelling the complex osseointegration processes occurring at the femur–implant interface. The adaptative FE model was found to be a widely used technique to simulate osseointegration. Finite Element software such as Ansys and Abaqus was typically coupled with user subroutines programmed in Python or Matlab to iterate and integrate the calculations. Both bone remodelling and bone ingrowth, essential for maintaining the secondary stability of the cementless stem, should be included in the simulations. Since they are related processes in vivo (e.g., bone ingrowth is influenced by factors related to bone remodelling), most FE studies considered a combination of the two implemented within the same workflow loop [152], [153], [156], [157], [158], [164], [174]. Bone ingrowth and bone remodelling were considered two independent phenomena in a few models [152], [154]. "Bone ingrowth" refers to the growth of bone within the irregular surface of an implant or its intimate contact at the bone–implant interface following the biological response. "Bone remodelling" involves the removal of mineralised bone by osteoclasts (bone resorption/bone loss/osteolysis) followed by the formation of bone matrix through the osteoblasts that subsequently become mineralised (bone apposition or bone formation) [203], [204]. In this last process, the biological process of cell differentiation, also known as "bone adaptation", plays a crucial role.

It is worth noting that bone remodelling was often simulated as bone mineral loss associated with the so-called stress shielding phenomenon. While bone resorption is indeed a biological process correlated with an increased risk of implant loosening, AL cannot be solely attributed to bone density loss. Therefore, this review focused more on papers that predicted bone ingrowth failure or the combined effects of the two processes.

As also reported in Section 3.3., two main bone interface contact modelling techniques were identified and named as direct contact and indirect contact models. The first are more computationally efficient; however, regarding their main assumptions, some limitations should be pointed out. For example, in a few direct contact models, only one mechanical stimulus controls the change in contact status, and the outcome is such that once the contact behaviour is set to be bonded, it will remain in that state until the simulation process is complete [156], [157]. Certain direct contact models addressed this limitation by incorporating additional criteria for debonding checks [155], [158]. The indirect contact models involving spring elements also overcome this problem by varying the osseointegration level with different spring stiffness values [153]. The mechano-regulatory models and diffusion analyses of mesenchymal stem cells included in many indirect contact models that considered an interface layer enabled a more realistic mimicry of biological progressions and simulation of tissue differentiation processes [160], [162], [165], [174]. However, most of these models assumed that, even under initial post-operative conditions, the implant is surrounded by a layer of granulation tissue, whereas, in reality, the implant is in direct contact with the bone. Some uncertainties related to the definition of the

micromotion threshold value used to estimate bone ingrowth were observed. For example, P.R. Fernandes et al. [157] considered a threshold value of 50μm below which the contact status was set to bounded. M. Viceconti et al. [155] adopted a similar approach with a 40μm micromotion threshold value. J. Folgado et al. [156] compared two threshold values of 25 and 50μm while determining whether the element was bonded or frictional. They showed a significant impact on the prediction of bone ingrowth. Bone ingrowth on the partially coated cylindrical stem was absent when the micromotion criterion was set at 25 μm, but some ingrowth was observed when the criterion was relaxed to 50μm. Micromotion thresholds of 50, 75, and 100 μm have also been investigated by A. Lutz et al. [178], and it was shown that for higher micromotion thresholds, the predicted osseointegration was also higher.

Some microscale models mimicking only local bone implant interfaces were proposed to investigate osseointegration and reduce the computational cost of the simulation [162], [165], [173], [174]. Although these models can more accurately and efficiently simulate the biochemical processes occurring at the interface, the influence of the anatomical topology of the bone, patient and implant variabilities, or loading scenarios on bone ingrowth would be limited.

Loading cases are another crucial consideration for predicting the long-term stability of the implants. In particular, the iterative computational process necessitates careful selection of load cycle intervals; otherwise, it may yield inaccurate results [205]. Also, as we mentioned above, the loading cases for the microscale models were limited, mainly based on constant shear loads or tangential displacements. The hybrid method proposed in [159], [177] represents a good combination of the advantages of both macroscale and microscale modelling approaches: it integrates the results obtained by solving the macroscale model, thereby capturing the overall behaviour of the system, with the loading configuration considered from microscale models. For the macroscale models, the peak value of the hip joint force of normal walking and stair climbing was most widely used. Reducing the number of discretization sub-steps for the hip joint load resulted in accurate mechanical stimulus for osseointegration at the bone–implant interface [178], which could serve as a practical reference when considering methods to reduce computational expense. Although the effect of various loading cases, including different postoperative conditions, on bone ingrowth results has been analysed in a few studies [160], [164], we still have limited knowledge regarding which set of loading cases best predicts in vivo conditions. Also, one notable observation is that, to the best of the author's knowledge, no simulation has yet considered an abnormal gait cycle associated with various pathologies or conditions affecting the musculoskeletal system. In the future, it would be meaningful to investigate how abnormal gait patterns affect the results of osseointegration computational models.

One last critical point worth mentioning is model validation. Traditional validation activities typically involve a rigorous comparison of the model predictions with the results obtained from the comparator (i.e., bench testing, clinical trials, animal experiments) [206]. For current bone osseointegration models, the existing literature acknowledges a lack of sufficient experimental and clinical data to robustly validate the computational models [162], [177]. Another big challenge for these FE models is not only accurately predicting

the osseointegration process in vivo but also determining when it occurs and identifying whether it ultimately caused the implant to loosen. Very few studies provided quantitative comparative evidence in terms of bone ingrowth (e.g., percentage of the osseointegration area, fibrous tissue thickness) between the computational results and the clinical data [155], [156], [166]. A comparison between the relative micro-movements predicted by the models and the experimental measurements taken in vitro was mentioned in [168]. Qualitative agreement between simulation outputs and clinical observations was often used as model plausibility evidence. For example, a few authors found that bone ingrowth does not occur uniformly across the coated surface but rather partially [152], [156], [157]. More bone formation was observed on the medio-lateral sides and towards the proximal regions of Gruen zones 2 and 6 [160], [161], which is in agreement with the radiographic results from the five-year follow-up study [207]. An interesting Ansys-to-DEXA conversion technique to present simulation results with clinical relevance was described in [153]. This involved converting the density values of the FE elements into two-dimensional pixel grey values and considering the differences in grey values between post-operative and long-term predictions across the seven Gruen zones.

3.5 Conclusions

In conclusion, the present study provides a comprehensive analysis of the main FE models predicting the AL failure risk induced by the lack of long-term stability. The main modelling assumptions, including bone and implant geometry, materials, boundary conditions, and the bone–implant interface, were summarised and presented. The limitations of various modelling assumptions and their impact on the simulation results were also discussed. Technical differences and trends in methodology evolution have been observed. Specifically, the modelling of long-term stability in femoral stems has progressed from macroscopic direct contact models to more advanced indirect models integrating interface layers. Microscale or hybrid models, focusing on localised regions at the interface, have grown in complexity, incorporating detailed surface porous structures and sophisticated tissue differentiation algorithms. This progress has been made possible thanks to the growth of available computational resources.

Although several important improvements in computational modelling have been made, it is evident that further advancements are needed. In particular, more rigorous step-by-step clinical validation for osseointegration models would be crucial for translating computational methodologies into clinical practice. Failure criteria used to determine loosening of the implant should be clearly defined, and effort should be made to identify the appropriate limit of tolerable conditions (e.g., maximum micromotion at the interface) considering implant, patient, and environmental factors, as also suggested by [208].

Extra attention should also be paid to the terminology used to present FE studies on AL. Terms such as “bone ingrowth”, “bone remodelling” and “bone adaptation” are often used interchangeably to define the osseointegration process since they all include the bone formation description.

Chapter 4

Development of a patient-specific model to predict primary stability of hip implant

4.1 Overview

Osteoarthritis carries a significant socioeconomic burden; among people who live to age 85, the lifetime risk of suffering hip OA has been estimated at 25.3% [209]. The prevalence of hip OA and other hip joint disorders has been discussed in Section 1.1.3. At the macroeconomic level, the direct and indirect expenses of OA treatment represent a high proportion of healthcare expenditure. It was reported that the costs account for 1–2.5% of the gross national product in developed countries, and are expected to quadruple by 2030 [210]. Total hip replacement (THA) is currently one of the most common and successful orthopaedic surgeries for the treatment of hip osteoarthritis. Increasing amounts of THA registries are now available and provide clinical outcome reports (see Section 1.2.4). Therefore, innovations in femoral stem design—including advances in material, geometry, surface coating, fixation technologies and surgical techniques—have led to a steadily expanding portfolio of available implants during the last decade. Particularly, cementless implants, which gained popularity due to the long-term durability and strong biological bond with the patient's bone, offer a potential for greater longevity.

At the same time, it underscores the need for more stringent and systematic approaches to evaluate a novel medical device's performance. Before introducing a new medical device to the market, clinical trials are required to assess its safety and effectiveness. Orthopaedic prostheses are generally classified as a Class III medical device due to their high-risk nature as an implantable device that sustains and supports the body [211]. As such, they require the strictest pre-market approval under both U.S. and European regulatory frameworks. In Europe, compliance with the Medical Devices Regulation (MDR) [212] should be followed. However, the clinical testing is accompanied by practical and methodological limitations. For hip implants, the duration of clinical trials lasts at least 2 to 5 years for short-term outcomes, such as joint functional recovery, pain reduction, and early implant performance. Long-term studies extending over 10 to 25 years are necessary to assess late complications, such as wear or aseptic loosening (AL). Post-market surveillance, aiming to collect large-scale retrospective data, may take decades, which is inherently challenging. Besides, participant populations are often limited. It hinders the acquisition of sufficient data on rare clinical cases and small-volume implant design variants.

As valuable alternatives, *in silico trials* refer to the use of computer modelling and simulation to evaluate the performance of medical devices. Compared with traditional clinical trials, this approach improves feasibility

and allows the optimisation of trial design with smaller sample sizes. By generating virtual patients, it reduces reliance on human and animal participants, aligning with the principles of replacement, reduction, and refinement in experimentation as suggested by the MDR. Generally speaking, *in silico medicine* is progressively gaining recognition, but is not yet universally accepted. Standards for in silico medicine are currently being developed within the regulatory framework. Viceconti et.al [213] highlighted the importance of an accurate definition of the Context of Use (CoU), which is the first step in the regulatory approval process of any new methodology. The CoU indicates the specific role and scope of the computational model used to address the question of interest [214]. A taxonomy of in silico trial CoUs and 46 potential applications were summarised in their work [213].

Within this context, finite element (FE) analysis, combined with musculoskeletal (MSK) modelling, has become a powerful tool for outcome assessment in THA. By creating a virtual replica of a patient's anatomy (Digital Twin), surgeons and engineers can conduct a personalised surgical plan, simulate physiological loading conditions and quantitatively estimate implant failure risk prior to surgery. Moreover, a standardised modelling workflow enables more systematic and reproducible simulation, as shown in Fig. 4.1; thereby enhancing efficiency and providing a robust in-silico framework to support preclinical evaluation and clinical decision-making.

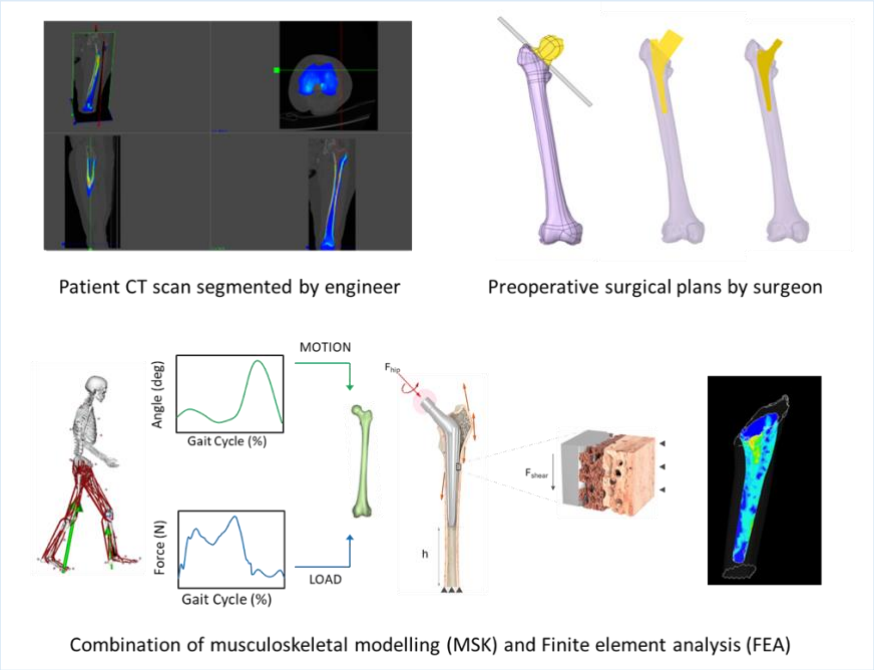

Figure 4.1 Overview workflow of the computational model to estimate the implant failure risk prior to surgery.

The objective of this thesis is to develop an *in silico trial* to estimate the risk of AL in an anatomical cementless hip stem design. Because AL remains the predominant late failure mechanism in cementless THA (common failure modes and mechanics detailed in Section 1.3.1). A patient- and surgery-specific FE model was developed to predict the *primary stability* (the relative micromotion in each point of the bone-implant contact surface induced by physiological activities such as level walking or stair climbing) of a commercial stem

design (Apta, Adler Ortho, Milan, Italy), for which extensive clinical experience is available. This chapter will describe in detail the modelling framework, including FE model construction, boundary conditions, meshing convergence study, contact analysis and results postprocessing.

4.2 Method and Material

4.2.1 FE Model Construction

A preliminary FE analysis to estimate the primary stability of the hip implant was conducted. The following sections include the geometry generation for both femur and implant; the virtual surgical implantation; material assignment; meshing; and boundary conditions, which are the foundation of an FE model. To ensure the reliability of the simulation results, a mesh convergence study was conducted to validate the adequacy of the element size and mesh quality.

4.2.1.1 Geometry and Surgical Planning

The femur geometry is sourced from the HFValid open-access data collection: Hip-Fracture Validation Collection (https://amsacta.unibo.it/id/eprint/7126/). The 3D shape of each femur was segmented from the CT scan, using open-source software (3D Slicer, v. 5.2.1). The implant was a commercial stem design (Apta, Adler Ortho, Milan, Italy), an anatomical stem. The stem geometry was provided by the company.

To simulate the surgical implantation procedure, the implants were virtually placed into the femur model through a user interface named HiPlan directly by the surgeon [215]. The resection plane for obliquely resecting near the femoral neck was carefully determined to preserve the less trochanter, following typical surgical practice. As shown in Fig 4.1 The multimodal display interface is a visualization paradigm where anatomical objects are represented through multiple views, each one simulating a different imaging modality familiar to the medical professionals, the intended end users of the application.

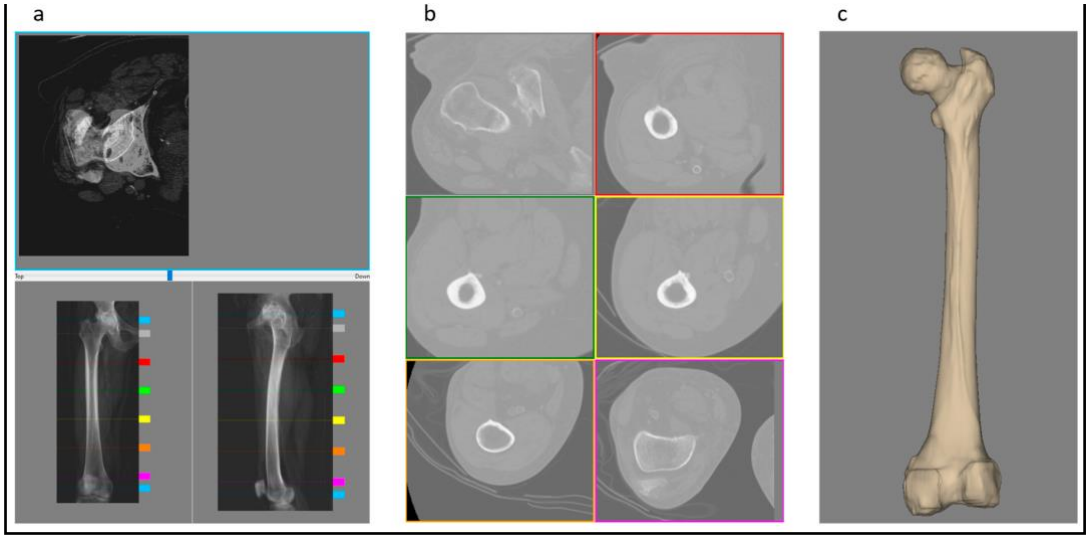

Figure 4.2 A virtual surgical plan was conducted by a surgeon based on the in-house software. The multimodal display principles. (a) The RX window where the CT dataset is represented as two orthogonal radiography projections: antero-posterior view (bottom left) and medio-lateral view (bottom right), together with a merged view (top) of two CT slices to visualise the femoral anteversion. The coloured sliders at the edge of the RX-projection image are used to choose the CT slices for the anteversion representation (blue sliders) and (b) the CT slices of the CT-window (sliders from grey to magenta); (c) the 3D-window, where the femoral bone is represented with a surface rendering. Reprinted from [215].

In collaboration with the surgeon, the software precisely defined the spatial relationship between the bone, implant, and resection plane. The corresponding rasp geometry is customised to the stem geometry, where the proximal grooves were filled, and the lateral-proximal section was extended to leave space to allow for intraoperative attachment of an inserter instrument, as shown in Fig. 4.2. The rasp was virtually positioned at the intended implant location to simulate canal preparation. Subsequently, all components were adjusted to the planned positions. Using the Boolean operation in SpaceClaim (Ansys release 2023 R2, ANSYS, Inc., Pennsylvania, USA), the resected femoral head was digitally removed from the intact bone model, and the canal for the implant was virtually created by subtracting the rasp geometry from the femur (Fig. 4.2). The final position of the stem was verified using CT scans in Mimics (Materialise, Leuven, Belgium) to ensure direct contact between the implant and the cortical bone in the proximal femur (Fig 4.3), which is essential for anatomical stems to achieve proximal fixation and promote long-term osseointegration.

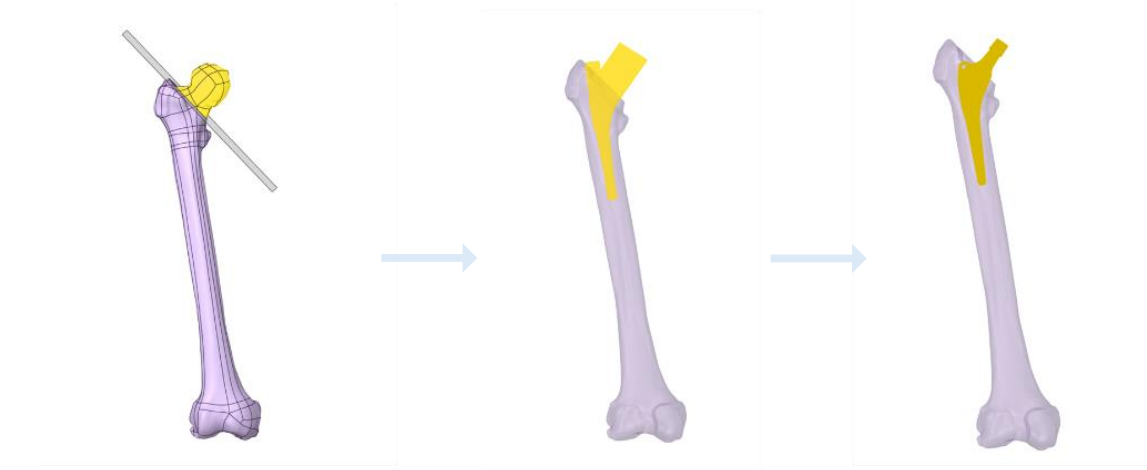

Figure 4.2. Pre-processing of bone and prosthesis geometries to simulate surgical implantation. From left to right: the femoral head was resected, followed by canal preparation using a virtual rasp, and finally, the femoral stem was positioned within the prepared canal, using the Boolean operation in SpaceClaim (Ansys release 2023 R2, ANSYS, Inc., Pennsylvania, USA).

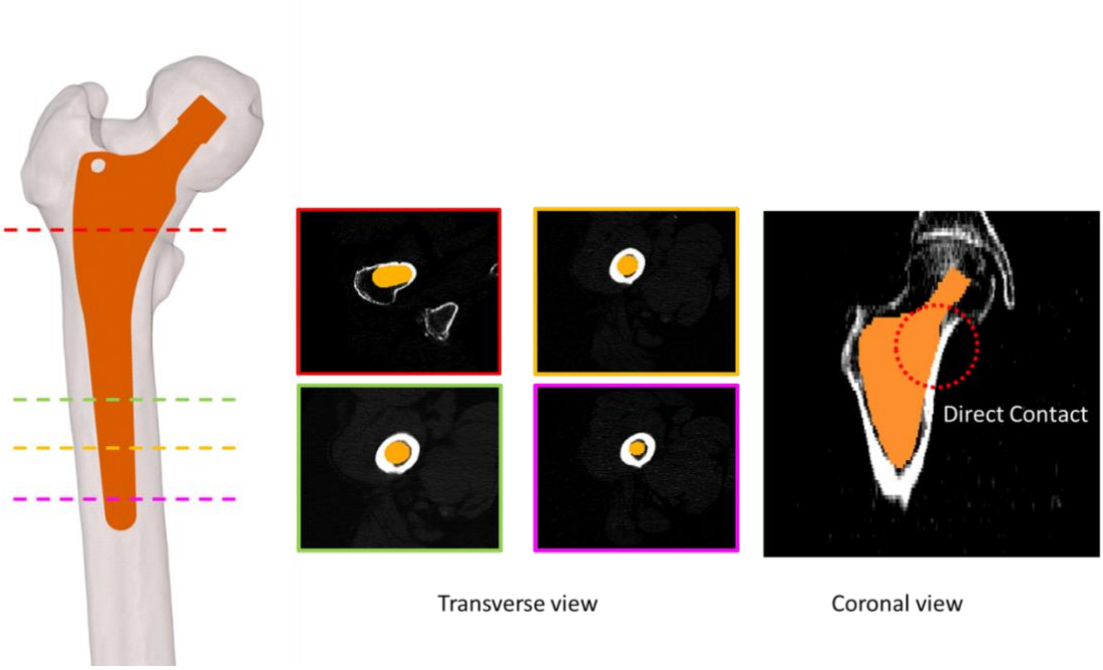

Figure 4.3. Verification of implant-to-bone contact in the coronal plane with a CT scan from both transverse and coronal planes confirms the direct contact between the anatomical stem and the cortical bone in the proximal femur.

4.2.1.2 Meshing and meshing convergence

Both bone and implant were meshed with quadratic tetrahedral elements (Bone element size: 1.5 mm; implant element size: 1.5 mm) in ICEM (Ansys release 2023 R2, ANSYS, Inc., Pennsylvania, USA). Mesh convergence is a fundamental requirement in FE analysis to ensure that the numerical solution is independent of the meshing discretisation. However, the inherent discontinuities in contact analysis—such as nonlinear contact states or abrupt stress/strain field variations propose significant challenges to achieving this convergence. To address this, instead of focusing on directly assessing the sensitivity of contact response indicators, the mesh convergence analysis begins with the underlying solid domain. The classical approach is the patch test, a consistency benchmark in finite element theory originally proposed by Bruce Irons [216]. The test evaluates whether a finite element type can correctly represent uniform or linearly varying stress or strain fields, thereby confirming the formulation's internal equilibrium and compatibility. To monitor convergence in the solid region of our model, strain energy density (SED) is selected as the principal measure. At the same time, because contact conditions may exhibit sensitivity to mesh resolution, an additional indicator—maximum contact sliding distance was also tracked. By combining these two perspectives, the convergence evaluation accounts for both internal structural consistency and the numerical behaviour at the contact interface. The mesh convergence tests were summarised in Table 4.1. Five mesh densities (S0–S4) were evaluated, with element sizes for the bone and stem ranging from 3.0 mm to 1.0 mm, corresponding to degrees of freedom (DOF) from approximately $8.79\times10^{5}$to 2.25×10^{7}. The specific procedure implemented is as follows:

a) The node corresponding to the highest SED in the coarsest mesh (3 mm) should be first located.

b) A hard point constraint is then assigned to this position to ensure a node exists at the same spatial coordinate in all other refined meshes.

c) For each level of mesh refinement, the SED at this fixed location is measured and compared across configurations to assess convergence trends.

d) Simultaneously, the selected contact metrics are extracted to investigate how sensitive the contact response is to mesh variation.

Table 4.1 Mesh convergence evaluated five mesh densities (S0–S4), with element sizes for the bone and stem ranging from 3.0 mm to 1.0 mm; corresponding degrees of freedom was listed.

	Element size of bone and stem	DOF
S0	3 mm	8.79×10^{5}
S1	2.5 mm	1.50×10^{6}
S2	2 mm	2.89×10^{6}
S3	1.5 mm	6.78×10^{6}
S4	1 mm	2.25×10^{7}

4.2.1.3 Material

Bone material assignment was done by mapping the local HU according to the CT scan of the patient (Bonemat, Istituto Ortopedico Rizzoli, Bologna, Italy) [217]. To avoid ash-density underestimation and overestimation for low- and high-density bone tissue [218], calibration was performed to ensure the accuracy of the bone density estimation based on CT data. Both cortical and cancellous bone were considered. The Apta-fix Adler stem was modelled as a homogeneous material with Young's modulus of 120 GPa, representing the Titanium alloy. Poisson ratio was defined as 0.3 for both bone and implant.

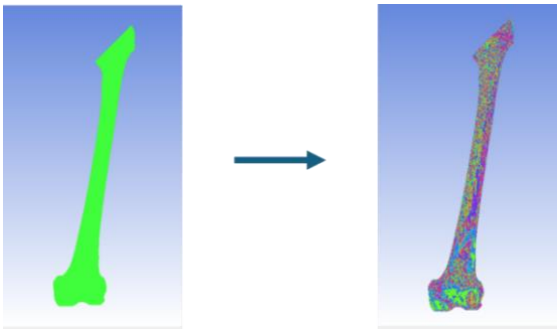

Figure 4.4. Bone material mapping based on DICOM dataset.

4.2.1.4 Boundary conditions and solutions

Loading cases from the literature were typically applied as hip contact forces and muscular load (Fig3.2. Muscle loads are distributed over the respective attachment areas or considered rigid plates attached to the

stem and femur to avoid stress concentration. For the current work, we only applied the hip contact force, which was considered as the peak load during normal walking or stair climbing according to the patient's body weight.

Two physiological loading cases were considered: level walking and stair climbing. The reference coordinate system (CS) was defined with its origin at the centre of the femoral head, with the X-axis directed from lateral to medial, the Y-axis from anterior to posterior, and the Z-axis from bottom to top. The force was applied at the surface of the implant top surface (Fig. 4.4), representing the load transfer from the postoperative femur head centre to the implant stem. In all models, the femur was constrained by fixing a 200 mm-long distal segment of the femoral shaft to eliminate rigid body motion. The magnitudes and directions of the applied loads, corresponding to a 70 kg body weight, are summarised in Table 4.2.

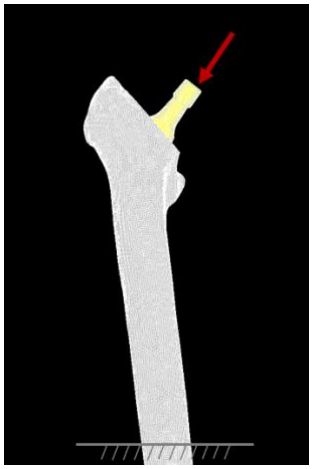

Figure 4.4. The hip contact force is applied for current FE tests, 200 mm-long distal segments of the femoral shaft, to eliminate rigid body motion.

Table 4.2: Summary of loading cases applied in the finite element simulations. Forces are expressed both as a percentage of body weight (BW) and as absolute values scaled to a reference body weight of 70 kg.

Loading Cases	Force (Percentage of BW)			BW (kg)	Force (N)		
	Fx	Fy	Fz		Fx	Fy	Fz
Level Walking	-54	33	-229	70	-370	225	-1572
Stair Climbing	-59	61	-236	70	-407	416	-1621

4.2.2 Contact Analysis

Accurate evaluation of the relative sliding at the bone–implant interface is crucial for predicting the risk of AL in cementless femoral stems and assessing the outcome of the preoperative surgical plans. As a result, contact analysis plays a vital role in this study, as it directly determines how the computational model reflects the complex mechanical interactions between the femur and the implant. The following sections consist of the details of contact analysis modelling strategy, parameter definition, algorithm development, and data processing method to capture the nonlinear behaviour at the bone–implant interface.

4.2.2.1 Contact Area Selection

ANSYS Mechanical APDL provides an option for automatic detection of contact pairs between two objects. However, this built-in method is not stable and flexible enough. Detected pairs can vary between models, making it difficult to compare different test groups. Instead of manual selection, the present study developed a method for defining contact regions, ensuring both accuracy and reproducibility across all simulations. Given that micromotion affects bone ingrowth primarily at the coated surface of the implant, the coating region of the femoral stem was defined as the primary target area, as shown in Fig. 4.5. Based on the landmarks of the stem, the local coordinate system with the origin at the top stem neck centre was generated for the coating region selection. Then these coated surfaces were paired with the adjacent bone surface to form the contact interface. In this way, every specific implant has the same region contributing to the contact pair with a different femur, laying a basis for the design of experiments of our study in the next chapter to investigate the factors that affect the failure risk in the patient-surgery-specific model.

To give directionality to the contact pair, one of the surfaces, called the Mover (called Contact in ANSYS), is the one that comes into contact with the other, called the Target. Generally, if one of the bodies is significantly stiffer than the other, it should be defined as the Target. In this study, the bone side was defined as the contact, and the implant as the target.

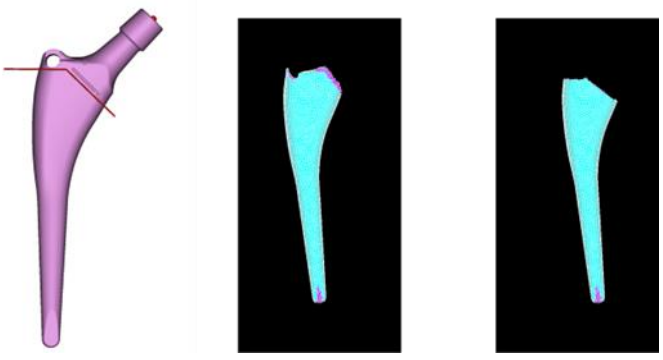

Figure 4.5 The coating region of the femoral stem was defined as the primary target area. The automatically detected contact area was further trimmed to obtain a precisely and parametrically defined coating region.

4.2.2.2 Contact Configuration

At the bone–implant interface, the contact was defined as a face-to-face, large-sliding, frictional contact [219] in Ansys Mechanical APDL (Ansys release 2023 R2, ANSYS, Inc., Pennsylvania, USA). Interface behaviour that is modelled as frictionless or by classical Coulomb's friction cannot fully represent the non–linear interface behaviour of the bone-implant interface.

The contact behaviour was assumed to be asymmetric, allowing the contact pair to have distinct target and contact surfaces, thereby reflecting the physical interaction more realistically. A friction coefficient of 0.3 was applied, which is widely reported in the literature for the interface between bone and Titanium alloy [183] (Table 3.3). For each contact pair, a number of control points are controlling the compenetrating, which have to be "pushed-out" at the following iteration. In this study, it is monitored at the nodes of the elements' faces, part of the contact pair. The interface contact non-linearity behaviour was solved with the Augmented Lagrange algorithm. In ANSYS, the main contact algorithms are penalty-based and Lagrange-based, which differ in how the contact interaction is treated mathematically. The penalty formulation enforces contact constraints by applying a stiffness proportional to the penetration, which makes it computationally efficient and stable but allows finite interpenetration between the contacting surfaces. The normal Lagrange formulation, by contrast, enforces a strict no-penetration condition through Lagrange multipliers, providing higher accuracy but at the cost of larger system matrices, longer run times, and potential convergence difficulties such as chattering. As a compromise, the Augmented Lagrange formulation combines the advantages of both approaches. It starts with a penalty-type stiffness to establish contact forces and then iteratively updates the Lagrange multipliers to minimise penetration.

4.2.2.3 Quantifying Bone–Implant Interface Motion

Commercial finite element software provides a wide range of solutions for contact modelling. In ANSYS Mechanical APDL, the sliding distance between paired contact elements can be directly obtained as an output. However, this method has inherent limitations: the sliding value is only calculated when the contact is fully closed, meaning that the two surfaces are in direct physical interaction. When the interface is in an open state—such as when a small gap exists between the bone and the implant—the software is unable to provide an accurate sliding distance. In addition, when the loading step is divided into multiple sub-steps, the relative micromotion between the bone and implant cannot be accurately represented by simply calculating the displacement difference between the initial and final positions. This is because the movement at the bone implant interface might not be a linear behaviour due to the irregular geometry of the contact surface. To overcome this issue, a custom computational method was applied to define the relative micromotion, ensuring a continuous and comprehensive characterisation of interface behaviour. The displacements across all sub-steps were incrementally summed. This approach provides a more realistic and clinically relevant representation of the complex, non-linear interaction at the bone–implant interface. A fully automated workflow was developed in Ansys Mechanical APDL (Ansys release 2023 R2, ANSYS, Inc., Pennsylvania,

USA) and MATLAB (Version R2022a, MathWorks, Inc., Natick, Massachusetts, USA). The overall procedures consist of the following steps:

(a)Data Extraction

At each loading sub-step, the three-dimensional coordinates and displacement data of both contact nodes (bone side) and target nodes (implant side) were extracted from APDL. This dataset, which included the spatial coordinates and unique identification numbers (IDs) of all nodes, served as the foundation for subsequent node pairing and displacement tracking.

(b) Node Pairing

For each contact node, search for the nearest target node by calculating the Euclidean distance between nodes. In regions with highly irregular geometry or where no direct vertex match existed, the algorithm located the target element whose centroid was closest to the contact node. This ensured that every contact node was consistently assigned to a corresponding target node.

(c) Local Coordinate System Construction

A local Cartesian coordinate system was generated for each contact corner node within APDL: The X and Y axes were aligned with the local tangent plane of the interface surface. The Z axis was oriented normal to the interface surface. As loading progressed, the origin of each local coordinate system was dynamically updated after every sub-step to maintain precise tracking of tangential motion.

(d) Relative Micromotion Calculation

For each paired node, the relative tangential displacement was computed as the difference between the displacements of the contact and target nodes, projected onto the local XY plane. By incrementally summing these tangential displacements across all sub-steps, the cumulative sliding distance of each node was determined. The sliding distances of all corner nodes belonging to a given contact element were averaged to obtain a representative sliding distance for that element. This provided a clear and continuous spatial distribution of micromotion across the entire bone–implant interface.

4.2.2.4 Contact Status definition

Based on the micromotion algorithm, the contact status was analysed with consideration of the gap value. Several threshold and classification criteria reported in previous computational models are summarised in Table 3.1. According to thresholds reported in experimental mechanobiology studies [208], micromotion exceeding 150 μm can lead to fibrous tissue differentiation, which is the first step toward AL. Osseointegration occurred when micromotion between the bone and implant was below 40 μm. The ingrowth was considered unsuccessful if the gap exceeded 500 μm. Accordingly, in this study, the contact status at the interface was

determined as Gap (Gap > 500 μm); for the interface with a gap less than 500 μm, the contact status was Bonded (Sliding < 40 μm); Standard (Sliding 40-150 μm); Risky (Sliding >150 μm) (Table 4.3).

An automated classification procedure developed in Ansys Mechanical APDL (Ansys release 2023 R2, ANSYS, Inc., Pennsylvania, USA) and MATLAB (Version R2022a, MathWorks, Inc., Natick, Massachusetts, USA), integrated with the micromotion algorithm, was implemented to ensure consistency across all simulations. This finally yielded reliable contact status results at the bone–implant interface, which were subsequently visualised in 3D mapping.

Table 4.3 Contact status definition according to the micromotion thresholds at the bone-implant interface.

Contact Status	Threshold
Gap	Gap > 500 μm
Risky	Sliding >150 μm
Standard	Sliding 40-150 μm
Bonded	Sliding < 40 μm

4.3 Result

4.3.1 Mesh convergence

As shown in Figure 4.7, the maximum contact sliding increased from 0.54 mm in S0 to 0.66 mm in S4, with the most pronounced change occurring between S0 and S2. Beyond S2, variations in contact sliding were less than 2%, indicating that the displacement solution had stabilised. Similarly, the SED results (Figure 4.6) showed minimal variation across all mesh densities, remaining within ±2% of the mean value.

Considering both accuracy and computational cost, S3 (element size: 1.5 mm) was selected for subsequent simulations. This mesh provided a sufficiently refined resolution to ensure stable displacement and SED responses while maintaining feasible computation times for the full set of loading conditions.

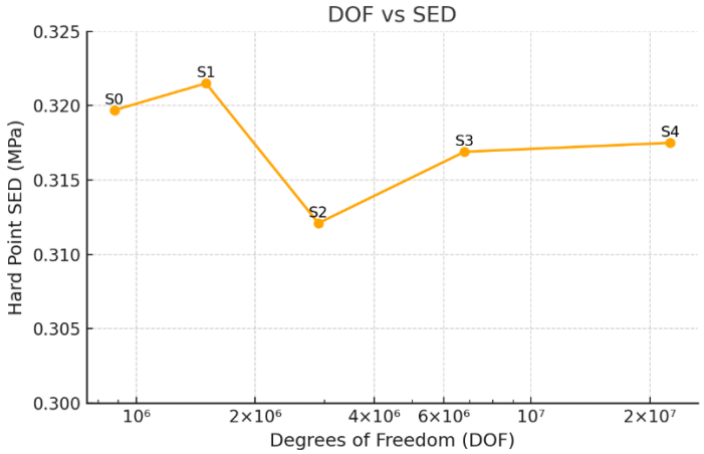

Figure 4.6 Mesh convergence analysis: models' degree of freedom with respect to the strain energy density (SED) at the hard point. Hard point was located by the position of the node corresponding to the highest SED in the coarsest mesh (3 mm); to ensure a node exists at the same spatial coordinate in all other refined meshes.

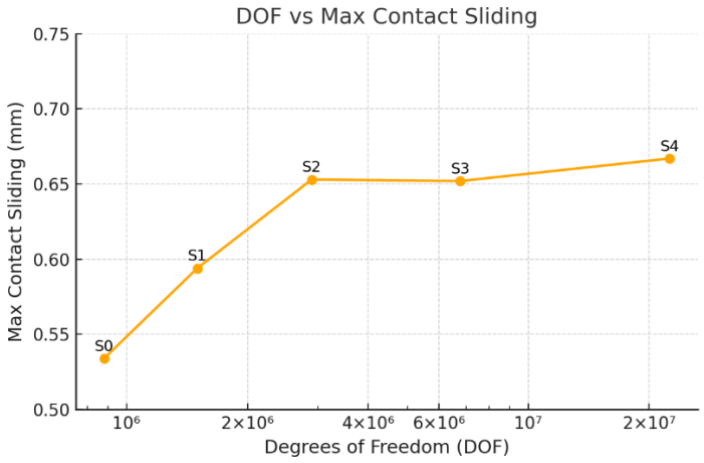

Figure 4.7 Mesh convergence analysis: models' degree of freedom with respect to the maximum contact sliding distance at the bone-implant interface.

4.3.2 Contact analysis results

Using the workflow of the patient- and surgery-specific FE model, a representative case study from the dataset was executed under stair climbing and level walking, applying loads corresponding to 70 kg body weight. The relative micromotion at each node on the bone–implant contact surface was calculated and then mapped to the results of contact status. The results of contact status statistics under stair climbing and level walking are summarised in Table 4.4. Each contact status area fraction of the whole contact area at the bone–implant interface was computed.

Results indicated that 9% of the contact area exhibited a gap greater than 500 μm in both loading cases. Under stair climbing, 16% of the contact area experienced sliding exceeding 150 μm, which was slightly higher compared to level walking. No bonded contact status was observed during stair climbing, whereas 2% of the contact area was bonded during level walking.

The spatial distribution of the relative sliding distance at the bone–implant interface is shown in Figure 4.8 for stair climbing and Figure 4.9 for level walking. The average sliding distance was 135 μm during stair climbing and 111 μm during level walking, with both maximum values located at the distal end of the femoral stem.

The overall distribution of contact status is illustrated in Figure 4.10 (stair climbing) and Figure 4.11 (level walking). Plots from both the coronal (anterior and posterior) and sagittal planes (lateral and medial) are presented. Regions of higher sliding were predominantly located at the distal end of the stem, with the lateral side exhibiting more pronounced motion compared to the medial side.

Table 4.4 Contact status results under stair climbing and level walking, area fraction (%) of contact-status categories (gap; risky; standard and bonded) at the bone–implant interface.

Contact Status	Under stair climbing area fraction (%)	Under level walking area fraction (%)
Gap	9	9
Risky	16	12
Standard	75	77
Bonded	0	2

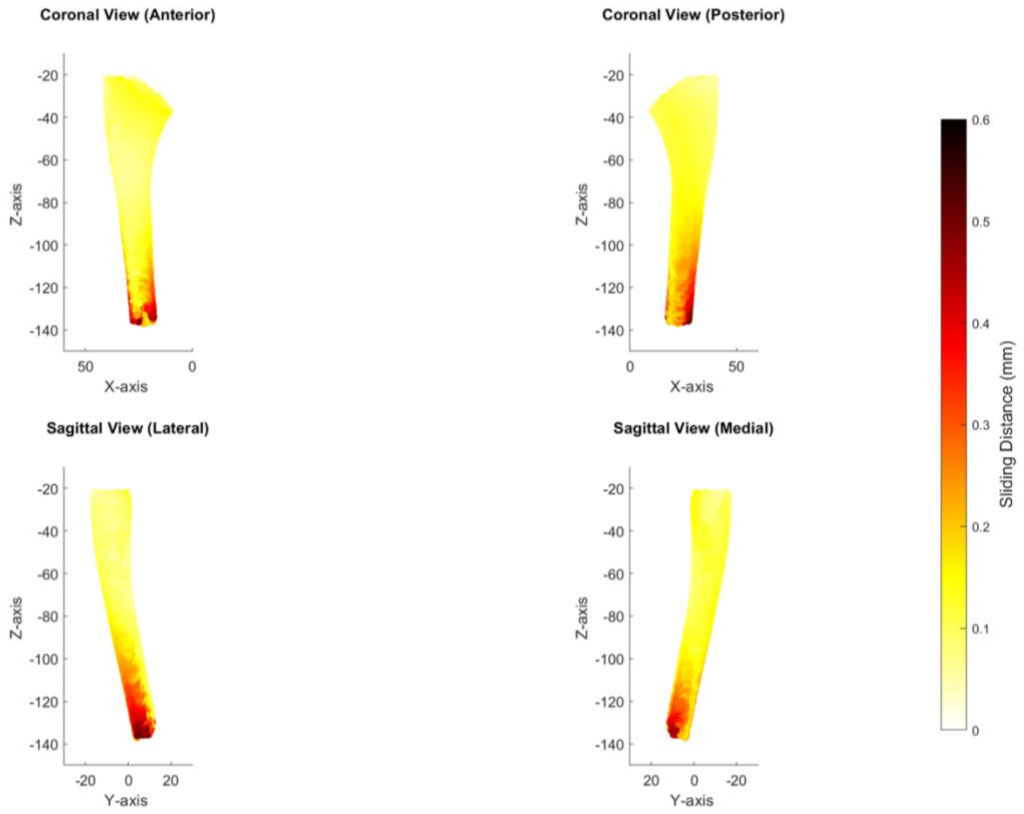

Figure 4.8. Under stair climbing, spatial map of contact relative sliding distance at the bone–implant interface.

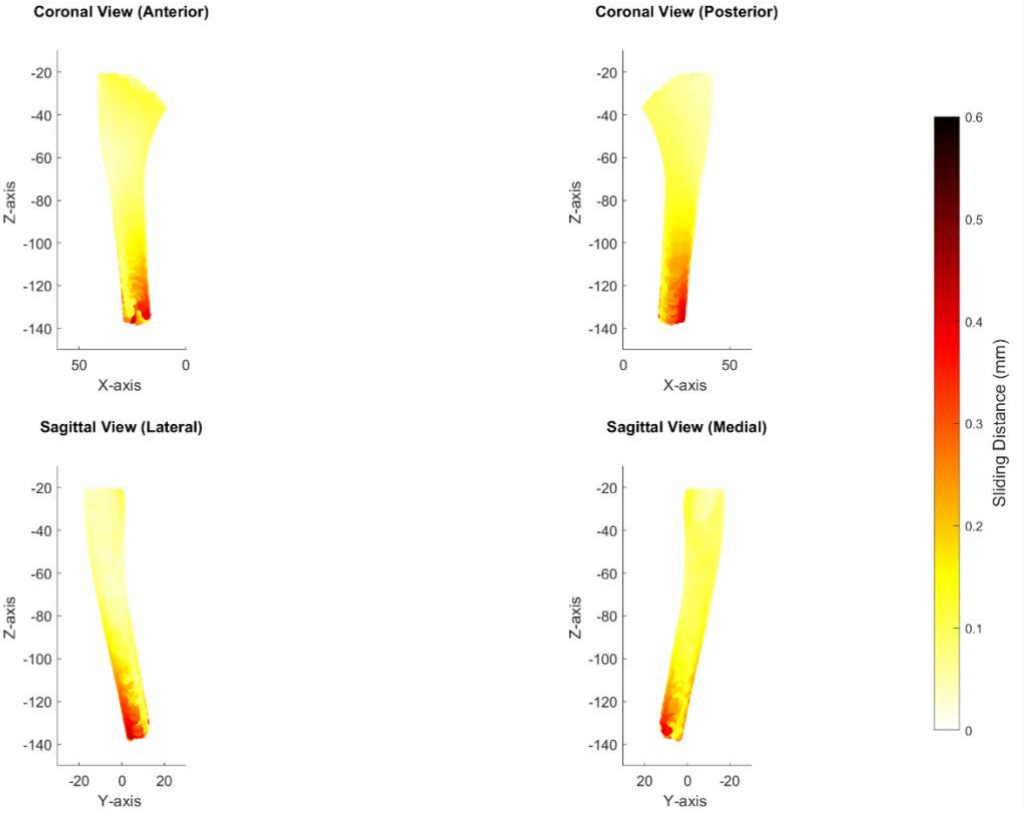

Figure 4.9. Under level walking, spatial map of contact relative sliding distance at the bone–implant interface.

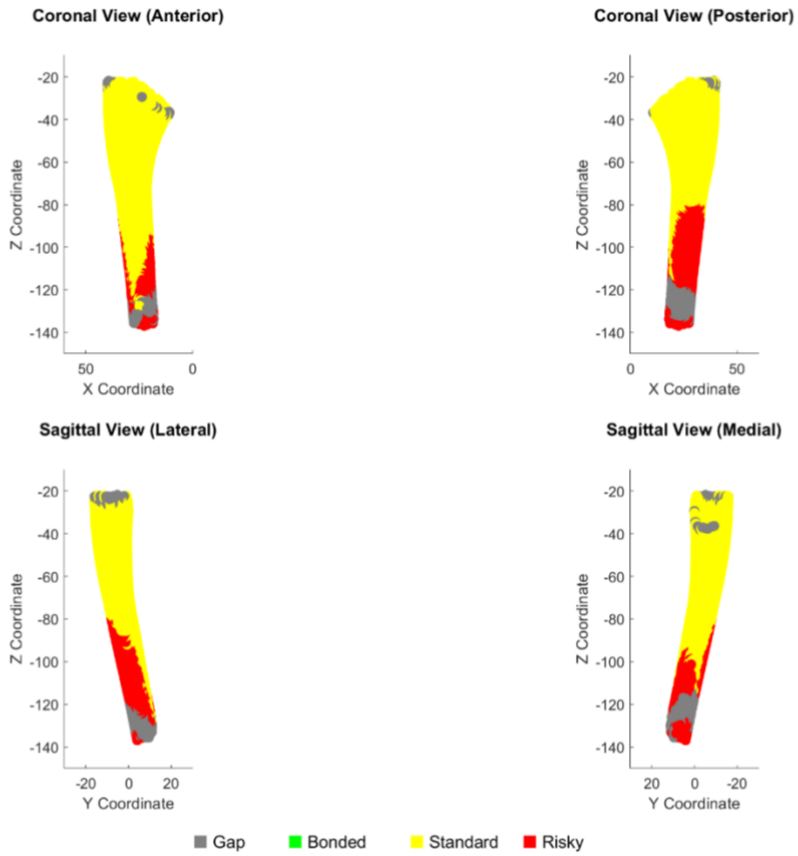

Figure 4.10. Under stair climbing, spatial map of contact states at the bone–implant interface.

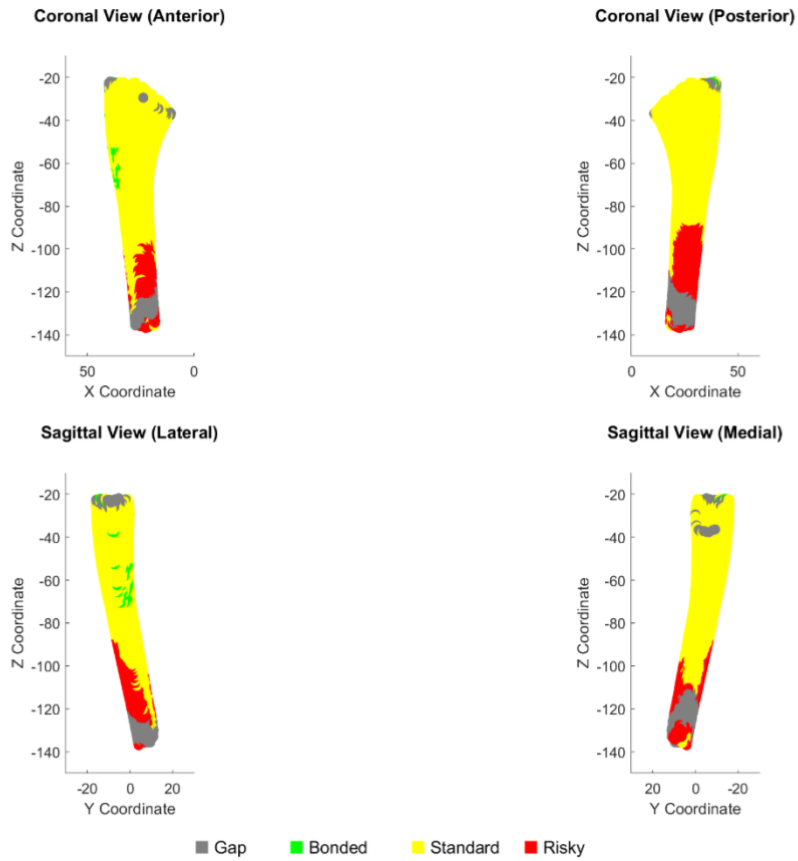

Figure 4.11. Under level walking, spatial map of contact states at the bone–implant interface.

4.4 Discussion

The aim of this thesis is to develop an *in silico* trial to estimate the risk of aseptic loosening (AL) in a new hip stem design. *In silico medicine* has gained broad acceptance for its ability to reduce experimental cost while enhancing the feasibility of clinical trials. Particularly in the field of orthopaedic devices, large-scale clinical trials can provide valuable insights into overall surgical outcomes, including implant designs, patient baseline and the surgical technologies. However, it remains difficult to distinguish the contribution of specific factors influencing these outcomes. This challenge highlights the necessity of close collaboration with clinicians and the implementation of a standardised, traceable pipeline that interprets clinical data for computational simulation.

This chapter presents a patient-specific and surgery-specific computational workflow for predicting the *primary stability* of a cementless anatomical femoral stem. Within this workflow, virtual preoperative surgical planning is performed by the surgeon, with software providing anatomical measurements of the femur and flexible pose adjustments of the implant to obtain accurate bone/implant relative position and resection planes. Subsequently, the FE contact analysis is coupled with user subroutines in Python/MATLAB for parameterised contact area selection, accurate micromotion quantification and customised contact state definition. The whole computation workflow enables the generation of interface micromotion maps and contact status distributions at the bone–implant interface under given daily activities. It will improve the predictive fidelity and efficiency of FE models to support preclinical evaluation of the cementless femoral stem.

Under stair climbing and level walking, the contact analysis was conducted in a case study. The results showed higher sliding distance concentrated near the distal stem, while a small lateral “bonded” region appeared only during level walking, but not during stair climbing. From the biomechanical point of view, these patterns suggest that everyday activities with higher joint loads and torsion may suppress early bone–implant bonding and enlarge regions prone to fibrous differentiation, thereby elevating late failure risk. This is in line with some clinical reports that patients engaging in high activity level loads are informed of their increased risk for AL [220]. The lateral bonded area observed in level walking indicates the localised conditions favourable to osseointegration, highlighting how activity profiles can modulate micromotion-driven risk.

In both loading conditions, a substantial portion of the stem surface may be susceptible to fibrous differentiation in the current case. Considering AL is a multifactor phenomenon, it can be caused by preoperative, intraoperative, and post-operative conditions, including (i) preoperative patient body weight, bone quality, femoral size; (ii) intraoperative implant sizing/positioning; and (iii) early postoperative activity intensity.

Therefore, the future work is extending the contact analysis to an *in silico trial* that involved a Monte Carlo study of the parameter space, sampling patients and surgical factors to quantify uncertainty in micromotion and the risky contact area fraction; a full-factorial sweep of all discrete combinations can be analysed. Based on the current workflow, the next chapter (Chapter 5) will explore the *primary stability* of the Apta stem as a

function of the femoral size, the subject's body weight, the pre-operative bone quality (degree of osteopenia), and the surgical uncertainty on the implant sizing.

Chapter 5

In silico trials to estimate the risk of aseptic loosening in new joint replacement designs: A Design of Experiments

5.1 Overview

In Chapter 4, we established a finite element (FE) model to quantify the risk of aseptic loosening in cementless femoral stems by computing the micromotion at the bone–implant interface. While single-patient analyses demonstrated the feasibility of the approach, the generalisation of these findings requires a systematic exploration of the effect of patient variability and surgical uncertainty.

In this chapter, a design of experiments (DoE) approach was employed to examine the influence of major factors on implant stability, as these factors represent the primary determinants of surgical success:

(1) Patient variability, represented by femoral size, bone quality and body weight (BW);
(2) Surgical uncertainty, represented by stem sizing and rotational misalignment.

By sampling representative combinations of these parameters, we generated a virtual patient cohort and conducted a set of 162 FE simulations across three patient-specific femur geometries, each tested under multiple body weight and bone mineral density (BMD)-derived T-score conditions, and with two stem sizes and 3 stem poses. The resulting micromotion patterns were analysed in terms of the risky contact area fraction, defined as the ratio of interface regions exceeding the micromotion threshold of 150 μm to the total bone–implant contact area. This DoE framework allows quantification of both patient-specific risk and generalisable patterns of failure, providing insights into the relative contributions of bone quality, loading, femoral geometry, and surgical variability.

5.2 Methods

To accurately assess aseptic loosening risk for a cementless stem, a virtual cohort was established that incorporates the diverse parameters influencing this failure mode. These parameters include anatomical morphology, bone quality, post-operative loading conditions, and surgical uncertainty.

5.2.1 Subject selection

Three femurs were selected from the HF valid database, corresponding to the minimum, average, and maximum femur size. The femoral size is defined as the estimated femoral biomechanical length: distance between the centre of the femur head and the midpoint of the knee condylar line, as it correlates strongly with

overall bone size and load-bearing capacity. The resulting models are referred to as Pat A (largest femur), Pat B (average femur), and Pat C (smallest femur), as shown in Table 5.1.

Table 5.1. Summary of demographics and femoral measurements for the selected patients; the implant stem size was suggested by the operating surgeon. Cases denote the patients with the maximum (A), average (B), and minimum (C) femoral size in the study cohort.

Subject	Age	Height	Weight	Side	Femur Length	T-score	Stem Size by surgeon
Pat A	76	168	100	R	413 mm	-2	Size 5
Pat B	72	154	90	R	370 mm	-2	Size 1
Pat C	77	134	55	R	312 mm	-2	Size1

5.2.2 Virtual patient cohort generation

In addition to femoral size, bone quality and patient body weight variability were also taken into account. We then scaled the bone quality and body weight.

Bone tissue was represented as a heterogeneous, linear elastic medium, with mechanical properties assigned on an element-by-element basis through Bonemat software (Istituto Ortopedico Rizzoli, Bologna, Italy). The local material parameters (ρ_{QCT}) were determined from the calibrated CT images of each subject [218] . Specifically, for every mesh element a volumetric bone mineral density (vBMD) was estimated by converting the corresponding Hounsfield Unit (HU) values using a linear calibration derived from phantom reference scans:

$$\rho_{QCT} = a + b*HU$$

where *HU* is the Hounsfield unit, and *a* and *b* are calibration coefficients obtained from phantom-based calibration scans. The coefficients a and b depended on the phantom calibration.

The relationship between density and stiffness followed a two-step conversion. First, ρ_{QCT} was transformed into ρ_{ash} ash density according to:

$$\rho_{ash}= 0.079 + 0.8772\cdot\rho_{QCT}$$

Apparent density was further converted into elastic modulus using established empirical relationships:

$$E = 14664 \cdot \rho_{ash}^{1.49}$$

Assuming the apparent density $\rho_{app}=\rho_{ash}/0.6$ and a constant Poisson's ratio.

To simulate the variations of bone quality, we independently scaled the bone mineral density of cortical and trabecular bone, which resulted in a total of nine virtual subjects. The baseline case corresponded to a T-score of -2, representing an osteopenia condition. It was further adjusted to represent both an osteoporotic state (T-score = -5) and a normal bone status (T-score = 0). Since bone remodelling in cortical bone occurs at a lower rate than in trabecular bone, the scaling of cortical and trabecular densities was carried out separately to account for their distinct biological behaviour.

To represent post-operative mechanical loading under different body weight conditions, hip joint reaction forces were scaled according to the patient's body weight. Three representative weights (50, 70, and 90 kg) were considered, corresponding to BMI values specific to each anatomical geometry. Loading scenarios for level walking and stair climbing were derived from validated musculoskeletal models and scaled linearly with body weight. Table 4.2 already summarises the applied loading cases, reporting hip forces both as a percentage of body weight (BW) and as absolute values referenced to 70 kg.

5.2.3 Surgical uncertainties

Previous Section 4.2.1 provided a detailed description of the virtual surgical planning performed with the Adler APTA cementless femoral stem. In this process, the implants were virtually positioned within the femoral models by the surgeon using the HiPlan software [215], a CT-assisted multimodality planning platform that enables accurate visualisation and alignment of the implant with the patient’s anatomy. In addition to the prosthetic components, corresponding rasp models were generated to reproduce the broaching procedure, shown in Fig.5.1. These rasp geometries were designed by incorporating internal grooves to mimic the cutting features of the surgical instrument, while a cylindrical extension was added at the proximal neck region to represent the clearance for the threaded connection of the insertion handle. Furthermore, a proximal enlarged section was created to simulate the compressive element produced during canal preparation, and the distal part of the rasp was elongated to match the overall length of the manufacturer’s CAD broach. This modelling strategy ensured that both the implant and its associated surgical tools were realistically represented, allowing a more faithful reproduction of the intraoperative preparation and insertion steps within the virtual environment.

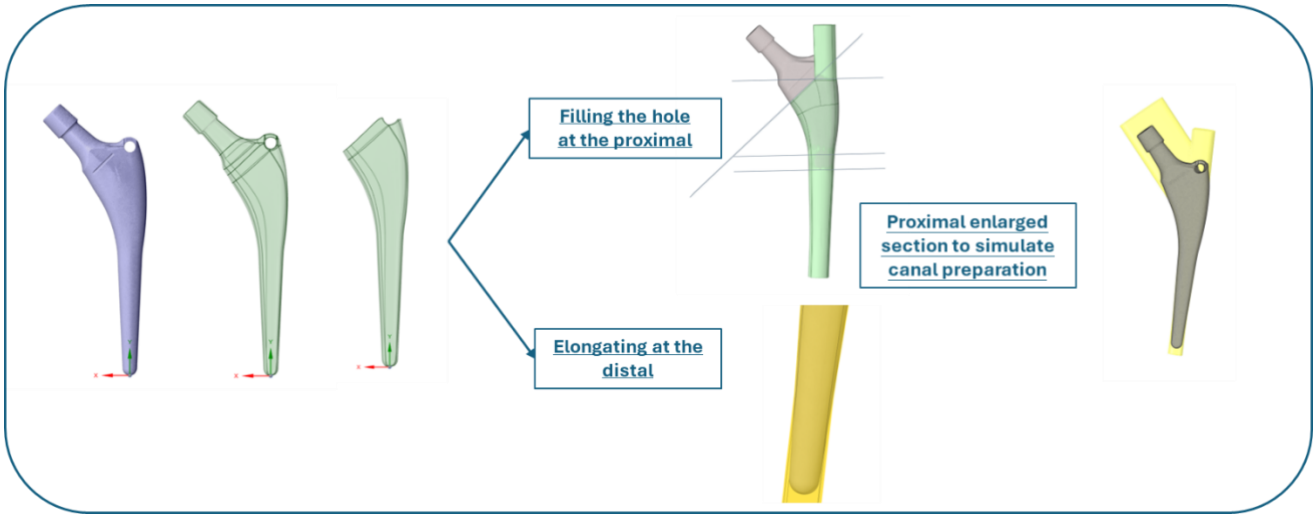

Figure 5.1. Procedure for constructing the rasp model from the femoral stem geometry, including proximal modification, canal preparation enlargement, and distal elongation.

Main surgical factors were introduced:

Stem sizing: For each patient, the planned stem size (as chosen by the surgeon) was compared with a stem size larger (+2), to assess the effect of under- vs. oversizing, under same cutting plane as shown in Fig. 5.2. While the primary stem was placed by the surgeon, the +2 size was positioned by the research engineer; the engineer used the surgeon's plan as a reference to maintain consistent proximal contact at the bone-implant interface. In this comparison, all stems belonged to the same design family (Adler APTA), in which the neck–shaft offset is constant across sizes. Therefore, varying the stem size did not alter the offset but only changed the overall length, width, and distal engagement of the implant within the femoral canal. Consequently, differences observed between the planned stem and the larger size (+2) reflect variations in canal fill and fixation rather than changes in offset.

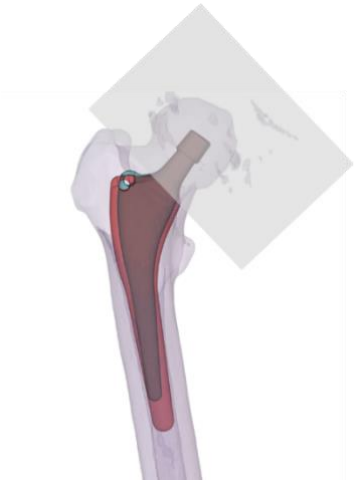

Figure 5.2. Illustration of two femoral stems virtually implanted within the same osteotomy plane: the stem size planned by the surgeon versus a larger stem (+2 sizes).

- **Resection plane:**

  Two cutting-plane configurations were considered. The first corresponded to the plane chosen by the surgeon in the virtual pre-operative planning, a user interface named HiPlan (mentioned in Chapter 4.2.1.1), representing the preferred osteotomy orientation according to the patient-specific femoral anatomy. The second was a theoretically prescribed plane, as might be recommended by the implant manufacturer, oriented perpendicular to the stem-neck axis (i.e., at 90° to the neck axis). In the simulations, both resection planes (Fig. 5.3) were applied and compared to evaluate the sensitivity of implant contact behaviour to variations in osteotomy orientation within an average-sized femur.

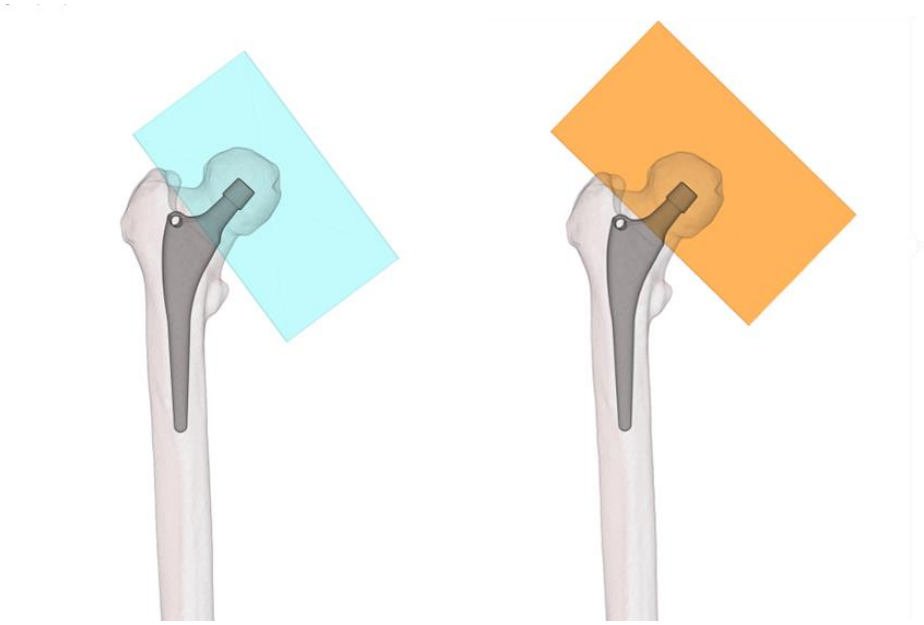

Figure 5.3. Comparison of two resection-plane configurations applied to the same femoral stem and pose within an average-sized femur. The blue plane corresponds to the surgeon's planned osteotomy orientation based on patient-specific anatomy, while the orange plane represents a theoretically prescribed manufacturer-style plane perpendicular (90°) to the stem–neck axis.

- **Rotational misalignment**: In clinical practice, it is virtually impossible to perform multiple real implantations on the same patient to directly quantify surgical error. Therefore, in this study we relied on evidence from virtual surgical planning, using it as a reasonable surrogate to represent the uncertainty in stem pose. Rotational misalignment was modelled within a range of −17° to +17°. This interval was derived from the work of Viceconti et al.[221], who systematically evaluated the spatial accuracy of pre-operative planning for total hip arthroplasty under different CT visualization modalities. Their results showed that rotational errors strongly depended on the display interface: deviations reached up to 16.7° with conventional 3D rendering, while even the orthogonal slice-based approach exhibited errors of around 4°. In contrast, the multimodal display interface significantly improved accuracy, reducing rotational error to less than 1°. These findings indicate that, even with

modern planning and navigation tools, femoral stem anteversion may be subject to uncertainties on the order of 10–15°. Based on this evidence, we adopted a conservative range of −17° to +17° in our simulations, to reproduce the rotational variability reported in clinical planning studies and thereby more realistically capture the effect of surgical uncertainty on implant stability. If the ±17° rotation range resulted in any part of the stem exceeding the cortical boundary of the host femur, the maximum allowable internal or external rotation that maintained cortical containment was applied instead.

5.2.4 Design of Experiments (DoE)

The factorial design included:

- 3 patients (small, average, large femur)
- 3 T-scores (0, −2, −5)
- 3 body weights (50, 70, 90 kg)
- 2 stem sizes (planned, +2)
- 3 stem poses (external 17°, planned, internal 17°)

This resulted in 162 simulations, the outcomes of which are presented as heatmaps to visualize the dependency of implant stability on bone quality, body weight, and stem size.

5. 3 Results

5.3.1 Effect of body weight and T-score on micromotion in average-sized femur

Based on the FE model of average-sized femur and stem (Subject B; femur length = 370 mm; stem size = 1), we performed a 3×2 factorial design varying body weight (50, 70, 90 kg) and bone quality (T-score = 0, −2) under two activities: level walking (LW) and stair climbing (SC). For each combination, the risky contact area fraction (micromotion > 150 μm) at the bone–implant interface was computed. Fig.5.4 visualises these results as heatmaps, with rows corresponding to T-score levels and columns to body weight for LW and SC, respectively.

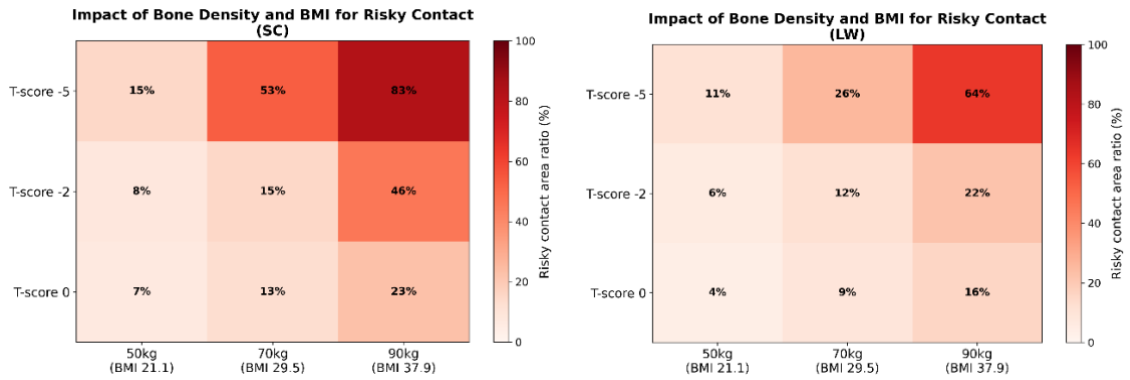

Figure 5.4. Heatmap of the risky contact area fraction at the bone–implant interface for the average-sized femur/stem under stair climbing (SC) or level walking (LW). Rows vary bone quality (T-score = 0, -2, -5); columns vary body weight (50, 70, 90 kg). Warmer colours denote larger risky area. Risky contact area fraction defined as the ratio of the bone–implant interface area with micromotion > 150 μm to the total bone–implant contact area.

5.3.2 Effect of stem pose on micromotion in an average-sized femur

The influence of stem rotational alignment on primary stability was assessed in the average-sized femur. As summarised in Table 5.2, externally rotating the stem by 17° and 10° resulted in relatively lower micromotions (159 and 160 μm) and smaller risky regions (38% and 39%). Near-neutral positions, including the planned orientation and ±3° rotations, produced slightly higher micromotions (170–173 μm) with approximately 45% of the interface classified as at risk. Further internal rotation to 10° and 17° increased micromotion values to 174 and 179 μm, while the risky area decreased modestly to 43% and 40%, respectively. Overall, these findings suggest that extreme external rotation may reduce micromotion, whereas internal rotation beyond 10° tends to increase it, with only minor variations observed in the proportion of the risky contact area.

Table 5.2. Influence of stem rotational pose on average micromotion and percentage of risky contact area for the average-sized femur.

Stem pose rotated	External 17°	External 10°	External 3°	Surgeon Planned	Internal 3°	Internal 10°	Internal 17°
Risky area (%)	38	39	45	45	45	43	40
Average micromotion (μm)	159	160	170	173	170	174	179

5.3.3 Effect of osteotomy (surgeon's cut vs guided cut) in an average-sized femur

The influence of osteotomy orientation was investigated in an average-sized femur by comparing two cutting planes under stair climbing. The first section, defined according to the surgeon's cut (Osteotomy 1), resulted in an average relative sliding of 173 µm and a risk region of 46% (Fig. 5.5). The second section (Osteotomy 2), guided by the specifications provided by the commercial stem manufacturer, yielded an average sliding of 176 µm with 48% of the interface identified as at risk (Fig. 5.6).

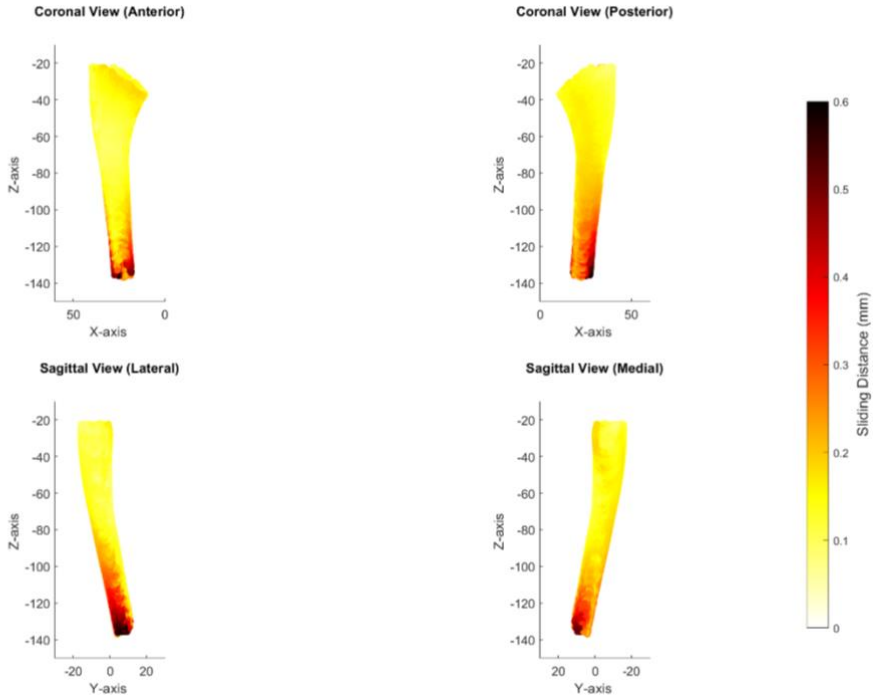

Figure 5.5. Contact sliding distance mapping for Osteotomy 1. Spatial distribution of relative sliding distance at the bone–implant interface for Osteotomy 1 (surgeon-defined plane) under stair-climbing loading conditions.

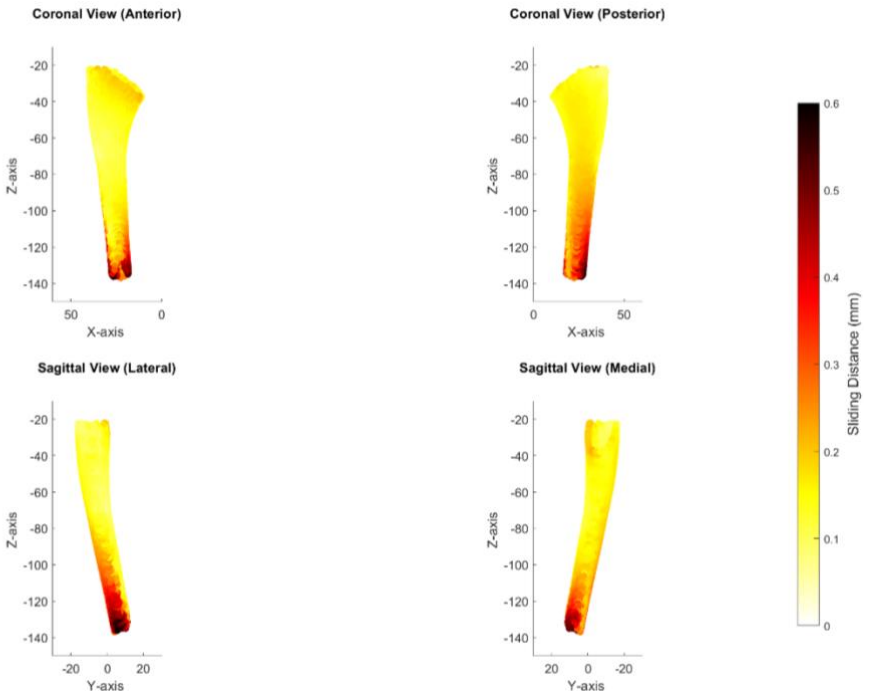

Figure 5.6. Contact sliding distance mapping for Osteotomy 2. Spatial distribution of relative sliding distance at the bone–implant interface for Osteotomy 2 (manufacturer-guided plane) under stair-climbing loading conditions.

5.3.4 Effect of Stem size on micromotion in three patient-specific models

For each patient, in addition to the planned stem size, simulations were conducted with a stem two sizes larger (+2 size) to account for implant size variability. The influence of stem size on micromotion, in relation to patient-specific body weight and T-score, is summarised in Table 5.3. Results are presented together with the change in risk (Δ Risky %). For Patient A, with a planned size 5 stem, upsizing to size 7 markedly reduced the risky region from 93% to 49% (Δ −44%). Similarly, Patient B showed a substantial reduction from 46% to 21% when the stem size was increased from size 1 to size 3 (Δ −25%). In contrast, Patient C exhibited a negligible change, with the risky fraction slightly increasing from 8% to 9% (+1%).

Table 5.3. Risky contact area fraction results of patient-specific FE model with different stem size (planned stem size vs pulsed stem size). Risky contact area fraction defined as the ratio of the bone–implant interface area with micromotion > 150 μm to the total bone–implant contact area.

Subject	Planned Stem Size	Stem Size Plus	Risky% (Planned)	Risky% (Size plus)	Δ Risky %
Pat A	Size5	Size7	93	49	- 44
Pat B	Size1	Size3	46	21	- 25
Pat C	Size1	Size3	8	9	+ 1

5.3.3 Effect of Femur size and implant stem size on micromotion with patient-specific weight and T-score

To examine the role of femoral geometry, micromotion at the bone–implant interface was evaluated in three representative patients, corresponding to the maximum, minimum, and average femoral sizes, with the stem sizes originally planned by the surgeon. The resulting risky contact area fractions are reported in Table 5.4 as a function of patient-specific body weight and T-score. Substantial variability was observed depending on stem size and body weight. Patient A, implanted with a size 5 stem and weighing 100 kg, exhibited the highest risk, with 93% of the interface identified as unstable. Patient B, with a smaller anatomy (size 1 stem) and a body weight of 90 kg, showed a markedly reduced risk of 46%. In contrast, Patient C, also implanted with a size 1 stem but with a much lower body weight of 55 kg, displayed only 8% of risky interface. Thirty percents bonded contact region was detected at the proximal part of the stem–bone interface in Patient C (Fig.5.7).

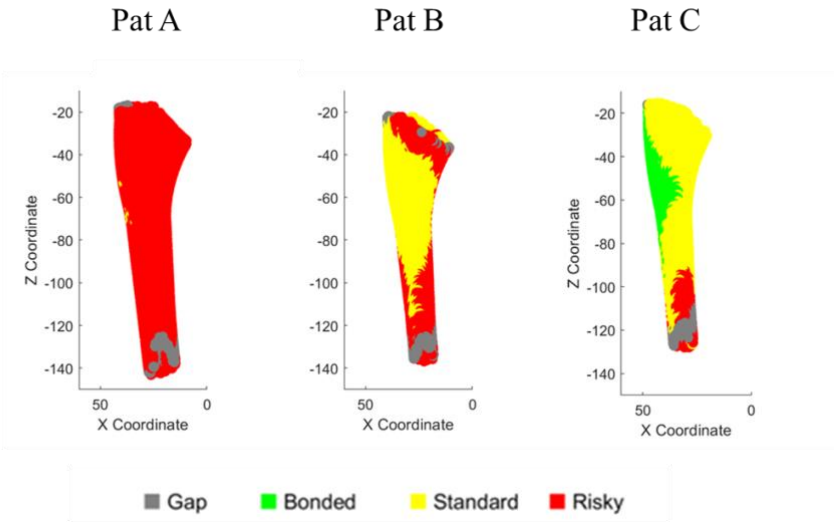

Figure 5.7. Contact condition maps at the bone–implant interface for three representative patients (Pat A, Pat B, Pat C) under stair-climbing. Colours indicate gap (grey), bonded (green), standard (yellow), and risky (red) regions.

Table 5.4. Risky contact area fraction results of patient-specific body weight and T-score. Risky contact area fraction defined as the ratio of the bone–implant interface area with micromotion > 150 μm to the total bone–implant contact area.

Subject	Femoral Stem Size	Body weight	T-score	Risky %
Pat A	Size 5	100	-2	93%
Pat B	Size 1	90	-2	46%
Pat C	Size 1	55	-2	8%

5.4 DoE: effect of parameter combination

Building upon the findings of previous single-factor investigations, a comprehensive Design of Experiments (DoE) framework was employed to quantify the combined influence of femur size, stem size, implant pose, bone quality (T-score), and body weight on implant stability metrics. As preliminary analyses revealed that osteotomy orientation (cutting plane) had a slight effect on micromotion at the bone implant interface, all DoE simulations were conducted using the surgeon-defined osteotomy plane for consistency.

As illustrated in Fig.5.8, the heatmaps display the predicted risk levels associated with micromotion at the implant–bone interface, under varying conditions of patient morphology, stem size, and surgical pose deviations. The three simulated poses—internal rotation, planned, and external rotation—were introduced to reflect possible angular deviations during surgery, representing typical uncertainties rather than intentional variations in surgical approach. Each subplot corresponds to a unique combination of patient anatomy (Pat A, B, or C), stem size, and pose, while the annotated values denote the percentage of risky interfacial area across different bone quality (T-score) and body mass index (BMI) conditions.

This set of heatmaps emphasises the critical influence of surgical variability—even within the bounds of realistic intraoperative error—on implant stability. The results indicate that the planned pose, which reflects the surgeon's intended pose for the stem, does not always yield the lowest risk. In several configurations, notably in Pat A with stem size 5, small rotational deviations from the planned pose can lead to marked increases in risk, with values reaching up to 94% in patients with low bone density and high BMI. In contrast, Pat C under internal rotational poses showed generally lower micromotion risk across both stem sizes. However, this trend was not uniform across all subjects. For Pat B, larger stem sizes under external rotation were linked to widespread regions of elevated risk, whereas smaller stems under similar external deviation showed a reduction in risky contact area.

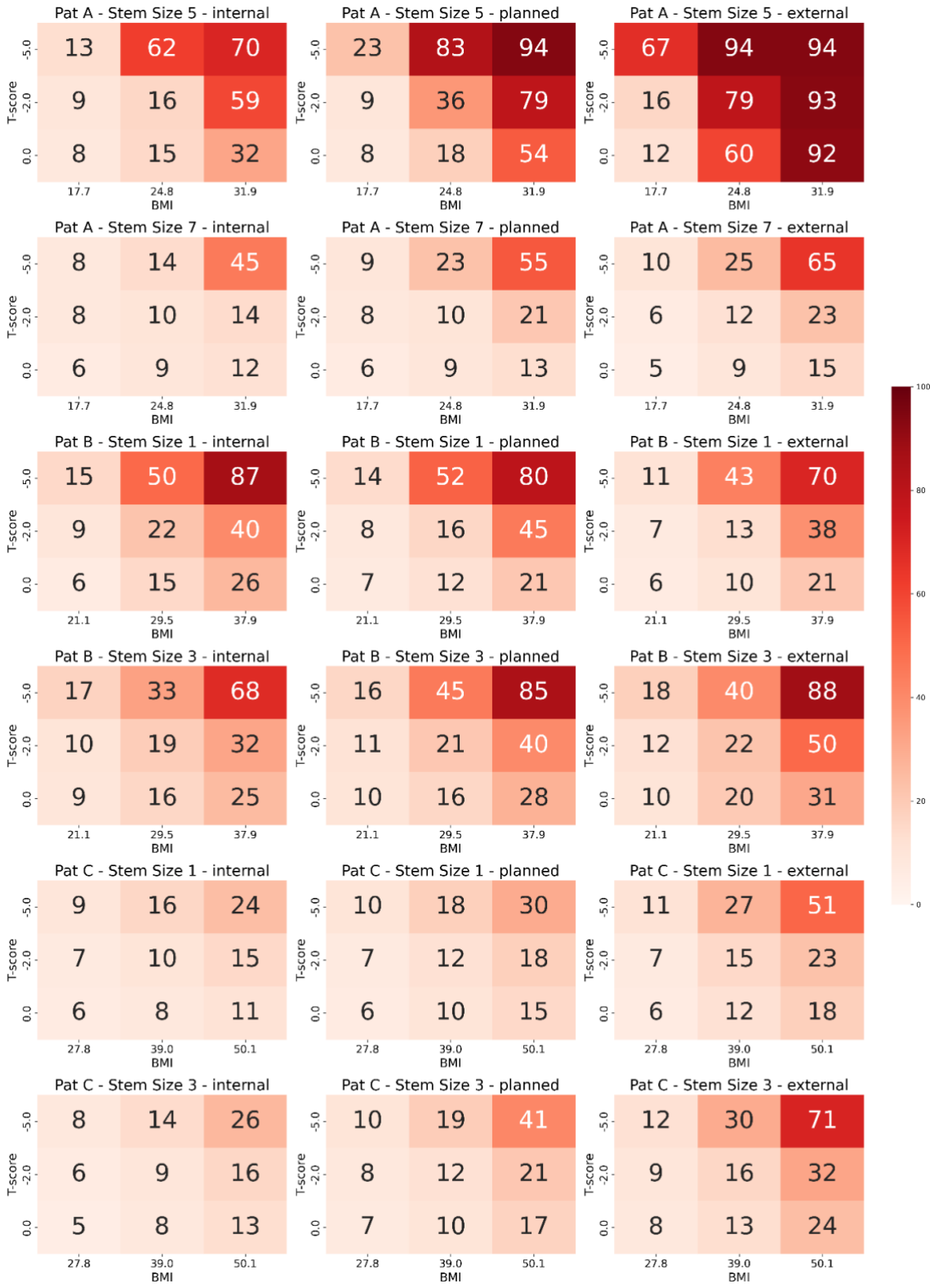

Figure 5.8. Heatmaps of predicted implant loosening risk (%) across varying T-score and BMI combinations, stratified by patient (Pat A–C), stem size, and surgical pose (internal rotation, planned, external rotation). Each subplot represents one unique combination of patient-specific femoral anatomy, implant size, and alignment condition. Risk values are shown as percentages, with darker colours indicating a higher risk of loosening. The "planned" pose (centre column) corresponds to the surgical plan, while the "internal" rotation and "external" rotation poses simulate rotational misalignment. T-score reflects bone quality, and BMI represents body weight relative to height.

The highest predicted risk area was consistently observed in regions of low T-score and high BMI, across all patient-stem-pose configurations. We stratified the dataset based on patient-specific physiological conditions. The Compromised Physiology Group included patients with a T-score ≤ −3 and body weight ≥ 80 kg. The Normal Physiology Group consisted of those with a T-score ≥ −2 and a body weight of < 80 kg. As shown in Fig. 5.9, a significant difference in risk area percent at the bone–implant interface was observed between the two groups ($p < 0.0001$). The femur size showed a significant influence on the risk assessment ($p < 0.05$) as shown in Fig.5.10. Specifically, the largest femur (Pat A) demonstrated a significantly higher predicted risk compared with the smallest femur (Pat C), and a difference was also observed between Pat B and Pat C ($p < 0.05$).

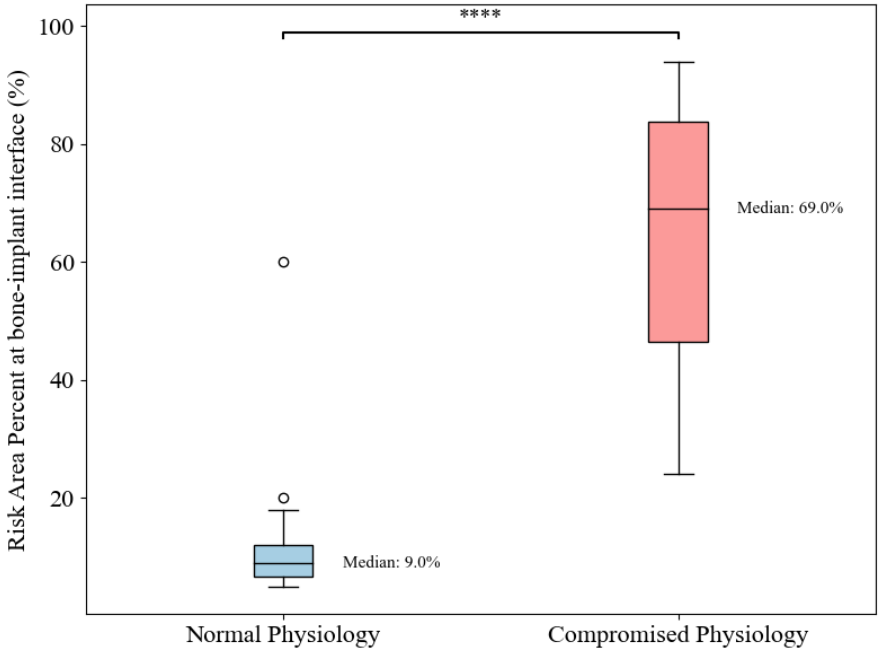

Figure 5.9. Distribution of predicted risk area percent at the bone–implant interface, stratified by physiological condition. Patients with T-score ≤ –3 and body weight ≥ 80 kg (Compromised Physiology) showed significantly higher risk area percentages compared to those with T-score ≥ –2 and body weight < 80 kg (Normal Physiology). Median values are labelled beside each box.

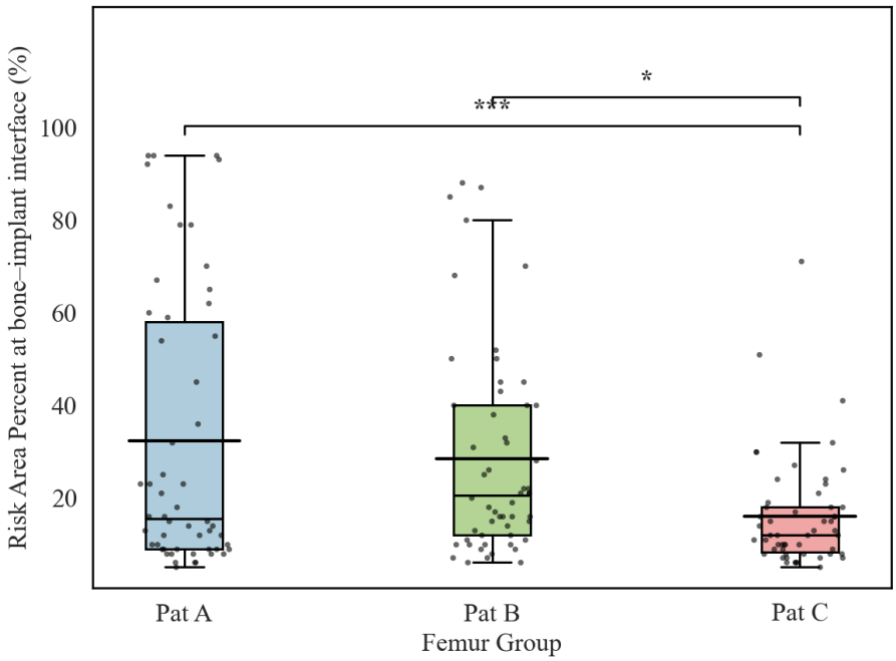

Figure 5.10. Effect of femur size on predicted interface risk. Boxplots illustrate the distribution of the predicted risk area percentage at the bone–implant interface for three representative femoral sizes (Pat A, Pat B, and Pat C), 54 models for each femur.

5.5 Discussion

This study applied a Design of Experiments (DoE) framework to systematically investigate how patient variability and surgical uncertainty influence the primary stability of cementless femoral stems. Through 162 simulations covering combinations of femoral geometry, bone quality, body weight, stem sizing, and rotational alignment, we quantified how each factor—and their interactions—affects micromotion at the bone–implant interface, an established predictor of aseptic loosening.

Among all parameters, bone quality and body weight emerged as two dominant patient-related factors. Variations in T-score had a pronounced effect on micromotion, with higher bone density consistently reducing the proportion of risky contact area. This result confirms the well-documented influence of bone stiffness on the mechanical interlock between implant and host bone. However, the analysis also showed that the detrimental effect of low T-score could be partially mitigated when the implant achieved good canal filling or was optimally aligned, suggesting that surgical precision may compensate for compromised bone conditions to some extent. Body weight, on the other hand, directly scaled the magnitude of joint reaction forces and led to nearly proportional increases in micromotion. Under stair-climbing loads, heavier patients exhibited markedly higher sliding and larger risky contact regions, while lighter patients maintained better initial stability.

These findings reinforce clinical evidence that excessive mechanical loading is one of the primary causes of early loosening and underline the need for weight management and postoperative load control, especially in osteoporotic individuals.

Regarding surgical factors, stem size demonstrated the most substantial stabilising effect. Increasing the stem size significantly reduced the micromotion and risky area in large and medium femurs, as the larger stem improved press-fit and cortical contact. In contrast, for the smallest femur, oversizing produced negligible improvement, implying that when cortical support is limited, further enlargement of the stem provides diminishing mechanical benefit and may even risk cortical perforation. But it should be noted that the stem size will also affect other risks such as bone fracture and stress shielding. Rotational alignment also influenced stability, though to a smaller degree. Slight external rotations of about 10–17° reduced micromotion by improving engagement of the posterior cortical wall, whereas internal rotations beyond 10° increased motion and shear. In contrast, deviations within ±3° around the planned orientation caused only minor differences, suggesting a moderate tolerance range in surgical practice. The influence of osteotomy orientation was comparatively minor. The difference between the surgeon-defined plane and the manufacturer-guided plane remained within 3% of risky area variation, indicating that cutting-plane orientation exerts a secondary influence compared to other surgical parameters. Nonetheless, consistent osteotomy execution remains necessary to ensure reproducible implant seating and neck geometry.

When the combined and interactive effects of parameters were examined, the relationships proved to be nonlinear rather than purely additive. The interaction between bone quality and body weight was particularly evident: in osteoporotic bone, even moderate increases in body weight led to disproportionately higher micromotion, indicating that poor bone amplifies load sensitivity. Conversely, normal bone quality effectively buffered the impact of weight variation. Similarly, the benefit of stem oversizing was found to depend strongly on femoral geometry. The stability related to the micromotion for large femurs benefited greatly from upsizing because of enhanced cortical engagement, whereas small femurs showed little change. These findings are consistent with current patient-specific implant planning practices, highlighting the importance of accounting for individual canal morphology rather than applying a uniform sizing rule. Another important interaction was observed between bone quality and stem alignment. In low-density bone, even small rotational errors resulted in larger regions of interface slip, whereas the same misalignment in dense bone produced negligible change. Together, these findings demonstrate that surgical precision becomes increasingly critical when bone quality deteriorates and that patient variability amplifies the mechanical consequence of operative uncertainty.

From a clinical and design standpoint, the DoE results provide several insights. Proper stem sizing and accurate rotational control appear to be the most effective strategies for minimising early micromotion, especially in patients with reduced bone density. While the surgeon cannot alter intrinsic bone quality, careful preoperative planning and intraoperative adjustment can substantially improve fixation outcomes. Conversely, patient-related factors such as high body weight and severe osteoporosis remain difficult to compensate for surgically,

highlighting the importance of preoperative assessment and postoperative rehabilitation in reducing mechanical risk. From an implant design perspective, the results indicate that optimising proximal canal engagement and enhancing surface coatings that promote bone ingrowth may be more beneficial than simply altering stem geometry or neck orientation. Computational DoE analysis, as demonstrated here, provides a reproducible and quantitative framework to guide both design iteration and clinical decision-making.

Several limitations of the present work should be acknowledged. First, the analysis was conducted on a limited number of femoral geometries (three specimens), which may not fully capture the complete anatomical variability observed in the clinical population. Nevertheless, these geometries were selected to represent distinct canal morphologies, allowing the investigation of geometry-dependent trends rather than patient-specific predictions. Second, only hip contact force was applied, no muscle forces were considered. Thirdly, the present study does not include direct validation against benchtop experiments or clinical outcomes for the investigated stem design. As such, the findings should be interpreted as mechanistic and hypothesis-generating rather than predictive of individual clinical performance. However, the observed trends are consistent with previously reported experimental and clinical observations in the literature regarding the influence of femoral geometry and cortical engagement on stem stability, providing indirect support for the credibility of the results.

Despite these limitations, this thesis offers several novel contributions beyond existing studies. In contrast to prior works that focused on isolated patient-specific analyses, the present framework enables systematic, population-level in-silico investigations through automated geometry processing, meshing, and material mapping. This approach allows the quantitative assessment of geometry-dependent implant behaviour under controlled variations in patient variability and surgical uncertainty, providing a scalable foundation for future virtual clinical trials and experimental validation.

Chapter 6

Towards in silico trials to estimate the risk of aseptic loosening in new joint replacement designs

One of the major challenges in predicting the risk of aseptic loosening in orthopaedic implants lies in the difficulty of accurately reproducing surgical variability. In real clinical settings, it is impossible to perform multiple surgeries on the same patient or to achieve perfectly identical implantations across different individuals. However, these limitations can be overcome in *in silico* simulations, where the surgical and patient-specific parameters can be systematically varied under controlled conditions.

In this context, *in silico clinical trials* provide a powerful preclinical tool to define individualised surgical implantation and conduct large-scale virtual cohort studies. Through computational modelling, it becomes possible to incorporate a wide range of factors that influence implant stability—such as bone quality, body weight, skeletal morphology, implant design, stem size, implant pose, and even post-operative loading conditions or lifestyle patterns. By parametrically varying these variables across a virtual population, the model can be validated from a population-level perspective. For high-risk complications—particularly aseptic loosening of cementless hip stems—this approach holds substantial clinical relevance to support personalised preoperative risk assessment and optimise implant designs accordingly.

In this thesis, we explored the effect of inter-patient and inter-surgery variability on the primary stability of a cementless stem using a Design of Experiment (DOE) approach. This gave us the possibility to carefully develop and validate the modelling methods, and to get a first sense of what the most important factors governing the mechanical stability of the stem are. The natural evolution of this study would be to generalise the methods for any cementless stem design, and to run a full Monte Carlo analysis instead of the DOE one. Both steps require the development of a fully automated pipeline, which can take in input the geometry of any cementless stem, and generate hundreds of simulations predicting the primary stability for a variety of patients described by their different femur sizes, bone densitometry, and body weight, when operated with the typical surgical variability regarding stem size and pose within the femur.

The automated computational framework developed in this work bridges the gap between biomechanical modelling and clinical decision-making. By automating the methods established in Chapters 4 and 5, we enable large-scale data processing, probabilistic modelling, and population-based risk evaluation, transforming traditional single-case finite element analysis into a scalable, reproducible system for virtual clinical experimentation.

6.1 Toward a Monte Carlo study: automating the pipeline

Automating the pipeline for generating and running Finite Element Analysis (FEA) for orthopaedic prostheses involves a structured workflow that aligns with traditional FEA practices but enhances enable the systematicity of calculations.

This approach enables the system to process data in batches when dealing with large volumes of patient-specific or surgery-specific inputs, thereby significantly reducing the operator time and thus the costs associated with a full-scale Monte Carlo analysis. With more efficient FEAs of this automation methodology, medical device optimisation or personalised preoperative surgery planning will benefit. In previous chapters, we detail each step of this workflow: Geometry of bone and implants, Virtual implantation, Mesh generation, Material properties assignment, Boundary conditions and solutions. This chapter will discuss the application of the automatic pipeline. The script was run on PowerShell associated with Python programming to launch the software of ANSYS 2023R2 (Mechanical APDL, Space Claim, ICE CDF, and BoneMat).

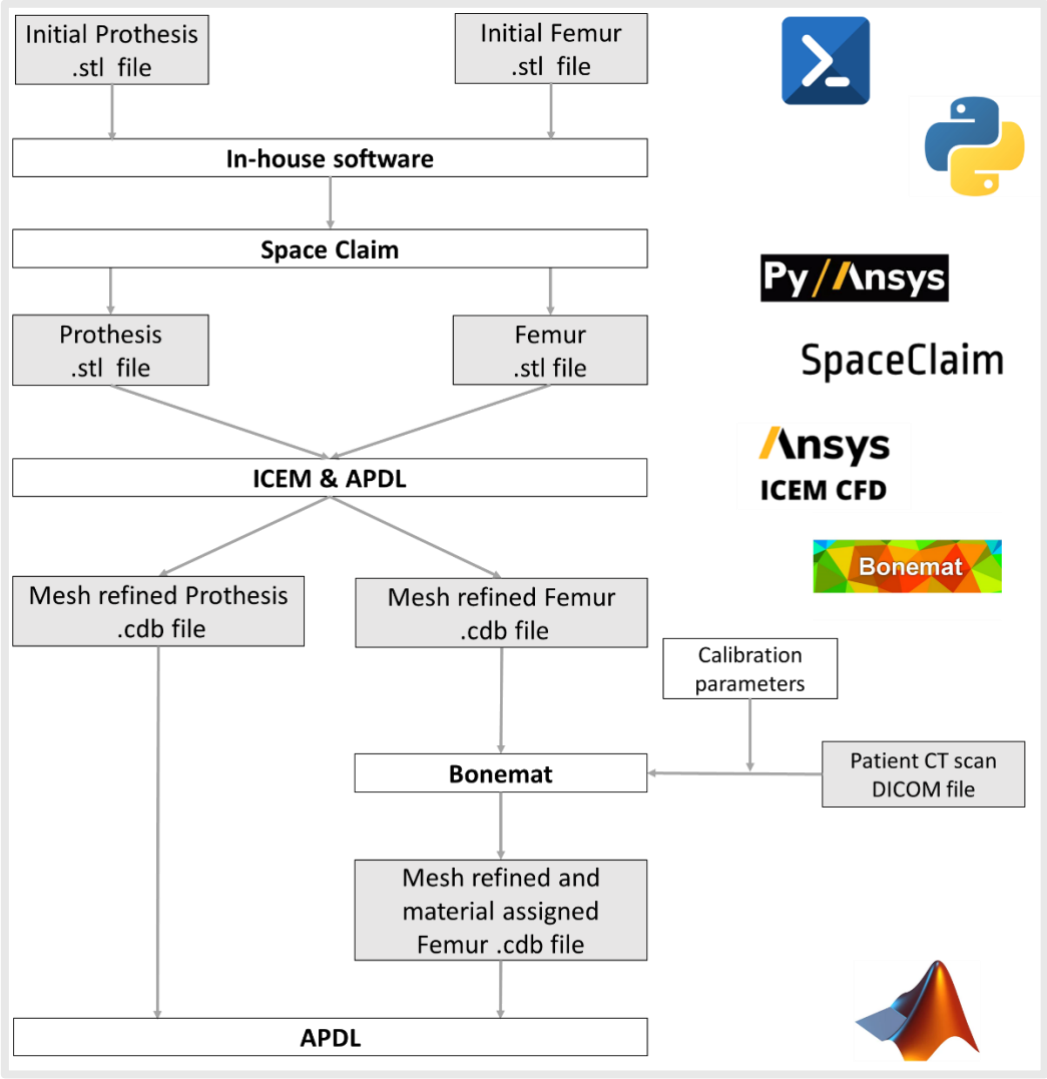

Figure 6.1. Automatic pipeline of patients -specific Finite Element Analysis for orthopaedic device in total hip joint replacement.

SpaceClaim provides Python-based scripting support, allowing sequential import of anatomical and implant geometries, followed by Boolean subtraction operations (e.g., *bone – cutting plane)* to create assembled models. Each processed geometry is automatically saved to a designated directory, as illustrated in *Figure 6.2*. It can also apply a rotation matrix to simulate variations in implant pose through scripting support. In Chapter 5, the meshing and material mapping information were detailed; both meshing and material mapping procedures were executed automatically using pre-defined Python, ICEM, and APDL macros. ICEM was employed exclusively as a meshing tool. The mesh density and element type were controlled according to anatomical regions, while Bonemat scripts assigned heterogeneous material properties based on calibrated relationships between CT grey values and elastic moduli.

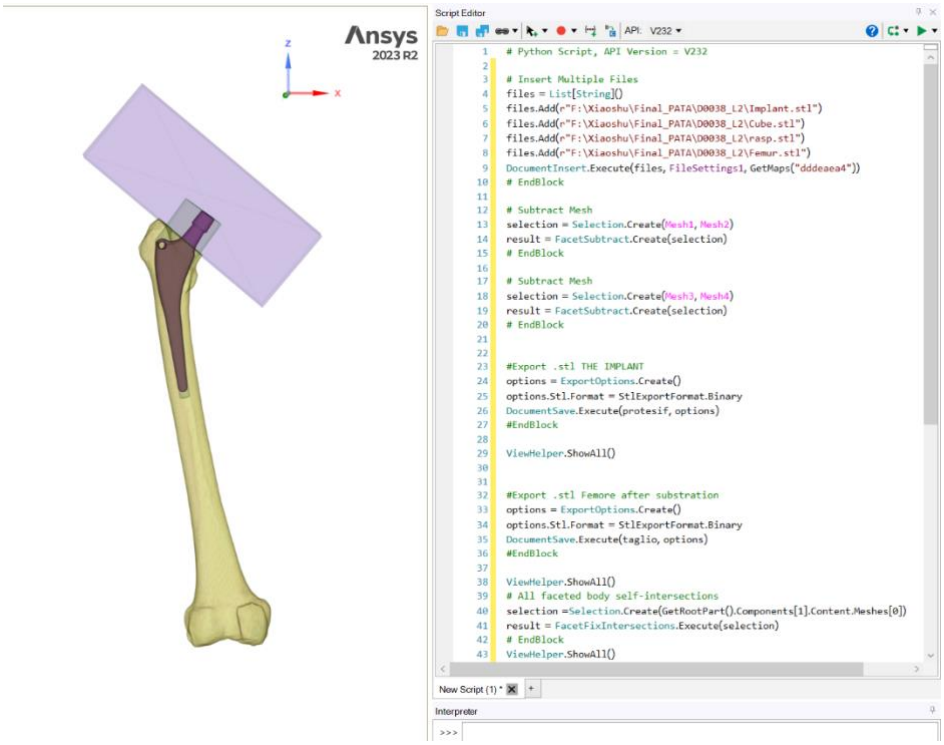

Figure 6.2. Example of a Python-based automation script in ANSYS SpaceClaim 2023 R2, illustrating the transition from manual Boolean operations to a fully automated workflow for virtual implantation and geometry preparation.

To be specific, for each virtual surgical plan done by the surgeon, the PowerShell interface allows the user to interactively specify the working directory, output path, and patient identifier. These identifiers link to individualised parameters such as anatomical landmark coordinates, DICOM datasets, and material calibration coefficients. Once initialised, the script launches ANSYS Mechanical APDL in batch mode, performs the full simulation, and saves the post-processing results automatically. A demonstration of this execution interface is presented in *Figure 6.3*.

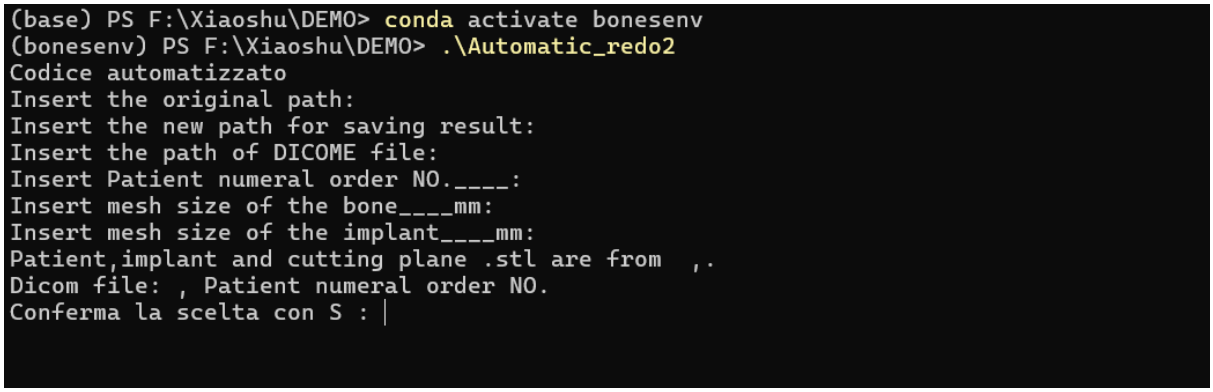

Figure 6.3. Interactive execution interface of the fully automated script, demonstrating the workflow initialisation within a configured Conda environment. In this demonstration, the automation framework is launched through a PowerShell terminal after activating the predefined Python environment (bonesenv). The user is prompted to specify the input and output directories, the DICOM file path, the patient identifier, and the mesh resolutions for both bone and implant models. Mesh size was chosen based on the mesh sensitivity analysis. Once these parameters are confirmed, the pipeline automatically executes the sequence of geometry processing, meshing, material mapping, and FEA simulation steps.

Based on the main automation workflow, a batch-processing system was implemented to automatically generate, execute, and post-process multiple finite-element simulations corresponding to the design-of-experiments (DoE) combinations. As illustrated in Figure 6.5, the PowerShell script sequentially called ANSYS MAPDL for each parameter set — here represented by variations in body weight (50 kg, 70 kg, 90 kg) and T-score (0, -2, -5) — while maintaining the same boundary conditions associated with stair-climbing load cases. This approach enabled the automated generation of all virtual models and the direct computation of post-processing metrics, such as the proportion of high-micromotion regions (> 150 μm) obtained from contact analyses. The results from these serial tests were later aggregated and visualised as risk-distribution heatmaps, providing a quantitative assessment of implant stability across physiological and bone-quality variations.

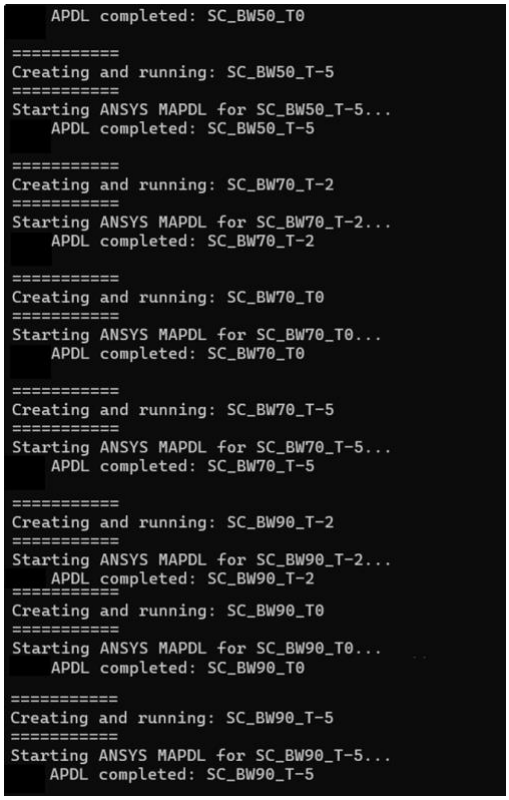

Figure 6.4 Example of automated batch simulation execution in PowerShell, showing sequential ANSYS MAPDL runs for combinations of body weight and T-score under stair-climbing loading conditions.

All simulations were performed in batch mode by the same operator using ANSYS 2023R2 (Mechanical APDL, Space Claim, ICE CDF, and BoneMat). Each model required approximately 120 minutes of wall-clock time, consisting of 2-3 minutes for preprocessing geometry, meshing, and material properties, 100 minutes for solution convergence, and 15 minutes for postprocessing and data export. In total, nine DoE combinations were processed sequentially within approximately 18 hours of computing time. The results of these test series were then summarized and visualized as risk distribution heatmaps, providing quantitative case study evidence of implant stability across physiological and bone quality variations.

In summary, to ensure the framework can be replicated, the master control is handled by a PowerShell script that manages the data flow between the Python environment and the ANSYS suite. This script initializes by activating a configured Conda environment named "bonesenv" and prompts the user for critical path definitions, including the DICOM dataset location and the specific patient identifier. The automation relies on a directory-linked system where anatomical landmarks and material calibration coefficients are automatically pulled based on the patient ID. By launching ANSYS Mechanical APDL in batch mode, the system bypasses manual graphical interface errors, ensuring that every simulation in a large-scale cohort—such as those required for Monte Carlo analysis—is executed under identical, controlled conditions.

Furthermore, the geometric preparation and material assignment stages utilize a specific sequence of Python and APDL macros to maintain consistency. In SpaceClaim, Python scripts automate Boolean operations, such as subtracting the cutting plane from the bone mesh, to create the virtual implantation assembly. The material mapping process, conducted via Bonemat, establishes a direct link between CT grey values and the elastic moduli assigned to the heterogeneous bone mesh. For replication purposes, it is noted that while mesh sizes are user-specified at the start of the pipeline, they are strictly governed by previous mesh sensitivity analyses to ensure solution convergence. This standardized approach allows for a total processing time of approximately 120 minutes per model, with the majority of the time dedicated to solution convergence, thus providing a clear computational benchmark for future studies.

6.2 Toward a Monte Carlo of primary stability prediction in cementless femoral stems

Each simulation was characterised by a combination of patient-specific and surgical parameters that collectively describe inter-subject variability and procedural uncertainty. The model included five main input variables: femur geometry (V1), body weight (V2), T-score (V3), stem size (V4), and stem pose (V5).

The femur geometry represents the anatomical variability among subjects and was approximated using three discrete models—small (S), medium (M), and large (L)—corresponding to the three patients analysed in this study. Although, in principle, such variability should ideally be represented through a statistical shape model or anatomical atlas [222], in this first approximation, it was assumed that the femoral geometry could take only these three representative configurations. Body weight and bone quality (expressed by the T-score) were treated as continuous stochastic variables sampled from literature-based probability distributions. Specifically, body weight followed a truncated Gaussian distribution (mean = 69.2 kg; range = 50–120 kg, truncated at 2% on both ends [223]), which better reflects the realistic population distribution and avoids non-physical values. The T-score was modelled as a truncated Gaussian with a mean of -2.5 and zero probability outside the [0, -5] interval.

The surgical variability was captured through stem size and stem pose. The stem pose was parameterised by angular orientations—internal/external rotation. For each femur geometry, the planned surgical configuration served as the central reference, around which all variables were varied according to their defined probability ranges.

A Monte Carlo analysis was then performed using a Latin Hypercube Sampling (LHS) strategy [224]. Successive batches of 100 simulations were performed until the mean and standard deviation of the outcome metrics (e.g., interface micromotion area > 150 μm) converged to stable values.

Probability distributions:

V1 – Femur Geometry: three discrete values (S, M, L) with flat probability.

V2 – Body Weight: truncated Gaussian distribution, mean = 69.2 kg, range = 50–120 kg, truncated at 2% [223].

V3 – T-score: truncated Gaussian, mean = −2.5, 18% probability at 0 and −5, according to the probability for an osteoporosis patient in THA [225] .

V4 – Stem Size: Gaussian distribution centred on the planned size, with variation up to ±2 sizes [226].

V5 – Stem Pose: Gaussian distribution centred on the planned alignment, with limits defined by surgical feasibility and the intra-cortical boundary of the host femur. External -internal rotation maximum 17° [221].

Samples were drawn according to the Latin Hypercube algorithm:

i. Generate an initial set of 100 samples and run the simulations.
ii. Increase the sample size to 200 and re-evaluate the mean and standard deviation of the target quantities (e.g., % area > 150 µm).
iii. Continue adding batches of 100 simulations until convergence of both the mean and the standard deviation is observed.

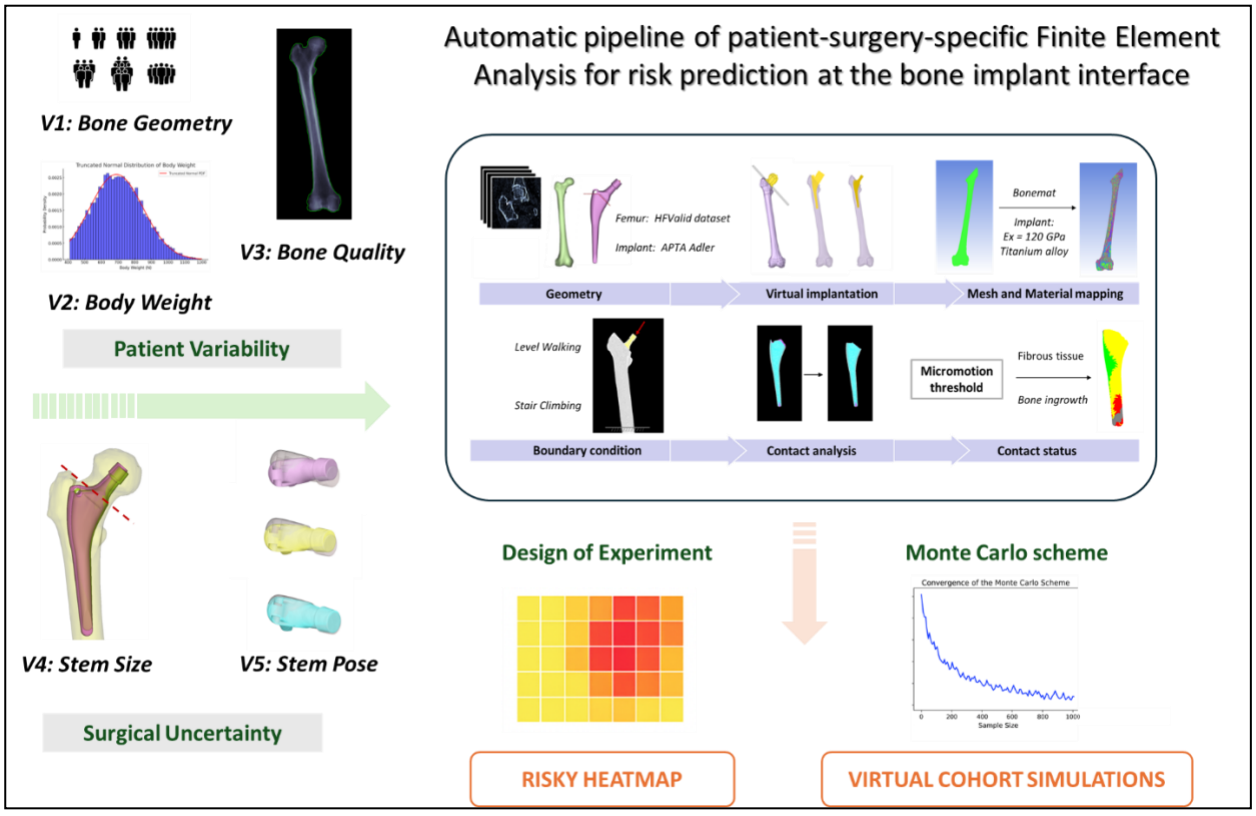

Figure 6.5. Overview of the automated simulation framework integrating patient variability and surgical uncertainty in finite element analyses of hip stem stability. This schematic illustrates the complete workflow developed to quantify the influence of both patient variability and surgical uncertainty on the mechanical stability of cementless femoral stems. On the left, patient variability is represented by differences in femoral geometry, body weight distribution, and bone quality (T-score), while surgical uncertainty includes variations in stem size and pose during implantation. The automated finite element pipeline (centre) consists of sequential steps: geometry preparation, virtual implantation, meshing and material property mapping, boundary condition assignment, and contact analysis. Each simulation computes interface micromotion to evaluate contact stability between bone and implant.

As the number of Monte Carlo iterations will be increasing, the mean and standard deviation of the predicted interface micromotion will be gradually stabilised, indicating the convergence of the virtual cohort. The final converged value will be representing a statistically robust estimate of the implant's primary stability, integrating both patient variability and surgical uncertainty. This value will be directly comparable with the corresponding data from clinical cohorts, thereby establishing a quantitative bridge between computational predictions (*in silico trial*) and real-world clinical outcomes (*clinical trial*). Such an approach enables the construction of a statistically representative in silico population, where the variability in anatomy, bone quality, and surgical technique is systematically sampled. The resulting virtual cohort provides a reproducible and ethically sustainable framework to complement clinical studies, supporting evidence-based evaluation of implant fixation and guiding future optimisation of orthopaedic device design.

References

[1] C. A. Petersilge, 'From the RSNA Refresher Courses. Radiological Society of North America. Chronic adult hip pain: MR arthrography of the hip', *Radiographics*, vol. 20 Spec No, pp. S43-52, Oct. 2000, doi: 10.1148/radiographics.20.suppl_1.g00oc12s43.

[2] M. Daniel, A. Iglič, and V. Kralj-Iglič, 'The shape of acetabular cartilage optimizes hip contact stress distribution', *J Anat*, vol. 207, no. 1, pp. 85–91, Jul. 2005, doi: 10.1111/j.1469-7580.2005.00425.x.

[3] D. E. Lunn, A. Lampropoulos, and T. D. Stewart, 'Basic biomechanics of the hip', *Orthopaedics and Trauma*, vol. 30, no. 3, pp. 239–246, Jun. 2016, doi: 10.1016/j.mporth.2016.04.014.

[4] R. Galmiche, H. Migaud, and P.-E. Beaulé, 'Hip Anatomy and Biomechanics Relevant to Hip Replacement', in *Personalized Hip and Knee Joint Replacement*, C. Rivière and P.-A. Vendittoli, Eds., Cham (CH): Springer, 2020. Accessed: Jul. 31, 2025. [Online]. Available: http://www.ncbi.nlm.nih.gov/books/NBK565771/

[5] R. Layton, N. Messenger, and T. Stewart, 'Characteristics of hip joint reaction forces during a range of activities', *Medical Engineering & Physics*, vol. 108, p. 103894, Oct. 2022, doi: 10.1016/j.medengphy.2022.103894.

[6] G. Bergmann *et al.*, 'Hip contact forces and gait patterns from routine activities', *J Biomech*, vol. 34, no. 7, pp. 859–871, Jul. 2001, doi: 10.1016/s0021-9290(01)00040-9.

[7] M. A. Varacallo, T. D. Luo, and N. A. Johanson, 'Total Hip Arthroplasty Techniques', in *StatPearls*, Treasure Island (FL): StatPearls Publishing, 2025. Accessed: Jul. 24, 2025. [Online]. Available: http://www.ncbi.nlm.nih.gov/books/NBK507864/

[8] J. N. Katz, K. R. Arant, and R. F. Loeser, 'Diagnosis and treatment of hip and knee osteoarthritis: A review', *JAMA*, vol. 325, no. 6, pp. 568–578, Feb. 2021, doi: 10.1001/jama.2020.22171.

[9] N. Aresti, J. Kassam, N. Nicholas, and P. Achan, 'Hip osteoarthritis', Jul. 2016, doi: 10.1136/bmj.i3405.

[10] H. Long *et al.*, 'Prevalence Trends of Site-Specific Osteoarthritis From 1990 to 2019: Findings From the Global Burden of Disease Study 2019', *Arthritis & Rheumatology*, vol. 74, no. 7, pp. 1172–1183, 2022, doi: 10.1002/art.42089.

[11] L. E. Diamond *et al.*, 'Individuals with mild-to-moderate hip osteoarthritis walk with lower hip joint contact forces despite higher levels of muscle co-contraction compared to healthy individuals', *Osteoarthritis and Cartilage*, vol. 28, no. 7, pp. 924–931, Jul. 2020, doi: 10.1016/j.joca.2020.04.008.

[12] C. A. G. Meyer *et al.*, 'Hip movement pathomechanics of patients with hip osteoarthritis aim at reducing hip joint loading on the osteoarthritic side', *Gait Posture*, vol. 59, pp. 11–17, Jan. 2018, doi: 10.1016/j.gaitpost.2017.09.020.

[13] C. A. G. Meyer *et al.*, 'Evaluation of stair motion contributes to new insights into hip osteoarthritis-related motion pathomechanics', *Journal of Orthopaedic Research*, vol. 34, no. 2, pp. 187–196, 2016, doi: 10.1002/jor.22990.

[14] J. A. López-López *et al.*, 'Choice of implant combinations in total hip replacement: systematic review and network meta-analysis', *BMJ*, vol. 359, p. j4651, Nov. 2017, doi: 10.1136/bmj.j4651.

[15] A. A. Khalifa and H. M. Bakr, 'Updates in biomaterials of bearing surfaces in total hip arthroplasty', *Arthroplasty*, vol. 3, no. 1, p. 32, Nov. 2021, doi: 10.1186/s42836-021-00092-6.

[16] U. F. O. Themes, 'Uncemented Tapered Femoral Components', Musculoskeletal Key. Accessed: Aug. 04, 2025. [Online]. Available: https://musculoskeletalkey.com/uncemented-tapered-femoral-components/

[17] A. Di Martino *et al.*, 'Long-term survival and complication rate of cementless prosthetic stems in primary total hip arthroplasty categorized by types according to Mont classification: a regional registry-based study on 53,626 implants', *Arch Orthop Trauma Surg*, vol. 144, no. 3, pp. 1423–1435, Mar. 2024, doi: 10.1007/s00402-023-05144-x.

[18] H. S. Khanuja, J. J. Vakil, M. S. Goddard, and M. A. Mont, 'Cementless Femoral Fixation in Total Hip Arthroplasty', *JBJS*, vol. 93, no. 5, p. 500, Mar. 2011, doi: 10.2106/JBJS.J.00774.

[19] J. Charnley, 'Arthroplasty of the hip. A new operation', *Lancet*, vol. 1, no. 7187, pp. 1129–1132, May 1961, doi: 10.1016/s0140-6736(61)92063-3.

[20] C. A. Engh and R. H. Hopper, 'The odyssey of porous-coated fixation', *The Journal of Arthroplasty*, vol. 17, no. 4, Supplement 1, pp. 102–107, Jun. 2002, doi: 10.1054/arth.2002.32547.

[21] M. S. Lehil and K. J. Bozic, 'Trends in total hip arthroplasty implant utilization in the United States', *J Arthroplasty*, vol. 29, no. 10, pp. 1915–1918, Oct. 2014, doi: 10.1016/j.arth.2014.05.017.

[22] W. H. Harris and W. J. Maloney, 'Hybrid Total Hip Arthroplasty', *Clinical Orthopaedics and Related Research®*, vol. 249, p. 21, Dec. 1989.

[23] H. Wangen *et al.*, 'Reverse hybrid total hip arthroplasty', *Acta Orthop*, vol. 88, no. 3, pp. 248–254, Jun. 2017, doi: 10.1080/17453674.2016.1278345.

[24] J. R. McLaughlin and K. R. Lee, 'Total Hip Arthroplasty With an Uncemented Tapered Femoral Component in Patients Younger Than 50 Years of Age: A Minimum 20-Year Follow-Up Study', *The Journal of Arthroplasty*, vol. 31, no. 6, pp. 1275–1278, Jun. 2016, doi: 10.1016/j.arth.2015.12.026.

[25] X. Y. Mei, Y. J. Gong, O. Safir, A. Gross, and P. Kuzyk, 'Long-term outcomes of total hip arthroplasty in patients younger than 55 years: a systematic review of the contemporary literature', *Can J Surg*, vol. 62, no. 4, pp. 249–258, Aug. 2019, doi: 10.1503/cjs.013118.

[26] A.-K. Fowler, A. R. Gray, and D. P. Gwynne-Jones, 'Hybrid Fixation for Total Hip Arthroplasty Showed Improved Survival Over Cemented and Uncemented Fixation: A Single-Center Survival Analysis of 2156 Hips at 12-18 Years', *The Journal of Arthroplasty*, vol. 34, no. 11, pp. 2711–2717, Nov. 2019, doi: 10.1016/j.arth.2019.06.031.

[27] A. Abdulkarim, P. Ellanti, N. Motterlini, T. Fahey, and J. M. O'Byrne, 'Cemented versus uncemented fixation in total hip replacement: a systematic review and meta-analysis of randomized controlled trials', *Orthop Rev (Pavia)*, vol. 5, no. 1, p. e8, Feb. 2013, doi: 10.4081/or.2013.e8.

[28] H. S. Khanuja, K. L. Mekkawy, A. MacMahon, C. M. McDaniel, D. A. Allen, and J. T. Moskal, 'Revisiting Cemented Femoral Fixation in Hip Arthroplasty', *J Bone Joint Surg Am*, vol. 104, no. 11, pp. 1024–1033, Jun. 2022, doi: 10.2106/JBJS.21.00853.

[29] K. I. Bunyoz, E. Malchau, H. Malchau, and A. Troelsen, 'Has the Use of Fixation Techniques in THA Changed in This Decade? The Uncemented Paradox Revisited', *Clin Orthop Relat Res*, vol. 478, no. 4, pp. 697–704, Apr. 2020, doi: 10.1097/CORR.0000000000001117.

[30] O. Chechik, M. Khashan, R. Lador, M. Salai, and E. Amar, 'Surgical approach and prosthesis fixation in hip arthroplasty world wide', *Arch Orthop Trauma Surg*, vol. 133, no. 11, pp. 1595–1600, Nov. 2013, doi: 10.1007/s00402-013-1828-0.

[31] N. Patel and P. Golwala, 'Approaches for Total Hip Arthroplasty: A Systematic Review', *Cureus*, vol. 15, no. 2, p. e34829, doi: 10.7759/cureus.34829.

[32] M. Tjur, A. R. Pedersen, W. Sloth, K. Søballe, N. D. Lorenzen, and M. Stilling, 'Posterior or anterolateral approach in hip joint arthroplasty - Impact on frontal plane moment', *Clinical Biomechanics*, vol. 54, pp. 143–150, May 2018, doi: 10.1016/j.clinbiomech.2018.03.017.

[33] V. M. Moretti and Z. D. Post, 'Surgical Approaches for Total Hip Arthroplasty', *Indian J Orthop*, vol. 51, no. 4, pp. 368–376, 2017, doi: 10.4103/ortho.IJOrtho_317_16.

[34] A. C. Lepri, M. Villano, F. Matassi, C. Carulli, M. Innocenti, and R. Civinini, '"Anterolateral" approach to the hip: a systematic review of the correct definition of terms', *Hip Int*, vol. 30, no. 2_suppl, pp. 13–19, Dec. 2020, doi: 10.1177/1120700020966800.

[35] A. Lübbeke, A. J. Silman, C. Barea, D. Prieto-Alhambra, and A. J. Carr, 'Mapping existing hip and knee replacement registries in Europe', *Health Policy*, vol. 122, no. 5, pp. 548–557, May 2018, doi: 10.1016/j.healthpol.2018.03.010.

[36] 'International Survey of Primary and Revision Total Hip Replacement'.

[37] R. J. Ferguson, A. J. Palmer, A. Taylor, M. L. Porter, H. Malchau, and S. Glyn-Jones, 'Hip replacement', *The Lancet*, vol. 392, no. 10158, pp. 1662–1671, Nov. 2018, doi: 10.1016/S0140-6736(18)31777-X.

[38] J. A. Singh, 'Epidemiology of Knee and Hip Arthroplasty: A Systematic Review§', *TOORTHJ*, vol. 5, no. 1, pp. 80–85, Mar. 2011, doi: 10.2174/1874325001105010080.

[39] A. B. Pedersen, S. P. Johnsen, S. Overgaard, K. Søballe, H. T. Sørensen, and U. Lucht, 'Total hip arthroplasty in Denmark', *Acta Orthopaedica*, vol. 76, no. 2, pp. 182–189, Jan. 2005, doi: 10.1080/00016470510030553.

[40] T. Ingvarsson, G. Hägglund, H. Jónsson, and L. S. Lohmander, 'Incidence of total hip replacement for primary osteoarthrosis in Iceland 1982-1996', *Acta Orthop Scand*, vol. 70, no. 3, pp. 229–233, Jun. 1999, doi: 10.3109/17453679908997798.

[41] G. Hooper, A. J.-J. Lee, A. Rothwell, and C. Frampton, 'Current trends and projections in the utilisation rates of hip and knee replacement in New Zealand from 2001 to 2026', *N Z Med J*, vol. 127, no. 1401, pp. 82–93, Aug. 2014.

[42] S. Nemes, M. Gordon, C. Rogmark, and O. Rolfson, 'Projections of total hip replacement in Sweden from 2013 to 2030', *Acta Orthopaedica*, vol. 85, no. 3, pp. 238–243, Jun. 2014, doi: 10.3109/17453674.2014.913224.

[43] I. N. Ackerman *et al.*, 'The projected burden of primary total knee and hip replacement for osteoarthritis in Australia to the year 2030', *BMC Musculoskelet Disord*, vol. 20, no. 1, p. 90, Feb. 2019, doi: 10.1186/s12891-019-2411-9.

[44] M. Rupp, E. Lau, S. M. Kurtz, and V. Alt, 'Projections of Primary TKA and THA in Germany From 2016 Through 2040', *Clin Orthop Relat Res*, vol. 478, no. 7, pp. 1622–1633, Jul. 2020, doi: 10.1097/CORR.0000000000001214.

[45] J. A. Singh, S. Yu, L. Chen, and J. D. Cleveland, 'Rates of Total Joint Replacement in the United States: Future Projections to 2020–2040 Using the National Inpatient Sample', *The Journal of Rheumatology*, vol. 46, no. 9, pp. 1134–1140, Sep. 2019, doi: 10.3899/jrheum.170990.

[46] G. S. Matharu, A. Judge, D. W. Murray, and H. G. Pandit, 'Trabecular Metal Acetabular Components Reduce the Risk of Revision Following Primary Total Hip Arthroplasty: A Propensity Score Matched Study From the National Joint Registry for England and Wales', *The Journal of Arthroplasty*, vol. 33, no. 2, pp. 447–452, Feb. 2018, doi: 10.1016/j.arth.2017.08.036.

[47] W. Hoskins, S. Rainbird, C. Holder, S. E. Graves, and R. Bingham, 'Revision for Aseptic Loosening of Highly Porous Acetabular Components in Primary Total Hip Arthroplasty: An Analysis of 20,993 Total Hip Replacements', *The Journal of Arthroplasty*, vol. 37, no. 2, pp. 312–315, Feb. 2022, doi: 10.1016/j.arth.2021.10.011.

[48] A. Palomäki *et al.*, 'Implant Survival of 6,080 Tritanium Cups in Primary Total Hip Arthroplasty: Data from the Finnish Arthroplasty Register from 2009 to 2017', *JBJS*, vol. 102, no. 13, p. 1177, Jul. 2020, doi: 10.2106/JBJS.19.00874.

[49] M. Wagner, H. Schönthaler, F. Endstrasser, D. Dammerer, P. Nardelli, and A. Brunner, 'Mid-Term Results After 517 Primary Total Hip Arthroplasties With a Shortened and Shoulderless Double-Taper Press-Fit Stem: High Rates of Aseptic Loosening', *The Journal of Arthroplasty*, vol. 37, no. 1, pp. 97–102, Jan. 2022, doi: 10.1016/j.arth.2021.09.004.

[50] W. T. Hoskins, R. J. Bingham, M. Lorimer, and R. N. de Steiger, 'The Effect of Size for a Hydroxyapatite-Coated Cementless Implant on Component Revision in Total Hip Arthroplasty: An Analysis of 41,265 Stems', *The Journal of Arthroplasty*, vol. 35, no. 4, pp. 1074–1078, Apr. 2020, doi: 10.1016/j.arth.2019.10.060.

[51] L. I. Havelin, B. Espehaug, S. E. Vollset, and L. B. Engesaeter, 'Early aseptic loosening of uncemented femoral components in primary total hip replacement. A review based on the Norwegian Arthroplasty Register', *The Journal of Bone & Joint Surgery British Volume*, vol. 77-B, no. 1, pp. 11–17, Jan. 1995, doi: 10.1302/0301-620X.77B1.7822364.

[52] J. C. Keurentjes *et al.*, 'Which implant should we use for primary total hip replacement? A systematic review and meta-analysis', *J Bone Joint Surg Am*, vol. 96 Suppl 1, pp. 79–97, Dec. 2014, doi: 10.2106/JBJS.N.00397.

[53] U. Anil, V. Singh, and R. Schwarzkopf, 'Diagnosis and Detection of Subtle Aseptic Loosening in Total Hip Arthroplasty', *The Journal of Arthroplasty*, vol. 37, no. 8, pp. 1494–1500, Aug. 2022, doi: 10.1016/j.arth.2022.02.060.

[54] K. Deere, M. R. Whitehouse, S. K. Kunutsor, A. Sayers, J. Mason, and A. W. Blom, 'How long do revised and multiply revised hip replacements last? A retrospective observational study of the National Joint Registry', *The Lancet Rheumatology*, vol. 4, no. 7, pp. e468–e479, Jul. 2022, doi: 10.1016/S2665-9913(22)00097-2.

[55] U. Anil, V. Singh, and R. Schwarzkopf, 'Diagnosis and Detection of Subtle Aseptic Loosening in Total Hip Arthroplasty', *The Journal of Arthroplasty*, vol. 37, no. 8, pp. 1494–1500, Aug. 2022, doi: 10.1016/j.arth.2022.02.060.

[56] C. A. Engh, D. O'Connor, M. Jasty, T. F. McGovern, J. D. Bobyn, and W. H. Harris, 'Quantification of implant micromotion, strain shielding, and bone resorption with porous-coated anatomic medullary locking femoral prostheses', *Clin Orthop Relat Res*, no. 285, pp. 13–29, Dec. 1992.

[57] M. Viceconti, R. Muccini, M. Bernakiewicz, M. Baleani, and L. Cristofolini, 'Large-sliding contact elements accurately predict levels of bone-implant micromotion relevant to osseointegration', *J Biomech*, vol. 33, no. 12, pp. 1611–1618, Dec. 2000, doi: 10.1016/s0021-9290(00)00140-8.

[58] S. S. Shet *et al.*, 'Imaging evaluation of periprosthetic loosening: A primer for the general radiologist', *World J Radiol*, vol. 17, no. 2, p. 102373, Feb. 2025, doi: 10.4329/wjr.v17.i2.102373.

[59] T. A. Gruen, G. M. McNeice, and H. C. Amstutz, '"Modes of failure" of cemented stem-type femoral components: a radiographic analysis of loosening', *Clin Orthop Relat Res*, no. 141, pp. 17–27, Jun. 1979.

[60] J. G. Delee and J. Charnley, 'Radiological Demarcation of Cemented Sockets in Total Hip Replacement', *Clinical Orthopaedics and Related Research®*, no. 121, p. 20, Dec. 1976.

[61] J. Vanrusselt, M. Vansevenant, G. Vanderschueren, and F. Vanhoenacker, 'Postoperative radiograph of the hip arthroplasty: what the radiologist should know', *Insights Imaging*, vol. 6, no. 6, pp. 591–600, Dec. 2015, doi: 10.1007/s13244-015-0438-5.

[62] I. A. Lautiainen, J. Joukainen, and E. A. Mäkelä, 'Clinical and roentgenographic results of cementless total hip arthroplasty', *J Arthroplasty*, vol. 9, no. 6, pp. 653–660, Dec. 1994, doi: 10.1016/0883-5403(94)90120-1.

[63] E. J. Vresilovic, W. J. Hozack, and R. H. Rothman, 'Radiographic assessment of cementless femoral components. Correlation with intraoperative mechanical stability', *J Arthroplasty*, vol. 9, no. 2, pp. 137–141, Apr. 1994, doi: 10.1016/0883-5403(94)90062-0.

[64] O. P. P. Temmerman, P. G. H. M. Raijmakers, J. Berkhof, O. S. Hoekstra, G. J. J. Teule, and I. C. Heyligers, 'Accuracy of diagnostic imaging techniques in the diagnosis of aseptic loosening of the

femoral component of a hip prosthesis: A META-ANALYSIS', *The Journal of Bone & Joint Surgery British Volume*, vol. 87-B, no. 6, pp. 781–785, Jun. 2005, doi: 10.1302/0301-620X.87B6.15625.

[65] C. Khalily and L. A. Whiteside, 'Predictive value of early radiographic findings in cementless total hip arthroplasty femoral components: An 8- to 12-Year Follow-up', *The Journal of Arthroplasty*, vol. 13, no. 7, pp. 768–773, Oct. 1998, doi: 10.1016/S0883-5403(98)90028-6.

[66] A. LÜBBEKE, C. BAREA, M. ZINGG, N. LAUPER, D. HANNOUCHE, and G. GARAVAGLIA, 'Radiographic signs and hip pain 5 years after THA with a cemented stem predict future revision for aseptic loosening: a prospective cohort study', *Acta Orthop*, vol. 95, pp. 32–38, Jan. 2024, doi: 10.2340/17453674.2023.26190.

[67] 'Reliability of the Radiological Assessments of Radiolucency and Loosening in Total Hip Arthroplasty Using Pacs - Toby O. Smith, Timothy H.D. Williams, Arjun Samuel, Luke Ogonda, James A. Wimhurst, 2011'. Accessed: Sep. 09, 2025. [Online]. Available: https://journals.sagepub.com/doi/abs/10.5301/HIP.2011.8660

[68] D. A. O'Neill and W. H. Harris, 'Failed total hip replacement: assessment by plain radiographs, arthrograms, and aspiration of the hip joint.', *JBJS*, vol. 66, no. 4, p. 540, Apr. 1984.

[69] A. R. Patel, P. Sweeney, G. Ochenjele, R. Wixson, S. D. Stulberg, and L. M. Puri, 'Radiographically Silent Loosening of the Acetabular Component in Hip Arthroplasty', *Am J Orthop (Belle Mead NJ)*, vol. 44, no. 9, pp. 406–410, Sep. 2015.

[70] H. Malchau, J. Kärrholm, Y. X. Wang, and P. Herberts, 'Accuracy of migration analysis in hip arthroplasty. Digitized and conventional radiography, compared to radiostereometry in 51 patients', *Acta Orthop Scand*, vol. 66, no. 5, pp. 418–424, Oct. 1995, doi: 10.3109/17453679508995578.

[71] R. M. Pilliar, J. M. Lee, and C. Maniatopoulos, 'Observations on the effect of movement on bone ingrowth into porous-surfaced implants', *Clin Orthop Relat Res*, no. 208, pp. 108–113, Jul. 1986.

[72] J. Kärrholm, 'Roentgen stereophotogrammetry. Review of orthopedic applications', *Acta Orthop Scand*, vol. 60, no. 4, pp. 491–503, Aug. 1989, doi: 10.3109/17453678909149328.

[73] S. Sesselmann, R. Forst, and F. Tschunko, 'Radiostereometric analysis of hip implants: A critical review of methodology and future directions', *OA Musculoskeletal Medicine*, vol. 1, no. 4, Dec. 2013, doi: 10.13172/2052-9287-1-4-941.

[74] 'Guidance on the Selection of Prostheses for Primary Total Hip Replacement | Guidance | NICE'. Accessed: Sep. 10, 2025. [Online]. Available: https://www.nice.org.uk/guidance/ta2

[75] N. Börlin, S. M. Röhrl, and C. R. Bragdon, 'RSA wear measurements with or without markers in total hip arthroplasty', *J Biomech*, vol. 39, no. 9, pp. 1641–1650, 2006, doi: 10.1016/j.jbiomech.2005.05.004.

[76] V. Brinkmann, F. Radetzki, K. S. Delank, D. Wohlrab, and A. Zeh, 'A prospective randomized radiographic and dual-energy X-ray absorptiometric study of migration and bone remodeling after implantation of two modern short-stemmed femoral prostheses', *J Orthopaed Traumatol*, vol. 16, no. 3, pp. 237–243, Sep. 2015, doi: 10.1007/s10195-015-0335-1.

[77] B. Cohen and N. Rushton, ‘Accuracy of DEXA measurement of bone mineral density after total hip arthroplasty’, *J Bone Joint Surg Br*, vol. 77, no. 3, pp. 479–483, May 1995.

[78] T. Freitag, M.-A. Hein, D. Wernerus, H. Reichel, and R. Bieger, ‘Bone remodelling after femoral short stem implantation in total hip arthroplasty: 1-year results from a randomized DEXA study’, *Arch Orthop Trauma Surg*, vol. 136, no. 1, pp. 125–130, Jan. 2016, doi: 10.1007/s00402-015-2370-z.

[79] C. S. Moret, S. E. Masri, B. L. Schelker, N. F. Friederich, and M. T. Hirschmann, ‘Unexpected early loosening of rectangular straight femoral Zweymüller stems with an alumina-reduced surface after total hip arthroplasty—a prospective, double-blind, randomized controlled trial’, *Journal of Orthopaedics and Traumatology*, vol. 25, no. 1, p. 12, Mar. 2024, doi: 10.1186/s10195-023-00743-1.

[80] O. SANDBERG *et al.*, ‘Inducible displacement CT increases the diagnostic accuracy of aseptic loosening in primary total hip arthroplasty’, *Acta Orthop*, vol. 93, pp. 831–836, Oct. 2022, doi: 10.2340/17453674.2022.5240.

[81] H. Malchau, ‘IMPLANT MOVEMENT ANALYSIS: A CT-BASED TECHNIQUE TO DIAGNOSE EARLY LOOSENING IN TOTAL HIP ARTHROPLASTY’, *Orthopaedic Proceedings*, vol. 106-B, no. SUPP_16, pp. 80–80, Aug. 2024, doi: 10.1302/1358-992X.2024.16.080.

[82] S. Kohyama, Y. Yoshii, Y. Okamoto, and T. Nakajima, ‘Advances in Bone Joint Imaging-Metal Artifact Reduction’, *Diagnostics (Basel)*, vol. 12, no. 12, p. 3079, Dec. 2022, doi: 10.3390/diagnostics12123079.

[83] H. Tang, X. Huang, X. Cheng, D. Yang, Y. Huang, and Y. Zhou, ‘Evaluation of peri-prosthetic radiolucent lines surrounding the cementless femoral stem using digital tomosynthesis with metal artifact reduction: a cadaveric study in comparison with radiography and computed tomography’, *Quant Imaging Med Surg*, vol. 10, no. 9, pp. 1786–1800, Sep. 2020, doi: 10.21037/qims-19-1018.

[84] T. H. French, N. Russell, and A. Pillai, ‘The diagnostic accuracy of radionuclide arthrography for prosthetic loosening in hip and knee arthroplasty’, *Biomed Res Int*, vol. 2013, p. 693436, 2013, doi: 10.1155/2013/693436.

[85] A. Miniaci, W. H. Bailey, R. B. Bourne, A. C. McLaren, and C. H. Rorabeck, ‘Analysis of radionuclide arthrograms, radiographic arthrograms, and sequential plain radiographs in the assessment of painful hip arthroplasty’, *The Journal of Arthroplasty*, vol. 5, no. 2, pp. 143–149, Jun. 1990, doi: 10.1016/S0883-5403(06)80233-0.

[86] A. Marx, G. Saxler, S. Landgraeber, F. Löer, T. Holland-Letz, and M. von Knoch, ‘Comparison of subtraction arthrography, radionuclide arthrography and conventional plain radiography to assess loosening of total knee arthroplasty’, *Biomed Tech (Berl)*, vol. 50, no. 5, pp. 143–147, May 2005, doi: 10.1515/BMT.2005.021.

[87] O. P. P. Temmerman *et al.*, ‘Diagnostic accuracy and interobserver variability of plain radiography, subtraction arthrography, nuclear arthrography, and bone scintigraphy in the assessment of aseptic femoral component loosening’, *Arch Orthop Trauma Surg*, vol. 126, no. 5, pp. 316–323, Jul. 2006, doi: 10.1007/s00402-006-0120-y.

[88] R. F. Shah, S. A. Bini, A. M. Martinez, V. Pedoia, and T. P. Vail, 'Incremental inputs improve the automated detection of implant loosening using machine-learning algorithms', *The Bone & Joint Journal*, vol. 102-B, no. 6 Supple A, pp. 101–106, Jun. 2020, doi: 10.1302/0301-620X.102B6.BJJ-2019-1577.R1.

[89] T. Rahman *et al.*, 'HipXNet: Deep Learning Approaches to Detect Aseptic Loos-Ening of Hip Implants Using X-Ray Images', *IEEE Access*, vol. 10, pp. 53359–53373, 2022, doi: 10.1109/ACCESS.2022.3173424.

[90] M. Loppini, F. M. Gambaro, K. Chiappetta, G. Grappiolo, A. M. Bianchi, and V. D. A. Corino, 'Automatic Identification of Failure in Hip Replacement: An Artificial Intelligence Approach', *Bioengineering*, vol. 9, no. 7, p. 288, Jul. 2022, doi: 10.3390/bioengineering9070288.

[91] A. Borjali, A. F. Chen, O. K. Muratoglu, M. A. Morid, and K. M. Varadarajan, 'Detecting mechanical loosening of total hip replacement implant from plain radiograph using deep convolutional neural network', Jul. 05, 2022, *arXiv*: arXiv:1912.00943. doi: 10.48550/arXiv.1912.00943.

[92] M.-S. Kim, J.-J. Kim, K.-H. Kang, J.-H. Lee, and Y. In, 'Detection of Prosthetic Loosening in Hip and Knee Arthroplasty Using Machine Learning: A Systematic Review and Meta-Analysis', *Medicina (Kaunas)*, vol. 59, no. 4, p. 782, Apr. 2023, doi: 10.3390/medicina59040782.

[93] U. Anil, V. Singh, and R. Schwarzkopf, 'Diagnosis and Detection of Subtle Aseptic Loosening in Total Hip Arthroplasty', *The Journal of Arthroplasty*, vol. 37, no. 8, pp. 1494–1500, Aug. 2022, doi: 10.1016/j.arth.2022.02.060.

[94] R. M. Pilliar, J. M. Lee, and C. Maniatopoulos, 'Observations on the Effect of Movement on Bone Ingrowth into Porous-Surfaced Implants', *Clinical Orthopaedics and Related Research®*, vol. 208, p. 108, Jul. 1986.

[95] N. Kohli, J. C. Stoddart, and R. J. van Arkel, 'The limit of tolerable micromotion for implant osseointegration: a systematic review', *Sci Rep*, vol. 11, no. 1, p. 10797, May 2021, doi: 10.1038/s41598-021-90142-5.

[96] R. Bieger, A. Ignatius, R. Decking, L. Claes, H. Reichel, and L. Dürselen, 'Primary stability and strain distribution of cementless hip stems as a function of implant design', *Clinical Biomechanics*, vol. 27, no. 2, pp. 158–164, Feb. 2012, doi: 10.1016/j.clinbiomech.2011.08.004.

[97] R. Bieger, T. Freitag, A. Ignatius, H. Reichel, and L. Dürselen, 'Primary stability of a shoulderless Zweymüller hip stem: a comparative in vitro micromotion study', *J Orthop Surg Res*, vol. 11, p. 73, Jul. 2016, doi: 10.1186/s13018-016-0410-1.

[98] P. O. Østbyhaug, J. Klaksvik, P. Romundstad, and A. Aamodt, 'Primary stability of custom and anatomical uncemented femoral stems: a method for three-dimensional in vitro measurement of implant stability', *Clin Biomech (Bristol)*, vol. 25, no. 4, pp. 318–324, May 2010, doi: 10.1016/j.clinbiomech.2009.12.012.

[99] M. R. Abdul-Kadir, U. Hansen, R. Klabunde, D. Lucas, and A. Amis, 'Finite element modelling of primary hip stem stability: The effect of interference fit', *Journal of Biomechanics*, vol. 41, no. 3, pp. 587–594, Jan. 2008, doi: 10.1016/j.jbiomech.2007.10.009.

[100] A. Fottner, M. Schmid, C. Birkenmaier, F. Mazoochian, W. Plitz, and J. Volkmar, 'Biomechanical evaluation of two types of short-stemmed hip prostheses compared to the trust plate prosthesis by three-dimensional measurement of micromotions', *Clinical Biomechanics*, vol. 24, no. 5, pp. 429–434, Jun. 2009, doi: 10.1016/j.clinbiomech.2009.02.007.

[101] A. Fottner *et al.*, 'Biomechanical evaluation of different offset versions of a cementless hip prosthesis by 3-dimensional measurement of micromotions', *Clinical Biomechanics*, vol. 26, no. 8, pp. 830–835, Oct. 2011, doi: 10.1016/j.clinbiomech.2011.04.001.

[102] M. Viceconti, L. Monti, R. Muccini, M. Bernakiewicz, and A. Toni, 'Even a thin layer of soft tissue may compromise the primary stability of cementless hip stems', *Clinical Biomechanics*, vol. 16, no. 9, pp. 765–775, Nov. 2001, doi: 10.1016/S0268-0033(01)00052-3.

[103] C. Götze, W. Steens, V. Vieth, C. Poremba, L. Claes, and J. Steinbeck, 'Primary stability in cementless femoral stems: custom-made versus conventional femoral prosthesis', *Clinical Biomechanics*, vol. 17, no. 4, pp. 267–273, May 2002, doi: 10.1016/S0268-0033(02)00012-8.

[104] H.-J. Wilke, R. S. Seiz, M. Bombelli, L. Claes, and L. Dürselen, 'Biomechanical and histomorphological investigations on an isoelastic hip prosthesis after an eight month implantation period', *J Mater Sci: Mater Med*, vol. 5, no. 6, pp. 384–386, Jun. 1994, doi: 10.1007/BF00058969.

[105] J.-P. Kassi, M. O. Heller, U. Stoeckle, C. Perka, and G. N. Duda, 'Stair climbing is more critical than walking in pre-clinical assessment of primary stability in cementless THA in vitro', *Journal of Biomechanics*, vol. 38, no. 5, pp. 1143–1154, May 2005, doi: 10.1016/j.jbiomech.2004.05.023.

[106] S. Gheduzzi and A. W. Miles, 'A review of pre-clinical testing of femoral stem subsidence and comparison with clinical data', *Proc Inst Mech Eng H*, vol. 221, no. 1, pp. 39–46, Jan. 2007, doi: 10.1243/09544119JEIM129.

[107] S. H. Pettersen, T. S. Wik, and B. Skallerud, 'Subject specific finite element analysis of implant stability for a cementless femoral stem', *Clinical Biomechanics*, vol. 24, no. 6, pp. 480–487, Jul. 2009, doi: 10.1016/j.clinbiomech.2009.03.009.

[108] J. R. Britton, L. A. Walsh, and P. J. Prendergast, 'Mechanical simulation of muscle loading on the proximal femur: analysis of cemented femoral component migration with and without muscle loading', *Clinical Biomechanics*, vol. 18, no. 7, pp. 637–646, Aug. 2003, doi: 10.1016/S0268-0033(03)00113-X.

[109] M. Gortchacow, M. Wettstein, D. P. Pioletti, and A. Terrier, 'A new technique to measure micromotion distribution around a cementless femoral stem', *J Biomech*, vol. 44, no. 3, pp. 557–560, Feb. 2011, doi: 10.1016/j.jbiomech.2010.09.023.

[110] M. Gortchacow, M. Wettstein, D. P. Pioletti, M. Müller-Gerbl, and A. Terrier, 'Simultaneous and multisite measure of micromotion, subsidence and gap to evaluate femoral stem stability', *J Biomech*, vol. 45, no. 7, pp. 1232–1238, Apr. 2012, doi: 10.1016/j.jbiomech.2012.01.040.

[111] L. Monti, L. Cristofolini, and M. Viceconti, ‘Methods for Quantitative Analysis of the Primary Stability in Uncemented Hip Prostheses’, *Artificial Organs*, vol. 23, no. 9, pp. 851–859, 1999, doi: 10.1046/j.1525-1594.1999.06287.x.

[112] L. Cristofolini, E. Varini, I. Pelgreffi, A. Cappello, and A. Toni, ‘Device to measure intra-operatively the primary stability of cementless hip stems’, *Medical Engineering & Physics*, vol. 28, no. 5, pp. 475–482, Jun. 2006, doi: 10.1016/j.medengphy.2005.07.015.

[113] B. Reggiani, L. Cristofolini, F. Taddei, and M. Viceconti, ‘Sensitivity of the Primary Stability of a Cementless Hip Stem to Its Position and Orientation’, *Artificial Organs*, vol. 32, no. 7, pp. 555–560, 2008, doi: 10.1111/j.1525-1594.2008.00577.x.

[114] B. Reggiani, L. Cristofolini, E. Varini, and M. Viceconti, ‘Predicting the subject-specific primary stability of cementless implants during pre-operative planning: Preliminary validation of subject-specific finite-element models’, *Journal of Biomechanics*, vol. 40, no. 11, pp. 2552–2558, Jan. 2007, doi: 10.1016/j.jbiomech.2006.10.042.

[115] F. Schmidutz, M. Woiczinski, M. Kistler, C. Schröder, V. Jansson, and A. Fottner, ‘Influence of different sizes of composite femora on the biomechanical behavior of cementless hip prosthesis’, *Clinical Biomechanics*, vol. 41, pp. 60–65, Jan. 2017, doi: 10.1016/j.clinbiomech.2016.12.003.

[116] B. Wang, Q. Li, J. Dong, D. Zhou, and F. Liu, ‘Comparisons of the surface micromotions of cementless femoral prosthesis in the horizontal and vertical levels: a network analysis of biomechanical studies’, *Journal of Orthopaedic Surgery and Research*, vol. 15, no. 1, p. 293, Jul. 2020, doi: 10.1186/s13018-020-01794-4.

[117] D. W. Burke, D. O. O’Connor, E. B. Zalenski, M. Jasty, and W. H. Harris, ‘Micromotion of cemented and uncemented femoral components’, *The Journal of Bone & Joint Surgery British Volume*, vol. 73-B, no. 1, pp. 33–37, Jan. 1991, doi: 10.1302/0301-620X.73B1.1991771.

[118] M. Baleani, L. Cristofolini, and A. Toni, ‘Initial stability of a new hybrid fixation hip stem: Experimental measurement of implant–bone micromotion under torsional load in comparison with cemented and cementless stems’, *Journal of Biomedical Materials Research*, vol. 50, no. 4, pp. 605–615, 2000, doi: 10.1002/(SICI)1097-4636(20000615)50:4<605::AID-JBM17>3.0.CO;2-P.

[119] H. McKellop, E. Ebramzadeh, P. G. Niederer, and A. Sarmiento, ‘Comparison of the stability of press-fit hip prosthesis femoral stems using a synthetic model femur’, *Journal of Orthopaedic Research*, vol. 9, no. 2, pp. 297–305, 1991, doi: 10.1002/jor.1100090219.

[120] E. Schneider, C. Kinast, J. Eulenberger, D. Wyder, G. Eskilsson, and S. M. Perren, ‘A Comparative Study of the Initial Stability of Cementless Hip Prostheses’, *Clinical Orthopaedics and Related Research®*, vol. 248, p. 200, Nov. 1989.

[121] L. Claes, S. Fiedler, M. Ohnmacht, and G. N. Duda, ‘Initial stability of fully and partially cemented femoral stems’, *Clinical Biomechanics*, vol. 15, no. 10, pp. 750–755, Dec. 2000, doi: 10.1016/S0268-0033(00)00044-9.

[122] P. A. Manley, R. Vanderby, S. Kohles, M. D. Markel, and J. P. Heiner, 'Alterations in femoral strain, micromotion, cortical geometry, cortical porosity, and bony ingrowth in uncemented collared and collarless prostheses in the dog', *The Journal of Arthroplasty*, vol. 10, no. 1, pp. 63–73, Feb. 1995, doi: 10.1016/S0883-5403(05)80102-0.

[123] S. D. Cook, K. A. Thomas, J. F. Kay, and M. Jarcho, 'Hydroxyapatite-coated porous titanium for use as an orthopedic biologic attachment system', *Clin Orthop Relat Res*, no. 230, pp. 303–312, May 1988.

[124] W. R. Walsh *et al.*, 'Bone ongrowth and mechanical fixation of implants in cortical and cancellous bone', *Journal of Orthopaedic Surgery and Research*, vol. 15, no. 1, p. 177, May 2020, doi: 10.1186/s13018-020-01696-5.

[125] M. Svehla, P. Morberg, B. Zicat, W. Bruce, D. Sonnabend, and W. R. Walsh, 'Morphometric and mechanical evaluation of titanium implant integration: comparison of five surface structures', *J Biomed Mater Res*, vol. 51, no. 1, pp. 15–22, Jul. 2000, doi: 10.1002/(sici)1097-4636(200007)51:1<15::aid-jbm3>3.0.co;2-9.

[126] S. Brogini *et al.*, 'Osseointegration of additive manufacturing Ti-6Al-4V and Co-Cr-Mo alloys, with and without surface functionalization with hydroxyapatite and type I collagen', *J Mech Behav Biomed Mater*, vol. 115, p. 104262, Mar. 2021, doi: 10.1016/j.jmbbm.2020.104262.

[127] Y. Huang *et al.*, 'Osteoconductivity and osteoinductivity of porous hydroxyapatite coatings deposited by liquid precursor plasma spraying: in vivo biological response study', *Biomed. Mater.*, vol. 9, no. 6, p. 065007, Nov. 2014, doi: 10.1088/1748-6041/9/6/065007.

[128] S. Baroni *et al.*, 'Calibration of Aseptic Loosening Simulation for Coatings Osteoinductive Effect', *Ann Biomed Eng*, vol. 53, no. 1, pp. 34–47, Jan. 2025, doi: 10.1007/s10439-024-03588-9.

[129] R. D. Bloebaum, N. T. Abdo, A. A. Hofmann, R. T. Epperson, R. E. Olsen, and O. Chalayon, 'Transcortical or intracondylar? Which model is accurate for predicting biomaterial attachment in total joint replacement?', *Journal of Biomedical Materials Research Part B: Applied Biomaterials*, vol. 106, no. 2, pp. 578–588, 2018, doi: 10.1002/jbm.b.33873.

[130] A. A. Hofmann, R. D. Bloebaum, and K. N. Bachus, 'Progression of human bone ingrowth into porous-coated implants. Rate of bone ingrowth in humans', *Acta Orthop Scand*, vol. 68, no. 2, pp. 161–166, Apr. 1997, doi: 10.3109/17453679709004000.

[131] A. Pancanti, M. Bernakiewicz, and M. Viceconti, 'The primary stability of a cementless stem varies between subjects as much as between activities', *Journal of Biomechanics*, vol. 36, no. 6, pp. 777–785, Jun. 2003, doi: 10.1016/S0021-9290(03)00011-3.

[132] R. M. A. Al-Dirini *et al.*, 'Virtual trial to evaluate the robustness of cementless femoral stems to patient and surgical variation', *J Biomech*, vol. 82, pp. 346–356, Jan. 2019, doi: 10.1016/j.jbiomech.2018.11.013.

[133] M. Viceconti *et al.*, 'Position Paper: Extending Credibility Assessment of In Silico Medicine Predictors to Machine Learning Predictors', *IEEE Journal of Biomedical and Health Informatics*, vol. 29, no. 7, pp. 5284–5290, Jul. 2025, doi: 10.1109/JBHI.2025.3552320.

[134] S. M. Kurtz *et al.*, 'International survey of primary and revision total knee replacement', *Int Orthop*, vol. 35, no. 12, pp. 1783–1789, Dec. 2011, doi: 10.1007/s00264-011-1235-5.

[135] H. Yamada *et al.*, 'Cementless total hip replacement: past, present, and future', *J Orthop Sci*, vol. 14, no. 2, pp. 228–241, Mar. 2009, doi: 10.1007/s00776-008-1317-4.

[136] N. Toossi, B. Adeli, A. J. Timperley, F. S. Haddad, M. Maltenfort, and J. Parvizi, 'Acetabular components in total hip arthroplasty: is there evidence that cementless fixation is better?', *J Bone Joint Surg Am*, vol. 95, no. 2, pp. 168–174, Jan. 2013, doi: 10.2106/JBJS.K.01652.

[137] Report of RIPO, 'Overall data on hip, knee and shoulder arthroplasty in Emilia Romagna region (Italy, 2000–2019)', 2022, [Online]. Available: http://ripo.cineca.it/authzssl/Reports.html

[138] 'National Joint Registry. 20th Annual report 2023'. [Online]. Available: https://reports.njrcentre.org.uk/Portals/0/PDFdownloads/NJR%2020th%20Annual%20Report%202023.pdf

[139] K. Iamthanaporn, K. Chareancholvanich, and C. Pornrattanamaneewong, 'Revision primary total hip replacement: causes and risk factors', *J Med Assoc Thai*, vol. 98, no. 1, pp. 93–99, Jan. 2015.

[140] P. Sadoghi, M. Liebensteiner, M. Agreiter, A. Leithner, N. Böhler, and G. Labek, 'Revision surgery after total joint arthroplasty: a complication-based analysis using worldwide arthroplasty registers', *J Arthroplasty*, vol. 28, no. 8, pp. 1329–1332, Sep. 2013, doi: 10.1016/j.arth.2013.01.012.

[141] R. J. Ferguson, A. J. Palmer, A. Taylor, M. L. Porter, H. Malchau, and S. Glyn-Jones, 'Hip replacement', *The Lancet*, vol. 392, no. 10158, pp. 1662–1671, Nov. 2018, doi: 10.1016/S0140-6736(18)31777-X.

[142] L. Janssen, K. A. P. Wijnands, D. Janssen, M. W. H. E. Janssen, and J. W. Morrenhof, 'Do Stem Design and Surgical Approach Influence Early Aseptic Loosening in Cementless THA?', *Clin Orthop Relat Res*, vol. 476, no. 6, pp. 1212–1220, Jun. 2018, doi: 10.1007/s11999.0000000000000208.

[143] J. C. Keurentjes *et al.*, 'Which implant should we use for primary total hip replacement? A systematic review and meta-analysis', *J Bone Joint Surg Am*, vol. 96 Suppl 1, pp. 79–97, Dec. 2014, doi: 10.2106/JBJS.N.00397.

[144] O. Graudejus, R. Ponce Wong, N. Varghese, S. Wagner, and B. Morrison, 'Bridging the gap between in vivo and in vitro research: Reproducing in vitro the mechanical and electrical environment of cells in vivo', *Front. Cell. Neurosci.*, vol. 12, 2018, doi: 10.3389/conf.fncel.2018.38.00069.

[145] A. AKHTAR, 'The Flaws and Human Harms of Animal Experimentation', *Camb Q Healthc Ethics*, vol. 24, no. 4, pp. 407–419, Oct. 2015, doi: 10.1017/S0963180115000079.

[146] M. Viceconti, S. Affatato, M. Baleani, B. Bordini, L. Cristofolini, and F. Taddei, 'Pre-clinical validation of joint prostheses: A systematic approach', *Journal of the Mechanical Behavior of Biomedical Materials*, vol. 2, no. 1, pp. 120–127, Jan. 2009, doi: 10.1016/j.jmbbm.2008.02.005.

[147] M. Taylor and P. J. Prendergast, 'Four decades of finite element analysis of orthopaedic devices: Where are we now and what are the opportunities?', *Journal of Biomechanics*, vol. 48, no. 5, pp. 767–778, Mar. 2015, doi: 10.1016/j.jbiomech.2014.12.019.

[148] M. Taylor, R. Bryan, and F. Galloway, 'Accounting for patient variability in finite element analysis of the intact and implanted hip and knee: A review', *Numer Methods Biomed Eng*, vol. 29, no. 2, pp. 273–292, Feb. 2013, doi: 10.1002/cnm.2530.

[149] M. Viceconti *et al.*, 'Possible Contexts of Use for In Silico Trials Methodologies: A Consensus-Based Review', *IEEE Journal of Biomedical and Health Informatics*, vol. 25, no. 10, pp. 3977–3982, Oct. 2021, doi: 10.1109/JBHI.2021.3090469.

[150] P. Favre, G. Maquer, A. Henderson, D. Hertig, D. Ciric, and J. E. Bischoff, 'In Silico Clinical Trials in the Orthopedic Device Industry: From Fantasy to Reality?', *Ann Biomed Eng*, vol. 49, no. 12, pp. 3213–3226, Dec. 2021, doi: 10.1007/s10439-021-02787-y.

[151] P. Pankaj, 'Patient-specific modelling of bone and bone-implant systems: the challenges', *Int J Numer Method Biomed Eng*, vol. 29, no. 2, pp. 233–249, Feb. 2013, doi: 10.1002/cnm.2536.

[152] A. Andrade-Campos, A. Ramos, and J. A. Simões, 'A model of bone adaptation as a topology optimization process with contact', *Journal of Biomedical Science and Engineering*, vol. 5, no. 5, Art. no. 5, May 2012, doi: 10.4236/jbise.2012.55030.

[153] S. Chanda, K. Mukherjee, S. Gupta, and D. K. Pratihar, 'A comparative assessment of two designs of hip stem using rule-based simulation of combined osseointegration and remodelling', *Proc Inst Mech Eng H*, vol. 234, no. 1, pp. 118–128, Jan. 2020, doi: 10.1177/0954411919890998.

[154] M. Tarala, D. Janssen, and N. Verdonschot, 'Balancing incompatible endoprosthetic design goals: A combined ingrowth and bone remodeling simulation', *Medical Engineering & Physics*, vol. 33, no. 3, pp. 374–380, Apr. 2011, doi: 10.1016/j.medengphy.2010.11.005.

[155] M. Viceconti, A. Pancanti, M. Dotti, F. Traina, and L. Cristofolini, 'Effect of the initial implant fitting on the predicted secondary stability of a cementless stem', *Med Biol Eng Comput*, vol. 42, no. 2, pp. 222–229, Mar. 2004, doi: 10.1007/BF02344635.

[156] J. Folgado, P. R. Fernandes, C. R. Jacobs, and V. D. Pellegrini, 'Influence of femoral stem geometry, material and extent of porous coating on bone ingrowth and atrophy in cementless total hip arthroplasty: an iterative finite element model', *Comput Methods Biomech Biomed Engin*, vol. 12, no. 2, pp. 135–145, Apr. 2009, doi: 10.1080/10255840903081123.

[157] P. R. Fernandes, J. Folgado, C. Jacobs, and V. Pellegrini, 'A contact model with ingrowth control for bone remodelling around cementless stems', *Journal of Biomechanics*, vol. 35, no. 2, pp. 167–176, Feb. 2002, doi: 10.1016/S0021-9290(01)00204-4.

[158] R. B. Ruben, P. R. Fernandes, and J. Folgado, 'On the optimal shape of hip implants', *Journal of Biomechanics*, vol. 45, no. 2, pp. 239–246, Jan. 2012, doi: 10.1016/j.jbiomech.2011.10.038.

[159] F. Tarlochan, H. Mehboob, A. Mehboob, and S.-H. Chang, 'Influence of functionally graded pores on bone ingrowth in cementless hip prosthesis: a finite element study using mechano-regulatory algorithm', *Biomech Model Mechanobiol*, vol. 17, no. 3, pp. 701–716, Jun. 2018, doi: 10.1007/s10237-017-0987-2.

[160] R. Ghosh, A. Hazra, S. Chanda, and D. Chakraborty, 'Computational assessment of growth of connective tissues around textured hip stem subjected to daily activities after THA', *Med Biol Eng Comput*, vol. 61, no. 2, pp. 525–540, Feb. 2023, doi: 10.1007/s11517-022-02729-3.

[161] P. K. Puthumanapully and M. Browne, 'Tissue differentiation around a short stemmed metaphyseal loading implant employing a modified mechanoregulatory algorithm: A finite element study', *Journal of Orthopaedic Research*, vol. 29, no. 5, pp. 787–794, 2011, doi: 10.1002/jor.21305.

[162] R. Ghosh, S. Chanda, and D. Chakraborty, 'The influence of macro-textural designs over implant surface on bone on-growth: A computational mechanobiology based study', *Computers in Biology and Medicine*, vol. 124, p. 103937, Sep. 2020, doi: 10.1016/j.compbiomed.2020.103937.

[163] H. Mehboob, F. Ahmad, F. Tarlochan, A. Mehboob, and S. H. Chang, 'A comprehensive analysis of bio-inspired design of femoral stem on primary and secondary stabilities using mechanoregulatory algorithm', *Biomech Model Mechanobiol*, vol. 19, no. 6, pp. 2213–2226, Dec. 2020, doi: 10.1007/s10237-020-01334-3.

[164] P. Moreo, M. A. Pérez, J. M. García-Aznar, and M. Doblaré, 'Modelling the mechanical behaviour of living bony interfaces', *Computer Methods in Applied Mechanics and Engineering*, vol. 196, no. 35, pp. 3300–3314, Jul. 2007, doi: 10.1016/j.cma.2007.03.020.

[165] R. Ghosh, S. Chanda, and D. Chakraborty, 'Influence of sequential opening/closing of interface gaps and texture density on bone growth over macro-textured implant surfaces using FE based mechanoregulatory algorithm', *Computer Methods in Biomechanics and Biomedical Engineering*, vol. 25, no. 9, pp. 985–999, Jul. 2022, doi: 10.1080/10255842.2021.1994960.

[166] P. Büchler, D. P. Pioletti, and L. R. Rakotomanana, 'Biphasic constitutive laws for biological interface evolution', *Biomech Model Mechanobiol*, vol. 1, no. 4, pp. 239–249, Apr. 2003, doi: 10.1007/s10237-002-0024-x.

[167] M. Tarala, D. Janssen, and N. Verdonschot, 'Toward a method to simulate the process of bone ingrowth in cementless THA using finite element method', *Medical Engineering & Physics*, vol. 35, no. 4, pp. 543–548, Apr. 2013, doi: 10.1016/j.medengphy.2012.10.010.

[168] M. Viceconti, S. Ricci, A. Pancanti, and A. Cappello, 'Numerical model to predict the longterm mechanical stability of cementless orthopaedic implants', *Med. Biol. Eng. Comput.*, vol. 42, no. 6, pp. 747–753, Nov. 2004, doi: 10.1007/BF02345207.

[169] P. Prendergast, 'Finite element models in tissue mechanics and orthopaedic implant design', *Clinical Biomechanics*, vol. 12, no. 6, pp. 343–366, Sep. 1997, doi: 10.1016/S0268-0033(97)00018-1.

[170] R. Ghosh, S. Chanda, and D. Chakraborty, 'Application of finite element analysis to tissue differentiation and bone remodelling approaches and their use in design optimization of orthopaedic implants: A review', *International Journal for Numerical Methods in Biomedical Engineering*, vol. 38, no. 10, p. e3637, 2022, doi: 10.1002/cnm.3637.

[171] F. S. Fröschen, D. C. Wirtz, and F. A. Schildberg, '[Physiological reactions in the interface between cementless implants and bone]', *Orthopadie (Heidelb)*, vol. 52, no. 3, pp. 178–185, Mar. 2023, doi: 10.1007/s00132-023-04347-9.

[172] A. S. Vio War, N. Kumar, and S. Chanda, 'Does preclinical analysis based on static loading underestimate post-surgery stem micromotion in THA as opposed to dynamic gait loading?', *Med Biol Eng Comput*, vol. 61, no. 6, pp. 1473–1488, Jun. 2023, doi: 10.1007/s11517-023-02801-6.

[173] S. Checa and P. J. Prendergast, 'A Mechanobiological Model for Tissue Differentiation that Includes Angiogenesis: A Lattice-Based Modeling Approach', *Ann Biomed Eng*, vol. 37, no. 1, pp. 129–145, Jan. 2009, doi: 10.1007/s10439-008-9594-9.

[174] X. Liu and G. L. Niebur, 'Bone ingrowth into a porous coated implant predicted by a mechano-regulatory tissue differentiation algorithm', *Biomech Model Mechanobiol*, vol. 7, no. 4, pp. 335–344, Aug. 2008, doi: 10.1007/s10237-007-0100-3.

[175] T. S. Buchanan, D. G. Lloyd, K. Manal, and T. F. Besier, 'Estimation of muscle forces and joint moments using a forward-inverse dynamics model', *Med Sci Sports Exerc*, vol. 37, no. 11, pp. 1911–1916, Nov. 2005, doi: 10.1249/01.mss.0000176684.24008.6f.

[176] A. Lutz and U. Nackenhorst, 'A Computational Approach on the Osseointegration of Bone Implants Based on a Bio-Active Interface Theory', *GAMM-Mitteilungen*, vol. 32, no. 2, pp. 178–192, 2009, doi: 10.1002/gamm.200910015.

[177] B. Mathai and S. Gupta, 'Bone Ingrowth Around an Uncemented Femoral Implant Using Mechanoregulatory Algorithm: A Multiscale Finite Element Analysis', *Journal of Biomechanical Engineering*, vol. 144, no. 021004, Sep. 2021, doi: 10.1115/1.4052227.

[178] A. Lutz and U. Nackenhorst, 'Numerical investigations on the osseointegration of uncemented endoprostheses based on bio-active interface theory', *Comput Mech*, vol. 50, no. 3, pp. 367–381, Sep. 2012, doi: 10.1007/s00466-011-0635-0.

[179] F. Taddei, A. Pancanti, and M. Viceconti, 'An improved method for the automatic mapping of computed tomography numbers onto finite element models', *Medical Engineering & Physics*, vol. 26, no. 1, pp. 61–69, Jan. 2004, doi: 10.1016/S1350-4533(03)00138-3.

[180] M. Viceconti, M. Casali, B. Massari, L. Cristofolini, S. Bassini, and A. Toni, 'The "standardized femur program" proposal for a reference geometry to be used for the creation of finite element models of the femur', *J Biomech*, vol. 29, no. 9, p. 1241, Sep. 1996, doi: 10.1016/0021-9290(95)00164-6.

[181] J. Guedes and N. Kikuchi, 'Preprocessing and postprocessing for materials based on the homogenization method with adaptive finite element methods', *Computer Methods in Applied Mechanics and Engineering*, vol. 83, no. 2, pp. 143–198, Oct. 1990, doi: 10.1016/0045-7825(90)90148-F.

[182] *Non-Homogeneous Media and Vibration Theory*, vol. 127. in Lecture Notes in Physics, vol. 127. Berlin, Heidelberg: Springer, 1980. doi: 10.1007/3-540-10000-8.

[183] M. Viceconti, R. Muccini, M. Bernakiewicz, M. Baleani, and L. Cristofolini, 'Large-sliding contact elements accurately predict levels of bone–implant micromotion relevant to osseointegration', *Journal of Biomechanics*, vol. 33, no. 12, pp. 1611–1618, Dec. 2000, doi: 10.1016/S0021-9290(00)00140-8.

[184] J. A. Oliveira, J. Pinho-da-Cruz, and F. Teixeira-Dias, 'Asymptotic homogenisation in linear elasticity. Part II: Finite element procedures and multiscale applications', *Computational Materials Science*, vol. 45, no. 4, pp. 1081–1096, Jun. 2009, doi: 10.1016/j.commatsci.2009.01.027.

[185] J. A. Simões and A. T. Marques, 'Design of a composite hip femoral prosthesis', *Materials & Design*, vol. 26, no. 5, pp. 391–401, Aug. 2005, doi: 10.1016/j.matdes.2004.07.024.

[186] G. Bergmann *et al.*, 'Hip contact forces and gait patterns from routine activities', *Journal of Biomechanics*, vol. 34, no. 7, pp. 859–871, Jul. 2001, doi: 10.1016/S0021-9290(01)00040-9.

[187] M. O. Heller, G. Bergmann, J.-P. Kassi, L. Claes, N. P. Haas, and G. N. Duda, 'Determination of muscle loading at the hip joint for use in pre-clinical testing', *Journal of Biomechanics*, vol. 38, no. 5, pp. 1155–1163, May 2005, doi: 10.1016/j.jbiomech.2004.05.022.

[188] M. O. Heller *et al.*, 'Musculo-skeletal loading conditions at the hip during walking and stair climbing', *Journal of Biomechanics*, vol. 34, no. 7, pp. 883–893, Jul. 2001, doi: 10.1016/S0021-9290(01)00039-2.

[189] D. R. Pedersen, R. A. Brand, and D. T. Davy, 'Pelvic muscle and acetabular contact forces during gait', *J Biomech*, vol. 30, no. 9, pp. 959–965, Sep. 1997, doi: 10.1016/s0021-9290(97)00041-9.

[190] J. Kuiper, 'Numerical optimization of artificial hip joint designs', 1993. Accessed: Feb. 22, 2024. [Online]. Available: https://www.semanticscholar.org/paper/Numerical-optimization-of-artificial-hip-joint-Kuiper/24463050f5a1fce93d8190a3d17ffacbbf7a5479

[191] T. M. Keaveny and D. L. Bartel, 'Effects of porous coating, with and without collar support, on early relative motion for a cementless hip prosthesis', *Journal of Biomechanics*, vol. 26, no. 12, pp. 1355–1368, Dec. 1993, doi: 10.1016/0021-9290(93)90087-U.

[192] M. Jasty, C. Bragdon, D. Burke, D. O'Connor, J. Lowenstein, and W. H. Harris, 'In vivo skeletal responses to porous-surfaced implants subjected to small induced motions', *J Bone Joint Surg Am*, vol. 79, no. 5, pp. 707–714, May 1997, doi: 10.2106/00004623-199705000-00010.

[193] S. Szmukler-Moncler, H. Salama, Y. Reingewirtz, and J. H. Dubruille, 'Timing of loading and effect of micromotion on bone-dental implant interface: review of experimental literature', *J Biomed Mater Res*, vol. 43, no. 2, pp. 192–203, 1998, doi: 10.1002/(sici)1097-4636(199822)43:2<192::aid-jbm14>3.0.co;2-k.

[194] D. W. Burke, D. O. O'Connor, E. B. Zalenski, M. Jasty, and W. H. Harris, 'Micromotion of cemented and uncemented femoral components', *The Journal of Bone & Joint Surgery British Volume*, vol. 73-B, no. 1, pp. 33–37, Jan. 1991, doi: 10.1302/0301-620X.73B1.1991771.

[195] C. A. Simmons, S. A. Meguid, and R. M. Pilliar, 'Mechanical regulation of localized and appositional bone formation around bone-interfacing implants', *J Biomed Mater Res*, vol. 55, no. 1, pp. 63–71, Apr. 2001, doi: 10.1002/1097-4636(200104)55:1<63::aid-jbm90>3.0.co;2-v.

[196] A. Lutz and U. Nackenhorst, ‘Computation of static-equivalent load sets for bone remodeling simulation’, *PAMM*, vol. 7, no. 1, pp. 4020007–4020008, 2007, doi: 10.1002/pamm.200700235.

[197] R. Huiskes, H. Weinans, H. J. Grootenboer, M. Dalstra, B. Fudala, and T. J. Slooff, ‘Adaptive bone-remodeling theory applied to prosthetic-design analysis’, *J Biomech*, vol. 20, no. 11–12, pp. 1135–1150, 1987, doi: 10.1016/0021-9290(87)90030-3.

[198] H. Isaksson, W. Wilson, C. C. van Donkelaar, R. Huiskes, and K. Ito, ‘Comparison of biophysical stimuli for mechano-regulation of tissue differentiation during fracture healing’, *J Biomech*, vol. 39, no. 8, pp. 1507–1516, 2006, doi: 10.1016/j.jbiomech.2005.01.037.

[199] M. Viceconti, L. Monti, R. Muccini, M. Bernakiewicz, and A. Toni, ‘Even a thin layer of soft tissue may compromise the primary stability of cementless hip stems’, *Clin Biomech (Bristol, Avon)*, vol. 16, no. 9, pp. 765–775, Nov. 2001, doi: 10.1016/s0268-0033(01)00052-3.

[200] D. Lacroix and P. J. Prendergast, ‘A mechano-regulation model for tissue differentiation during fracture healing: analysis of gap size and loading’, *J Biomech*, vol. 35, no. 9, pp. 1163–1171, Sep. 2002, doi: 10.1016/s0021-9290(02)00086-6.

[201] D. R. Carter, P. R. Blenman, and G. S. Beaupré, ‘Correlations between mechanical stress history and tissue differentiation in initial fracture healing’, *J Orthop Res*, vol. 6, no. 5, pp. 736–748, 1988, doi: 10.1002/jor.1100060517.

[202] F. Lebon and S. Ronel-Idrissi, ‘Asymptotic analysis of Mohr-Coulomb and Drucker-Prager soft thin layers’, *1*, vol. 4, no. 2, Art. no. 2, Apr. 2004.

[203] A. G. Robling and C. H. Turner, ‘Mechanical Signaling for Bone Modeling and Remodeling’, *Crit Rev Eukaryot Gene Expr*, vol. 19, no. 4, pp. 319–338, 2009.

[204] D. J. Hadjidakis and I. I. Androulakis, ‘Bone Remodeling’, *Annals of the New York Academy of Sciences*, vol. 1092, no. 1, pp. 385–396, 2006, doi: 10.1196/annals.1365.035.

[205] M. Feyzi, K. Fallahnezhad, M. Taylor, and R. Hashemi, ‘A review on the finite element simulation of fretting wear and corrosion in the taper junction of hip replacement implants’, *Computers in Biology and Medicine*, vol. 130, p. 104196, Mar. 2021, doi: 10.1016/j.compbiomed.2020.104196.

[206] ASME, ‘V&V 40 - 2018: Assessing Credibility of Computational Modeling through Verification and Validation: Application to Medical Devices’, 2018.

[207] F. S. Santori, M. Manili, N. Fredella, M. Tonci Ottieri, and N. Santori, ‘Ultra-short stems with proximal load transfer: Clinical and radiographic results at five-year follow-up’, *Hip Int*, vol. 16 Suppl 3, pp. 31–39, 2006, doi: 10.1177/112070000601603S06.

[208] N. Kohli, J. C. Stoddart, and R. J. van Arkel, ‘The limit of tolerable micromotion for implant osseointegration: a systematic review’, *Sci Rep*, vol. 11, no. 1, Art. no. 1, May 2021, doi: 10.1038/s41598-021-90142-5.

[209] L. B. Murphy *et al.*, ‘One in four people may develop symptomatic hip osteoarthritis in his or her lifetime’, *Osteoarthritis Cartilage*, vol. 18, no. 11, pp. 1372–1379, Nov. 2010, doi: 10.1016/j.joca.2010.08.005.

[210] Z. Fan *et al.*, 'The prevalence of hip osteoarthritis: a systematic review and meta-analysis', *Arthritis Research & Therapy*, vol. 25, no. 1, p. 51, Mar. 2023, doi: 10.1186/s13075-023-03033-7.

[211] C. F. van Eck, A. F. Chen, B. A. Klatt, J. D'Antonio, and F. Fu, 'The classification of implants: class I, II, III', *J Long Term Eff Med Implants*, vol. 19, no. 3, pp. 185–193, 2009, doi: 10.1615/jlongtermeffmedimplants.v19.i3.30.

[212] 'Regulation - 2017/745 - EN - Medical Device Regulation - EUR-Lex'. Accessed: Sep. 03, 2025. [Online]. Available: https://eur-lex.europa.eu/eli/reg/2017/745/oj/eng

[213] M. Viceconti *et al.*, 'Possible Contexts of Use for In Silico Trials Methodologies: A Consensus-Based Review', *IEEE Journal of Biomedical and Health Informatics*, vol. 25, no. 10, pp. 3977–3982, Oct. 2021, doi: 10.1109/JBHI.2021.3090469.

[214] 'VV40-Assessing Credibility of Computational Modeling through Verification and Validation Application to Medical Devices - ASME'. Accessed: Sep. 03, 2025. [Online]. Available: https://www.asme.org/codes-standards/find-codes-standards/assessing-credibility-of-computational-modeling-through-verification-and-validation-application-to-medical-devices

[215] M. Mercuri *et al.*, 'Towards an Automated Computational Workflow to Assess Primary Stability in Total Hip Arthroplasty', *Bioengineering*, vol. 12, no. 7, p. 723, Jul. 2025, doi: 10.3390/bioengineering12070723.

[216] B. Irons and M. Loikkanen, 'An engineers' defence of the patch test', *International Journal for Numerical Methods in Engineering*, vol. 19, no. 9, pp. 1391–1401, 1983, doi: 10.1002/nme.1620190908.

[217] F. Taddei, E. Schileo, B. Helgason, L. Cristofolini, and M. Viceconti, 'The material mapping strategy influences the accuracy of CT-based finite element models of bones: an evaluation against experimental measurements', *Med Eng Phys*, vol. 29, no. 9, pp. 973–979, Nov. 2007, doi: 10.1016/j.medengphy.2006.10.014.

[218] E. Schileo *et al.*, 'An accurate estimation of bone density improves the accuracy of subject-specific finite element models', *J Biomech*, vol. 41, no. 11, pp. 2483–2491, Aug. 2008, doi: 10.1016/j.jbiomech.2008.05.017.

[219] B. Reggiani, L. Cristofolini, E. Varini, and M. Viceconti, 'Predicting the subject-specific primary stability of cementless implants during pre-operative planning: preliminary validation of subject-specific finite-element models', *J Biomech*, vol. 40, no. 11, pp. 2552–2558, 2007, doi: 10.1016/j.jbiomech.2006.10.042.

[220] J. J. Cherian, J. J. Jauregui, S. Banerjee, T. Pierce, and M. A. Mont, 'What Host Factors Affect Aseptic Loosening After THA and TKA?', *Clinical Orthopaedics & Related Research*, vol. 473, no. 8, pp. 2700–2709, Aug. 2015, doi: 10.1007/s11999-015-4220-2.

[221] M. Viceconti, R. Lattanzi, C. Zannoni, and A. Cappello, 'Effect of display modality on spatial accuracy of orthopaedic surgery pre-operative planning applications', *Med Inform Internet Med*, vol. 27, no. 1, pp. 21–32, Mar. 2002, doi: 10.1080/14639230110110233.

[222] J. Zhang, D. Malcolm, J. Hislop-Jambrich, C. D. L. Thomas, and P. M. F. Nielsen, 'An anatomical region-based statistical shape model of the human femur', *Computer Methods in Biomechanics and Biomedical Engineering: Imaging & Visualization*, vol. 2, no. 3, pp. 176–185, Jul. 2014, doi: 10.1080/21681163.2013.878668.

[223] M. Viceconti, G. Brusi, A. Pancanti, and L. Cristofolini, 'Primary stability of an anatomical cementless hip stem: A statistical analysis', *Journal of Biomechanics*, vol. 39, no. 7, pp. 1169–1179, Jan. 2006, doi: 10.1016/j.jbiomech.2005.03.024.

[224] A. B. Owen, 'A Central Limit Theorem for Latin Hypercube Sampling', *Journal of the Royal Statistical Society: Series B (Methodological)*, vol. 54, no. 2, pp. 541–551, 1992, doi: 10.1111/j.2517-6161.1992.tb01895.x.

[225] M. Daher, BSc, E. Mekhael, BSc, M. M. El-Othmani, and MD, 'Total Hip Arthroplasty in Patients with Hip Osteoporosis: A Narrative Review', *Hip & Pelvis*, vol. 36, no. 4, pp. 260–272, Dec. 2024, doi: 10.5371/hp.2024.36.4.260.

[226] E. Pansard, M. Vigan, and T. Bauer, 'Do the sizes of total hip arthroplasty implants match between 3D planning software and 2D templating?', *Orthopaedics & Traumatology: Surgery & Research*, vol. 110, no. 2, p. 103744, Apr. 2024, doi: 10.1016/j.otsr.2023.103744.

Acknowledgements

Finally, I have reached the moment to reflect on this journey and express my deepest gratitude.

First and foremost, I would like to extend my heartfelt thanks to my supervisor, Professor Marco Viceconti. I am profoundly honored to have been one of the doctoral students under his direct guidance. Beyond his scientific rigor and high-level insights that have shaped my research, I am most grateful for our countless discussions on technical details. His mentorship has been both an inspiration and a privilege.

My gratitude also goes to my colleagues at the Istituto Ortopedico Rizzoli. Their support and the collaborative environment they provided were essential to the completion of this work. I am also deeply indebted to my family and friends, whose unwavering encouragement and belief in me kept me going.

The past three years have been a journey of overcoming setbacks. While this thesis may not be a “perfect” piece of work, it represents my most perfect period of personal and professional growth. Living in Bologna, I have gained more than just knowledge; I have embraced its history, sensed its art, and, most importantly, learned the value of solitude and independent.

Lastly, I want to thank myself. For every time I faced a challenge and chose not to give up. The road ahead is long, but I look forward to meeting it with the same resilience and positivity.